The Dissertation Committee for Ahmad Sakhaee-Pour certifies that this is the approved version of the following dissertation:

Gas Flow Through Shale

Committee:

Steven L. Bryant, Supervisor

Larry W. Lake

Robert M. Reed

Sanjay Srinivasan

Mary F. Wheeler

Gas Flow Through Shale

by

Ahmad Sakhaee-Pour, B.S.; M.S.

Dissertation

Presented to the Faculty of the Graduate School of

The University of Texas at Austin

in Partial Fulfillment

of the Requirements

for the Degree of

Doctor of Philosophy

The University of Texas at Austin

August 2012

Dedication

To my family

Acknowledgements

I would like to express my highest appreciation to Professor Steven Bryant for his support during my Ph.D. study. Our regular weekly meetings shaped my understanding of pore structure. More importantly, his in-depth analyses and thoughtful comments were a significant stimulus in causing me to think more critically and sometimes very differently. His encouragement and assessment of my performance have played a vital role in my training, and without these, this study would not have been possible.

I acknowledge financial contribution from Exxon Mobil. This research has been mainly funded by Exxon Mobil and the Jackson School of Geosciences at The University of Texas at Austin through the Collaborative on Unconventional Reservoirs. I benefitted from quarterly meetings we had during the course of the project in which I had interactions with the industry people and geologists, and thus I would like to thank them.

I would like to extend my sincere appreciation to Dr. Edward Wanat of Exxon Mobil. His comments in the quarterly meetings and follow-up communications significantly enhanced the practicality of this research. He offered a different perspective from ours, and therefore I learned a great deal from him. I would like to thank him for his support and encouragement as well.

Further, I would like to acknowledge Dr. Barbara Faulkner of Exxon Mobil. She was the coordinator of the project from the industry side, and it was due to her efforts that we were able to have access to the actual data in a timely manner.

Moreover, I would like to thank Dr. Eric Potter from the Bureau of Economic Geology, who was the coordinator of the Collaborative at The University of Texas at

Austin. Without his coordination, we would not have been able to meet with Exxon Mobil regularly. I am also very grateful for his support during the course of this project.

Furthermore, I am extremely grateful for the instructive meetings I have had with Professors Larry Lake and Mary Wheeler during my PhD study. These meetings have played an important role in my education. I would also like to thank Professor Kamy Sepehrnoori, the graduate advisor of the Petroleum Engineering Department, for his valuable advice.

In addition, I would like to express my gratitude to the members of my dissertation committee—Professor Larry Lake, Dr. Robert Reed, Professor Sanjay Srinivasan, and Professor Mary Wheeler—for their comments during my proposal and final defense.

I am also thankful to the Petroleum and Geosystems Engineering Department staff. I would like to specifically thank Cheryl Kruzie, Roger Terzian, Sophia Ortiz, Rand Martin, Frankie Hart, Mary Pettengill, Allison Brooks, and Heather Routt.

Last but not least, I would like to express my appreciation to Stephaine Lane of the Bureau of Economic Geology, who played an important role in organizing one of our meetings with Exxon Mobil during the summer.

Gas Flow Through Shale

Publication No._____

Ahmad Sakhaee-Pour, Ph.D.

The University of Texas at Austin, 2012

Supervisor: Steven L. Bryant

The growing demand for energy provides an incentive to pursue unconventional resources. Among these resources, tight gas and shale gas reservoirs have gained significant momentum because recent advances in technology allowed us to produce them at an economical rate. More importantly, they seem likely to contain a significant volume of hydrocarbon.

There are, however, many questions concerning hydrocarbon production from these unconventional resources. For instance, in tight gas sandstone, we observe a significant variability in the producibilities of wells in the same field. The heterogeneity is even present in a single well with changes in depth. It is not clear what controls this heterogeneity.

In shale gas, the pore connectivity inside the void space is not well explored and hence, a representative pore model is not available. Further, the effects of an adsorbed layer of gas and gas slippage on shale permeability are poorly understood. These effects play a crucial role in assigning a realistic permeability for shale in-situ from a laboratory measurement. In the laboratory, in contrast to in-situ, the core sample lacks the adsorbed layer because the permeability measurements are typically conducted at small pore

pressures. Moreover, the gas slippages in laboratory and in-situ conditions are not identical. The present study seeks to investigate these discrepancies.

Drainage and imbibition are sensitive to pore connectivity and unconventional gas transport is strongly affected by the connectivity. Hence, there is a strong interest in modeling mercury intrusion capillary pressure (MICP) test because it provides valuable information regarding the pore connectivity. In tight gas sandstone, the main objective of this research is to find a relationship between the estimated ultimate recovery (EUR) and the petrophysical properties measured by drainage/imbibition tests (mercury intrusion, withdrawal, and porous plate) and by resistivity analyses. As a measure of gas likely to be trapped in the matrix during production—and hence a proxy for EUR—we use the ratio of residual mercury saturation after mercury withdrawal (S_{gr}) to initial mercury saturation (S_{gi}), which is the saturation at the start of withdrawal. Crucially, a multiscale pore-level model is required to explain mercury intrusion capillary pressure measurements in these rocks.

The multiscale model comprises a conventional network model and a tree-like pore structure (an acyclic network) that mimic the intergranular (macroporosity) and intragranular (microporosity) void spaces, respectively. Applying the multiscale model to porous plate data, we classify the pore spaces of rocks into macro-dominant, intermediate, and micro-dominant. These classes have progressively less drainage/imbibition hysteresis, which leads to the prediction that significantly more hydrocarbon is recoverable from microporosity than macroporosity. Available field data (production logs) corroborate the higher producibility of the microporosity. The recovery of hydrocarbon from micro-dominant pore structure is superior despite its inferior initial production (IP). Thus, a reservoir or a region in which the fraction of microporosity varies spatially may show only a weak correlation between IP and EUR.

In shale gas, we analyze the pore structure of the matrix using mercury intrusion data to provide a more realistic model of pore connectivity. In the present study, we propose two pore models: dead-end pores and Nooks and Crannies. In the first model, the void space consists of many dead-end pores with circular pore throats. The second model

supposes that the void space contains pore throats with large aspect ratios that are connected through the rock. We analyze both the scanning electron microscope (SEM) images of the shale and the effect of confining stress on the pore size distribution obtained from the mercury intrusion test to decide which pore model is representative of the in-situ condition. We conclude that the dead-end pores model is more representative.

In addition, we study the effects of adsorbed layers of CH_4 and of gas slippage in pore walls on the flow behavior in individual conduits of simple geometry and in networks of such conduits. The network is based on the SEM image and drainage experiment in shale. To represent the effect of adsorbed gas, the effective size of each throat in the network depends on the pressure. The hydraulic conductance of each throat is determined based on the Knudsen number (*Kn*) criterion. The results indicate that laboratory measurements made with N_2 at ambient temperature and 5-MPa pressure, which is typical for the transient pulse decay method, overestimate the gas permeability in the early life of production by a factor of 4. This ratio increases if the measurement is run at ambient conditions because the low pressure enhances the slippage and reduces the thickness of the adsorbed layer. Moreover, the permeability increases nonlinearly as the in-situ pressure decreases during production. This effect contributes to mitigating the decline in production rates of shale gas wells. Laboratory data available in the literature for methane permeability at pressures below 7 MPa agree with model predictions of the effect of pressure.

Table of Contents

List of Tables

List of Figures

Chapter 1: Introduction

1.1. Problem statement

Tight gas and shale gas reservoirs are thought to contain a significant fraction of energy (Polczer, 2009), yet the physics of flow through the matrices of these unconventional resources are not well understood. This is mainly because of the complexity of the pore connectivity in tight gas sandstone. In shale gas, this becomes even more challenging because the transport properties of a single nanoscale throat—the typical pore throat size in shale (Nelson, 2009)—are still a matter of active research.

In many conventional rocks, a significant range of saturation corresponds to a narrow range of capillary pressure during drainage. For instance, the wetting phase saturation (S_w), defined by $S_w = 1 - S_{Hg}$, decreases 0.7 (from $S_w = 0.9$ to $S_w = 0.2$) when the capillary pressure increases from 0.7 to 2.1 MPa in a carbonate sample, as shown in Figure 1.1 (Al-Sayari, 2009). This is shown by the gray box on Figure 1.1. The capillary pressure is within 50 percent of a threshold pressure in percolation (Berkowitz and Balberg, 1993). The threshold pressure is 1.4 MPa in this sample.

When percolation occurs, a large number of throats with capillary entry pressures smaller than the threshold pressure are accessed. These throats are not invaded at a lower pressure because access to them is only by way of narrower throats. The existence of a plateau-like trend in drainage curve, when capillary pressure versus wetting phase saturation is plotted in a linear scale, is an indicator of this phenomenon (see Figure 1.1). The conventional models, such as sphere packing (Behseresht and Bryant, 2009), are capable of capturing this plateau-like trend in the drainage curve when the results are plotted on a linear scale.

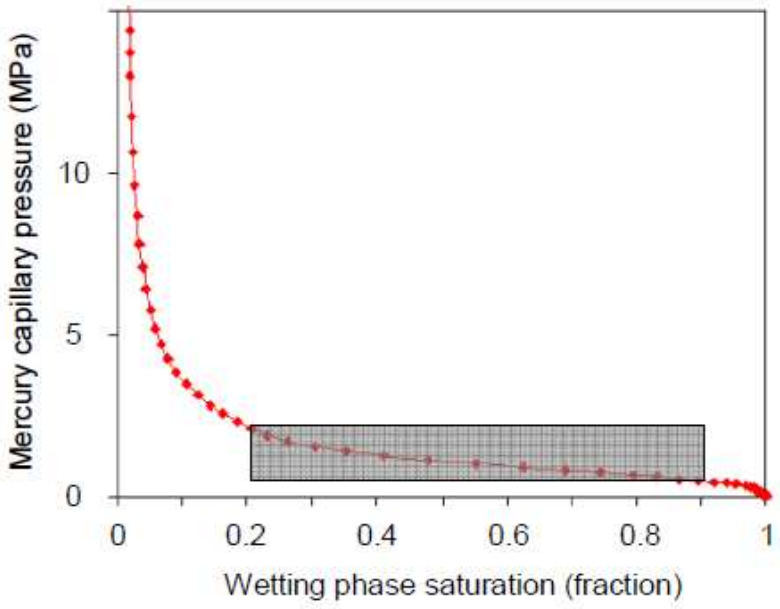

Figure 1.1: Drainage results of carbonate sandstone (Al-Sayari, 2009) obtained from mercury intrusion test. The gray box shows the decrease in the wetting phase saturation (S_w) from $S_w = 0.9$ to $S_w = 0.2$ when the capillary pressure increases from 0.7 to 2.1 MPa. This range of capillary spans 0.7 MPa from 1.4 MPa which is the threshold pressure of this sample. The wetting phase saturation here is defined by $S_w = 1 - S_{Hg}$. We observe a plateau-like trend of capillary pressure with wetting phase saturation in drainage when it is plotted on a linear scale.

In tight gas sandstones, however, the change in wetting saturation during mercury intrusion is rarely as large as the conventional sample we observe in Figure 1.2. That is, we do not see the plateau-like trend in drainage experiments, even when capillary pressure is plotted on a logarithmic scale. Thus, the conventional models, such as sphere packing (Mousavi, 2010), cannot capture the two-phase displacement of tight gas sandstones.

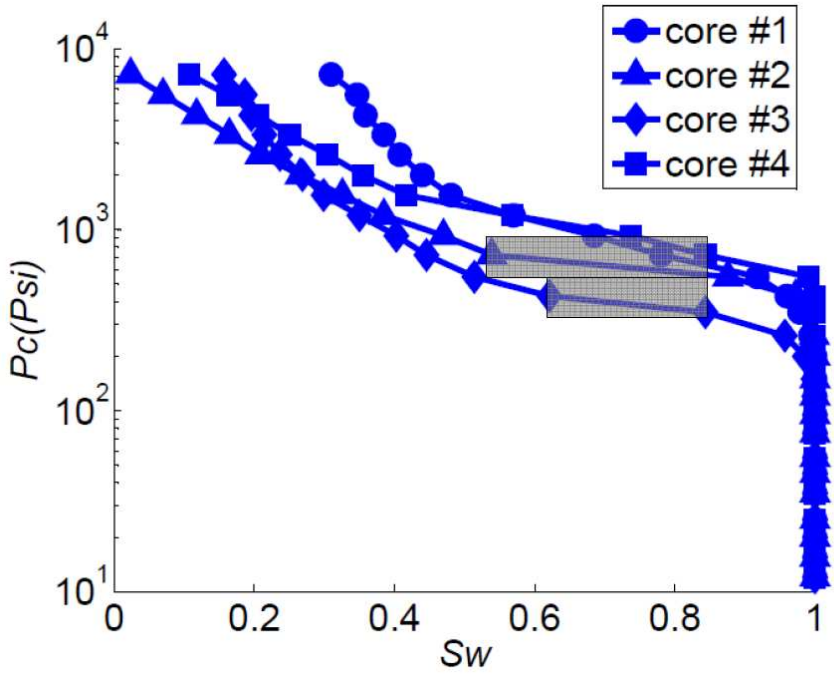

Figure 1.2: Mercury intrusion capillary pressures of confined Western tight gas sandstones versus wetting phase saturation (S_w), where $S_w = 1 - S_{Hg}$. The capillary pressure shows that there is no plateau-like trend similar to what we observe in Figure 1.1. There is only a slight percolation which is shown by the gray boxes. Thus, the conventional models such as sphere packing cannot capture this trend (Mousavi, 2010).

In shale reservoirs, there are two fundamental challenges in the physics of gas flow through the matrix. First, the extremely narrow size of the pore throats prevents us from using continuum models. Second, gas desorption takes places during the production, which alters the pore structure.

The pore throat size of shale is on the order of a nanometer (see Nelson, 2009), whereas those of conventional reservoirs are rarely less than microns. Figure 1.3 shows a scanning electron microscope (SEM) image of a shale sample (Wang and Reed, 2009). This means that the conventional models, such as sphere packing, used for studying transport in conventional rocks, in which pore throats are a hundred to a thousand times

larger, cannot be employed directly. This is because, in extremely narrow throats, molecule-wall collisions are more dominant than molecule-molecule collisions. Thus, the interactions of molecule-wall must be modeled to predict the flow properties, which is the case for shale. However, the conventional models are designed to capture molecule-molecule collisions, and thus cannot be adopted directly.

Further, most of the void space is inside the organic-rich region of Barnett shale (Loucks et al., 2008; Wang and Reed, 2009), as depicted in Figure 1.3, and that is where gas desorption takes place. The adsorbed layer of gas becomes thinner during production, and hence the pore throat area open to flow expands. This leads us to a new family of pore structures in which the resistance against the flow is a strong function of pressure. Such a pore model has not been developed.

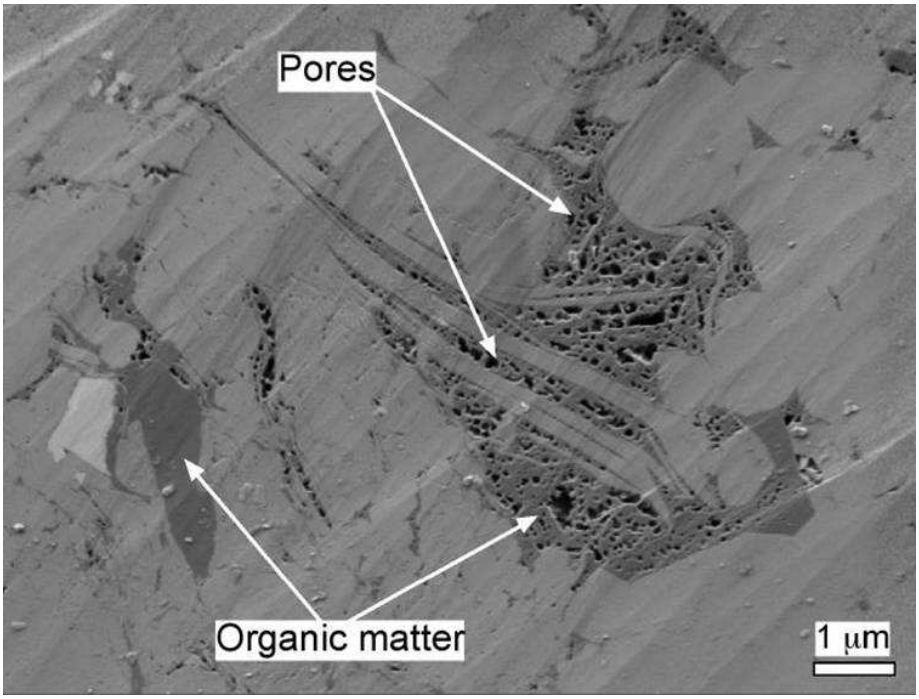

Figure 1.3: A scanning electron microscope image of a Barnett shale sample (courtesy of Wang and Reed, 2009).

1.2. Objectives

This dissertation examines the petrophysical properties of tight gas and shale gas reservoirs to understand how hydrocarbon flow takes place through the matrices of these unconventional resources. To this end, this study adopts the pore-scale modeling approach and discusses the implications of such modeling for production. For dealing with tight gas and with shale gas, respectively, the main objectives of the present study are the following:

a) To develop a new pore structure model to capture two-phase displacements in tight gas sandstone. This entails appropriate representations of the microporosity and macroporosity to mimic the flow through each and their interactions.

b) To analyze the pore connectivity of gas shale and compare it with the void space of conventional reservoirs. Further, we evaluate the effects of an adsorbed layer of gas and of gas slippage on the single-phase gas permeability.

1.3. Hypotheses tested in this research

The conventional network models, such as sphere packing and regular lattice, allowed many researchers to analyze flow properties through a matrix of unconsolidated sandstone (Behseresht et al., 2009; and Rodriguez, 2010). The network modeling approach divides the void space into pores interacting with each other by the pore throats. We adopt the term “conventional” here for the regular lattice and sphere packing-based models because the positions of the pores are assigned either from the pattern of regular lattice or from sphere packing. The pore throat size is then obtained from the positions of the grains in the sphere packing-based approach, and in the regular lattice, the pore throat size is assigned randomly from mercury intrusion capillary pressure mesuremeant data. In the present study, we hypothesize that the network modeling approach can capture the

transport properties of tight gas sandstones and of gas shale if the positions of the pores are assigned appropriately and if their characteristics sizes are determined correctly.

In tight gas sandstone, our hypothesis is that the natures of the intergranular and intragranular voids are different both in terms of the characteristic size of the pore throats and the spatial distribution (topology) of the pore throats. We term “intergranular” and “intragranular” voids as “macroporosity” and “microporosity”, respectively, and use them interchangeably. This means that this is a topological criterion and not a size criterion. Thus, we propose a multiscale network model to capture the transport properties of this unconventional resource. The multiscale model comprises a conventional network model and a tree-like pore structure (an acyclic network) that mimic the intergranular (macroporosity) and intragranular (microporosity) void spaces, respectively.

The present study tests the proposed multiscale model by comparing the predicted results of the model with the petrophysical measurements. We compare the imbibition data obtained from mercury withdrawal as well as drainage results from the porous plate experiment. We also test the actual production data because our model has major implications for producibility. The model classifies the producing intervals into macro-dominant, intermediate, and micro-dominant, and predicts that the hydrocarbon recovery improves progressively in these intervals. This classification is based on the fraction of connected microporosity to total porosity, meaning that the micro-dominant interval has the largest fraction of connected microporosity. To test the hydrocarbon recovery prediction, we use field data (production logs) taken at different times in a single well.

In shale gas, our hypothesis is that the void space of the un-fractured matrix consists largely of dead-end pores. Hence, we propose a tree-like pore model in which many pores with circular pore throats are connected to a branching point. This is similar

to the tree-like pore model proposed for the microporosity of the tight gas sandstone. This part of our research aims to provide a more representative model for pore connectivity.

We test the pore connectivity model by SEM images of shales to determine whether the pore connectivity model, in which each pore is connected to three or fewer pores, is consistent with the image analyses available in the literature. We also analyze the effects of confining stress on the drainage results obtained from mercury intrusion test and on the pore throat geometry. The image analysis reveals whether the circular pore throats we adopt for the dead-end pores model remain open under confined conditions, which is representative of in-situ stress boundary conditions.

In addition, we study the effects of adsorbed layer of methane and gas slippage on the pore walls. We hypothesize that an adapted network model can be used to analyze the single-phase gas flow properties at in-situ conditions. Both the adsorbed layer and slippage are present at in-situ conditions. This model is based on SEM images of shale samples and a pore size distribution obtained from the mercury intrusion test. It further accounts for the effects of an adsorbed layer and slippage depending on the gas pressure. The thickness of the adsorbed layer increases with the gas pressure whereas the slippage decreases with an increase in the gas pressure.

The present study also tests the adapted network model predictions against laboratory measurements available for low pressures (< 8 MPa). At those pressures, gas slippage plays a more important role, and thus the laboratory results yield a partial validation of the model.

Chapter 2: Literature review

The present study consists of two major sections, the first deals with tight gas reservoirs and the second with shale gas reservoirs. The following literature review covers studies related to each of these topics.

2.1. Tight gas sandstone

In tight gas sandstone, the objective of this study is to understand the pore structure in terms of the characteristic size of the throat and connectivity. In-depth understanding of the pore structure is crucial because it allows us to predict the ultimate recovery. The prediction of hydrocarbon recovery from the understanding of the pore structure arises here and not in the conventional rocks because there are two types of porosities, i.e. microporosity and macroporosity, interacting with each other unlike the conventional rocks. Possible differences in the pore structures of the porosities makes it possible for them to behave differently in terms of recovery and thus, it is possible for producing intervals of a well, which could have different fractions of these porosities, to produce differently. Therefore, we will mainly focus on the petrophysical models of the pore structure both analytical and empirical.

We begin with a definition of tight gas sandstone. Tight gas sandstone is generally considered a formation with low permeability. The US government provided a more precise definition by indicating that its single-phase permeability is less than 0.1 microD (Holditch, 2006). Some researchers, however, disagreed and proposed alternative definitions. For instance, Holditch (2006) stated that a formation is tight gas if it is producible at an economic rate only after hydraulic fracturing. Later, Nelson (2009) recommended another criterion. He claimed that hydrocarbon is not stored under the buoyancy force in these formations and that this should be adopted as a distinguishing

criterion. Despite the differences in the definitions, they have the commonality of not using porosity as a screening factor. This tells us that the resistance of the formation against the flow is the main concern and is probably is the reason why many researchers studied the flow behavior of tight gas sandstones.

Many studies have been undertaken to model the fluid flow through these reservoirs. The importance of these studies becomes more obvious considering the fact that these reservoirs behave differently from the conventional reservoirs in several respects (Masters, 1979; Masters, 1984; Law and Dickenson, 1985; Spencer, 1985, 1989; Surdam, 1997). One characteristic of these unconventional reservoirs is that producibility can vary widely from well to well. Another characteristic is that water production rates strongly affect the economics of gas production but are difficult to predict. The amount of fluid recovered after the hydraulic fracturing operation is also an important consideration (Bazin et al., 2010; and Bahrami et al., 2011).

The influence of confining stress on the porosity and single-phase permeability were also studied (Ostensen, 1983; Luffel et al., 1991; Byrnes and Castle, 2000; Jones and Owens, 1980). It was reported that the porosity change with loading is negligible whereas the permeability decreases notably (Jones and Owens, 1980). It was further stated that the permeability reduction is more notable for lower permeability rocks (Jones and Owens, 1980). Considering the significant decrease of permeability with loading, it was concluded that the flow occurs mainly through sheet-like cracks and consequently, the crack closure was modeled (Cluff and Webb, 2009). Further, two-phase flow characteristics were explored (Shanley et al., 2004). Analyzing the relative permeability data available in the literature, Shanley et al. (2004) argued that over a wide range of wetting phase saturation, gas does not flow. In addition, the influence of diagenesis on flow properties was investigated (Mousavi and Bryant, 2008, Lee et al., 2010, and Olson

et al., 2010). In other research, it was indicated that the pore connectivity is a dominant parameter in the fluid flow (Mousavi and Bryant, 2009).

The macroscopic flow properties of sedimentary rocks depend on their microscopic structure (*i.e.*, grain scale geometry) and on conductive fractures within the rock. To better understand this dependence, many researchers have investigated pore structures of conventional sandstones, and recently those techniques have been extended to tight gas sandstones (Nelson, 2009). Hayes (1991) showed that the porosity evolution stages can be indicated from the vitrinite reflectance, (R_o). The stages are destruction of primary porosity, dissolution porosity, and destruction of porosity by cementation and compaction.

Many conventional models, such as Corey-Brook (1966), cannot capture the two-phase flow properties of tight gas sandstone. This is because the conventional models were proposed for the pore structures of conventional rocks, which differ from the pore structure of tight gas sandstone. Therefore, to create an appropriate model, we need to understand the pore structure of tight gas sandstone and its differences from conventional rocks. This entails analyzing the fluid flow from a fundamental level, that is, at the pore-scale. The pore-scale approach accounts for the interactions of the pores, which are connected in a network pattern.

2.2. Theoretical approaches (network modeling)

Network modeling is a theoretical approach that mimics the void space by building a network of pores connected to each other. The interaction of the connected pores is through the pore throat. This approach implements the interactions of pores inside the rock and allows us to estimate flow properties such as permeability.

2.2.1. Bundle-of-tubes model

Purcell (1949) proposed the bundle-of-tubes model for a void space in a porous medium. This means that the parallel tubes can model the macroscopic transport properties. The main goal of this approach was to relate the mercury intrusion experiment (drainage) to single-phase permeability. A schematic illustration of the model representing a three-dimensional representation of a rock is shown in Figure 2.1.

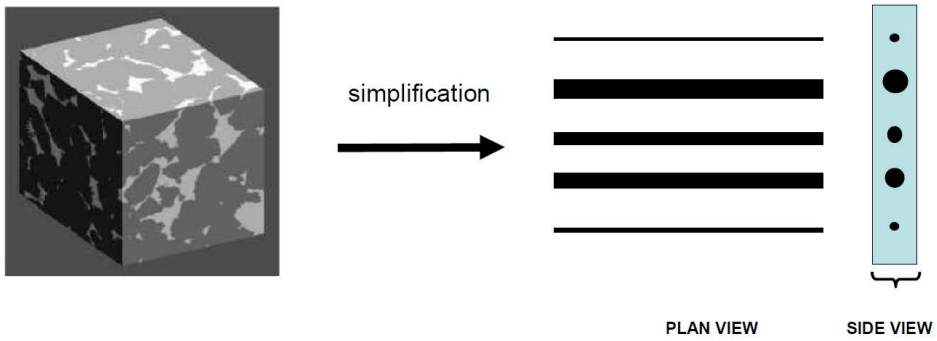

(a) (b)

Figure 2.1: The bundle-of-tubes model depicted in (b) simplifies the three-dimensional pore model of a rock shown in (a). The simplified representation of the void space contains many parallel tubes with a circular cross section. See the plan and side views in (b).

The main notion here is that the void space accessed at each capillary pressure has a characteristic size that controls the permeability. The characteristic size is relevant to the size of the tube because this model presumes the void space contains parallel tubes. The characteristic size of the tube is determined from mercury intrusion capillary pressure (MICP) data using the Young-Laplace equation. With this notion, Purcell (1949) related the drainage measurement to single-phase permeability:

$$k = F\frac{\gamma^2\phi}{2}\int_{S=0}^{S=1}\frac{dS}{P_{c_i}^2} \tag{2.1}$$

where γ is the interfacial tension of the mercury, φ is the porosity of the sample, S_w is the wetting phase saturation, and F is the lithology factor. The lithology factor is a matching parameter which is calculated for each type of pore structure after fitting the above relation to a number of samples.

The main advantage of the bundle-of-tubes model is its simplicity. In addition, it incorporates the idea of pore size distribution into the pore model. However, it fails to provide a realistic image of the rock, as it ignores the pore connectivity. In reality, pores are not arranged in a pattern similar to tubes.

2.2.2. Interconnected tubes model

Because pores are interconnected, the bundle-of-tubes model is not representative of the void space. With that in mind, Fatt (1956) proposed that the pores are interconnected in a regular lattice pattern. Figure 2.2 shows a two-dimensional regular square lattice model as an example.

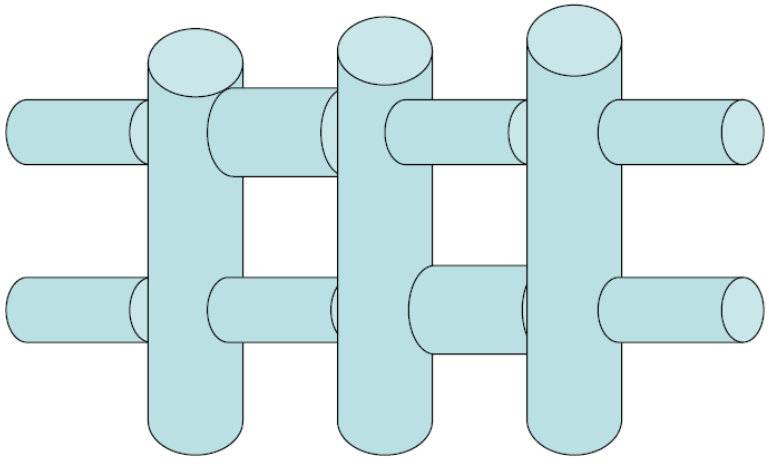

Figure 2.2: A two-dimensional regular square lattice model was proposed by Fatt (1956). This model includes interconnectivity of the pores and is capable of capturing residual nonwetting phase saturation during drainage and imbibition.

This model accounts for the interconnectivity of the pores. The interconnectivity permits us to capture the residual wetting phase saturations both in drainage and imbibition. We are aware that the wetting phase remains in the void space in the form of residual phase and hence, this model is more representative of the pore space of the conventional rocks such as unconsolidated sandstone.

2.2.3. Network extraction from rock image

The rock image indicates positions of the pores and thus, we can extract the network model directly (Oren et al., 2002). Because this is a direct extraction of the network model from the void space without considering a pattern a priori similar to the Bundle-of-tubes and regular lattice model, we consider this a semi-analytical approach. The resolution of the images must be comparable to the characteristic size of pore throats to let us derive detailed information of the void space. Because of the resolution issue, this approach faces challenges for tight gas and shale gas. The void spaces of these unconventional reservoirs contain extremely narrow throats, which could be on the order of nanometers for shale (Sakhaee-Pour and Bryant, 2012).

2.2.4. Sphere packing as a pore space model

We could consider a packing of spheres as an approximate model of the unconsolidated sandstone in which the spheres represent the grains and the empty space between them the void space. With that notion, Bryant et al. (1993) developed a physically representative network model using the actual measured data of 8000 bearing balls (Finney, 1970). Using the representative model, researchers also examined the effects of grain sedimentation, compaction, and diagenesis on the transport properties (Bryant et al., 1993; Oren et al., 1998).

A random sphere packing was also created with computer generated codes (Thane, 2006) by implementing a cooperative rearrangement method (Cargill, 1984). This is similar to actual sphere packing (Finney, 1970) because the spheres represent the grains. Unlike the actual packing, however, the computer code can impose periodic

boundary conditions at the packing edges. This eliminates edge effects, which further improves the representation of the void space. The elimination of the edge effects allows us to use a finite size model and yet analyze the flow behavior in an infinitely extended porous medium (Behseresht et al., 2009). An example of a random sphere packing is shown in Figure 2.3 (courtesy of Rodriguez, 2010).

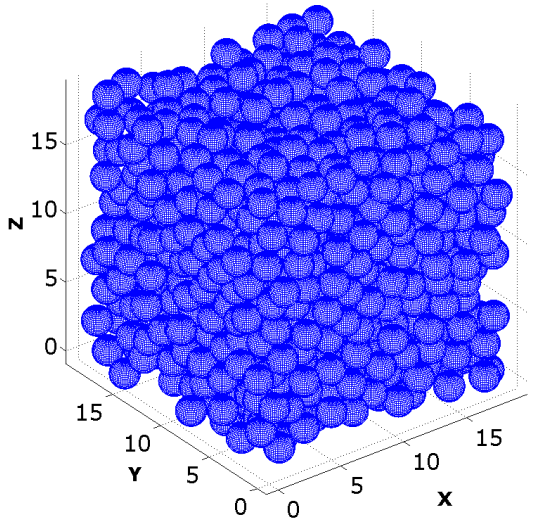

Figure 2.3: An example of a random sphere packing that is used as an approximate model for the void space of unconsolidated sandstone. The generated packing contains 1000 spheres of a radius of 1 in which a periodic boundary condition is imposed (courtesy of Rodriguez, 2010).

2.2.5. Pore throat resistance against flow

The detailed information of the positions of the grains, either from the actual packing (Finney, 1970) or the computer code (Thane, 2006), allows thorough extraction of the geometry of the empty space. The empty space is to represent the void space and hence, we can use it to build a network of pores connected to each other. We can then obtain the resistance of each pore throat against the flow from the extracted empty space.

The resistance of pore throat in a three-dimensional space is determined by the Delaunay Tessellation technique (Gladkikh and Bryant, 2006). The Tessellation is a computational geometric structure that splits the space into convex polygonal regions. The splitting is implemented by grouping every four nearest spheres together. An

example of a grouped four spheres is shown in Figure 2.4 in which pore throats are at the surfaces of tetrahedron. The resistance of each pore throat is calculated based on the opening area available at the surface.

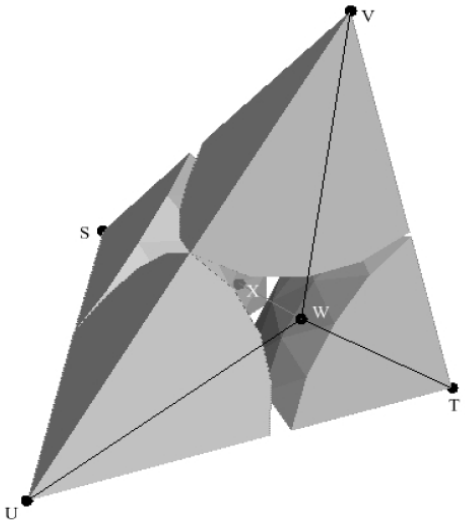

Figure 2.4: Delaunay cell formed by four neighboring spheres. The point W indicates the center of the gap. The point X indicates the center of the pore body. The plane defined by points UVT identifies one of the four pore throats (courtesy of Mousavi, 2010).

2.2.6. Extension of the sphere packing model for tight gas sandstone

The outstanding success of the sphere packing model in explaining the flow properties of unconsolidated sandstones (Bryant et al., 1993; Oren et al., 1998) provided an incentive to test them for tight gas sandstone. This is because they were found to be representative of the intergranular void space that constitutes the porosity of unconsolidated sandstone. Hence, Mousavi and Bryant (2007) used the sphere packing model to study the effects of compaction and cementation on the intergranular void space of tight gas sandstone. They implemented the compaction by considering soft and hard grains that penetrate each other. Then, they grew the sizes of the grains for the cementation.

This approach is successful when it is of interest to better understand the

intergranular void space. However, this is not always the case especially for tight gas sandstone in which a significant fraction of the porosity is intragranular. The intragranular void is inside the grain, whereas the intergranular void is between the grains. With that in mind, Mousavi (2010) tested whether the drainage results of the tight gas sandstone could be captured by the sphere packing model, and proved that the intergranular model alone is not capable of modeling two-phase displacement.

2.3. Empirical approaches

Empirical approaches aim to capture a correlation between petrophysical properties. For instance, many correlations were proposed to map the capillary pressure measurement to single-phase permeability (Swanson, 1981; Thomeer, 1983). As an example of such, we review the Swanson (1981) method and its extensions to tight gas sandstone.

2.3.1. Swanson method

Swanson (1981) proposed a correlation to estimate single-phase permeability from the mercury intrusion test (drainage). This is useful because it allows approximation of the permeability from small pieces of a rock such as portions of sidewalls or drilling cuttings.

To propose the correlation, Swanson (1981) defined effective bulk saturation (S_b) on the drainage curve obtained from the mercury intrusion experiment. The effective saturation corresponds to a capillary pressure (P_c) at which pores effectively interconnect the void space and thus, they control the flow behavior. The effective saturation is a saturation at which the slope of tangent to the P_c-S_w curve in a log-log plot is –1. Knowing the effective bulk saturation (S_b) and its corresponding capillary pressure (P_c), Swanson predicted the permeability as follows:

$$k_{Swanson\_brine} = 431\left(\frac{S_b}{P_c}\right)^{2.109} \tag{2.2}$$

where the coefficients 431 and 2.109 are empirical and calculated after fitting the above relationship to 24 clean sandstones.

As an example, we show the procedure for a 15-bar ceramic sample here. The 15-bar is an indicator of the characteristic sizes of the pore throats of the sample. It shows that the air starts to invade the saturated sample and push the moisture out when its relative pressure is 15-bar. This capillary pressure is often considered an entry pressure in petroleum engineering terminology.

To find the effective bulk saturation and its corresponding capillary pressure from the Swanson method, we plot the capillary pressure versus the mercury (nonwetting phase) saturation in a log-log plot (Figure 2.5). We then draw a tangent line to the curve where the slope is –1. The mercury saturation at the described point is 0.56 of the saturation unit, which means that the bulk saturation is 0.18 of the saturation unit, since the porosity of the sample is 0.32 ($S_b = \phi S_{Hg} = 0.32 \times 0.56 = 0.18$). Note that the effective bulk saturation is calculated with respect to the bulk volume and not the void space and that is why we implement the porosity here. The capillary pressure at this point is 2160 psi. Using these values, the Swanson method predicts that the single-phase permeability is 18 microD.

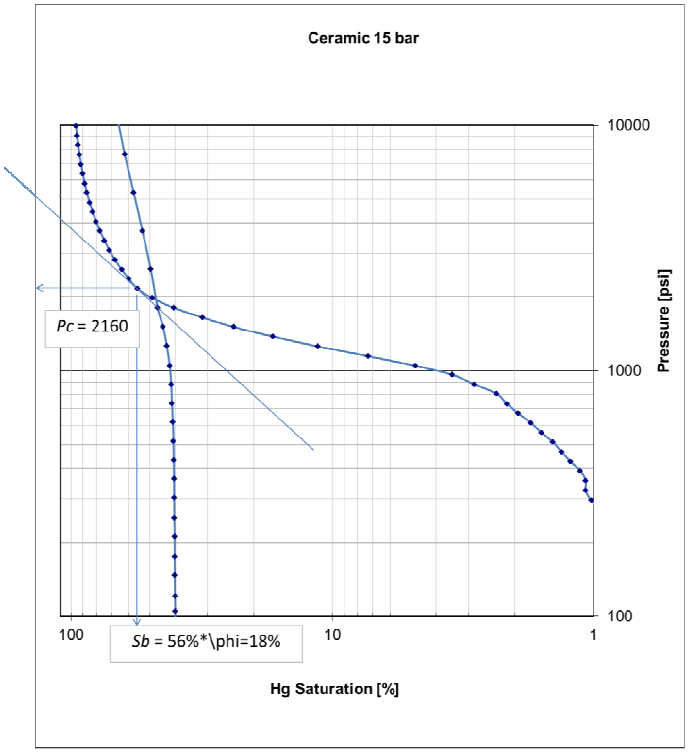

Figure 2.5: Illustration of the Swanson (1981) method for a 15-bar ceramic sample. The effective bulk saturation (S_b) and its capillary pressure correspond to the point where the slope of curve in the log-log demonstration is –1.

2.3.2. Extensions of the empirical model for tight gas sandstone

Comisky et al. (2007) published a thorough review of the empirical models extended capture correlations between the petrophysical properties of tight gas sandstones. For completeness, we mention two correlations that are based on Swanson (1981).

Walls and Amaefule (1985) proposed a new correlation for tight gas sandstones whose permeabilities are smaller than 0.01 microD. They mapped the mercury intrusion data (drainage) to the single-phase permeabilities. The laboratory measurements were run under net effective stresses between 3000–4000 psi. They re-evaluated the Swanson coefficients as follows:

$$k_{Walls-Amaefule} = 30.5\left(\frac{S_b}{P_c}\right)^{1.56} \tag{2.3}$$

Later, Kamath (1992) provided another correlation for tight gas sandstone when the permeability is smaller than 1 microD. The new correlation is expressed in below:

$$k_{Kamath} = 413(\frac{S_b}{P_c})^{1.85} \quad (2.4)$$

While these types of correlation provide a quick tool for permeability estimation, they do not provide insights into the pore structure. More importantly, the estimation is not reliable for a specific sample unless it is in the pool of data.

2.4. Shale gas reservoirs

Shale has provoked a great deal of research recently owing to the considerable volume of natural gas stored in these resources (Polczer, 2009). The natural gas produced from these reservoirs is called shale gas, and is envisaged to provide a substantial fraction of US gas production, perhaps as much as half by 2020, according to some reports (Polczer, 2009).

Shale and mudrock are sometimes used interchangeably; strictly speaking, however, they are different in appearance despite their similarities in composition. Mudrock lacks fissility (Blatt and Tracy, 1996), unlike shale. This means that mudrock does not separate along thin laminae or parallel layers that are less than 1 cm thick.

2.4.1. Scanning electron microscope (SEM) images

Understanding the void space of shale gas presents major challenges. For instance, the characteristic size of the pore throat is on the order of nanometers. This extremely narrow throat size prevents us from using continuum models to analyze the fluid flow behavior, an aspect discussed in greater detail in the final chapter of the present study. Moreover, the void space changes during production because of gas desorption taking place inside the organic-rich region.

With the major challenges of the shale in mind, we begin with the images of the shales because they help us to clarify the complexities of pore structure. Figure 2.6 shows scanning electron microscope (SEM) images of different shales. We observe that the pore size is on the order of nanometers. Further, there is a notable difference in the wettability of the pores and they are not all the same. In the Barnett shale, most pores are inside the organic-rich region, meaning that they are gas wet while in some other samples, such as Fayetteville, pores reside in the non-organic-rich region. The organic-rich region is shown with dark gray color in this image.

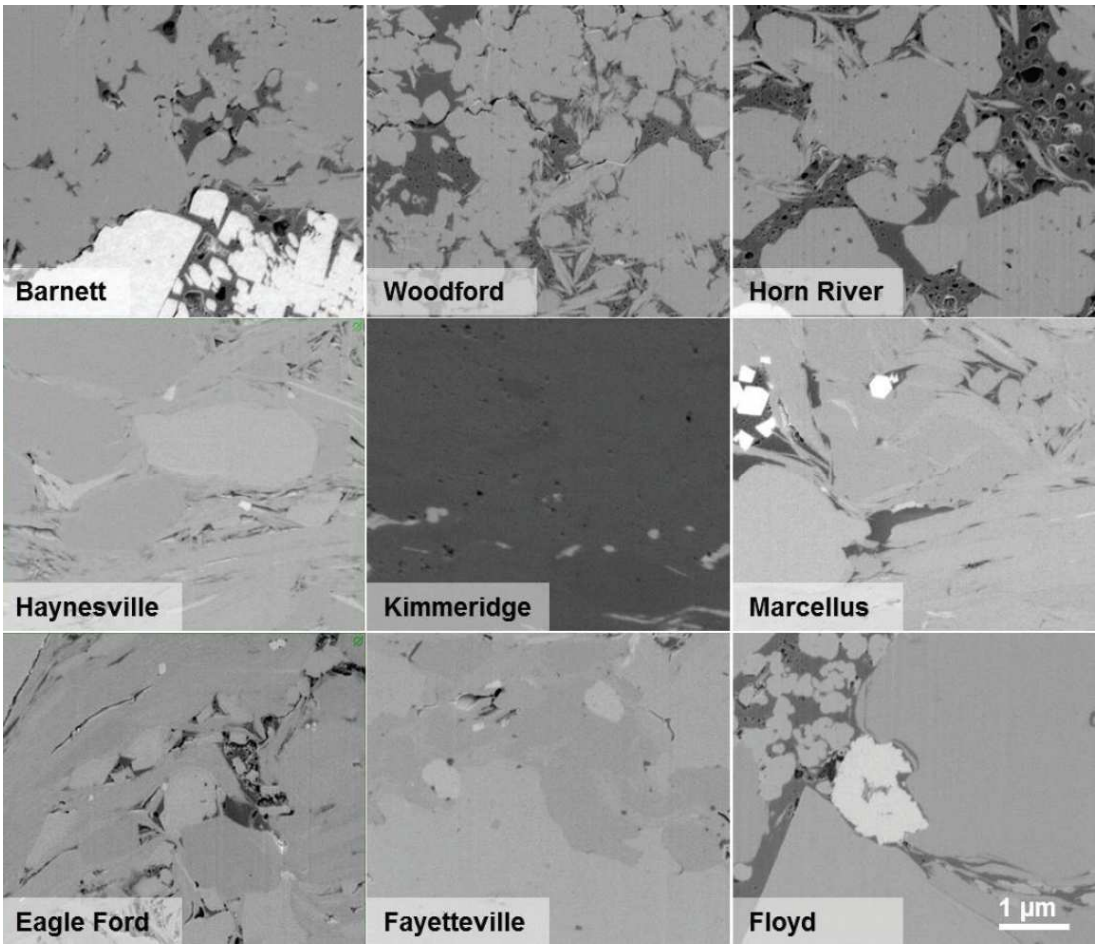

Figure 2.6: Scanning electron microscope images of shale samples (courtesy of Curtis et al., 2010). The pore size is on the order of nanometers. We also observe that

pores are inside the organic-rich region in some shales, such as Barnett. The organic-rich region is shown with gray color. The pores in the images are shown by black color.

We should be careful when we interpret these images as they are obtained without confining stress, and thus many crack-like pores may be closed under confined conditions, which is more representative of in-situ boundary conditions.

2.4.2. Pore connectivity of shale from laboratory measurements

We cannot deduce significant information regarding the pore connectivity of the shale from SEM images because they are limited to a very small region of the rock. Consequently, researchers made other laboratory measurements, such as the mercury intrusion capillary test (Heath et al., 2011) and adsorption/desorption (Adesida et al., 2011). These tests give us valuable insights not only into the pore connectivity but also the pore size distribution.

Figure 2.7 shows mercury intrusion results of Kirtland and Tuscaloosa shale samples (Heath et al., 2011). The “After closure” condition indicated on the plots is relevant to the confined boundary condition, which mimics the loading at in-situ condition. We observe that the capillary entry pressure is almost equal to 30–80MPa after closure. This tells us that a significant fraction of the pore throats have characteristic sizes smaller than 10 nm. We also observe that the capillary pressure increases almost linearly with mercury saturation (nonwetting phase). This trend of capillary pressure vs. mercury saturation sheds light on the pore connectivity of the shale, as we will discuss later in this study.

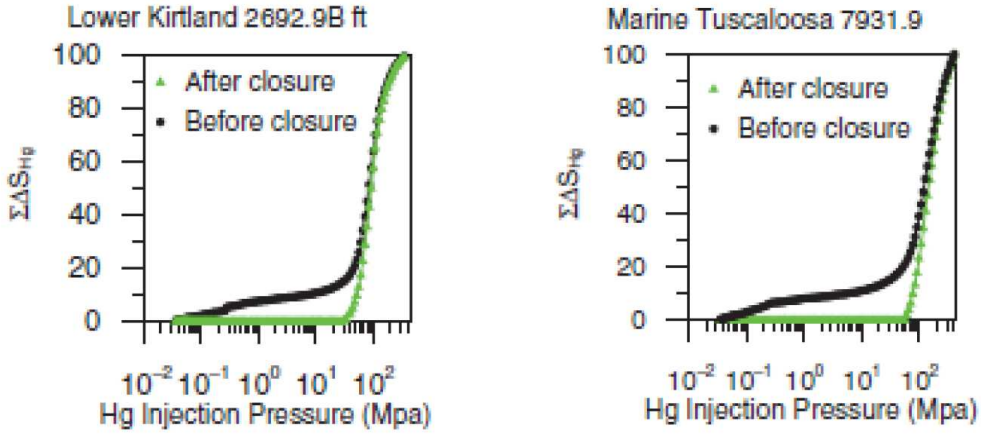

(a) (b)

Figure 2.7: Mercury intrusion capillary pressures of (a) Kirtland and (b) Tuscaloosa shales (courtesy of Heath et al., 2011). The "After closure" refers to confined boundary condition which is representative of in-situ boundary conditions.

Also, Adesida et al., (2011) derived the pore size distribution of shale sample using the adsorption/desorption experiment. Their measurements further confirm that most pores have characteristic sizes smaller than 10 nm.

2.4.3. Modification of petrophysical properties for shale

To provide a meaningful parameter that describes the petrophysical properties of shale, many researchers revisited the commonly adopted definitions. For instance, Sondergeld et al. (2010) re-evaluated the logs for shale to provide meaningful values for its petrophysical properties.

Some of the challenges we encounter in studying shale stem from gas desorption, which is absent in conventional reservoirs. Gas desorption is crucial in shale because it forms a significant fraction of stored hydrocarbon volume stored. To address this, Ambrose et al. (2010) investigated the effect of adsorbed gas on the porosity and provided a new model. Passey et al. (2010) also analyzed this issue and recommended

that we express the hydrocarbon storage in the form of bulk volume of gas. This definition does not require any porosity evaluation.

2.5. Permeability measurements

We measure the permeability of each formation to model hydrocarbon flow through the reservoir. Similarly, this was undertaken for shale gas reservoirs to understand the flow behavior. Therefore, we review the measurement techniques available in the literature and indicate whether they are used for shale.

2.5.1. Constant head

The constant head approach applies a constant pressure difference to a core sample to measure the permeability. This test uses the steady-state flow rate to determine the permeability. Although this method is widely adopted for high-permeability rocks, it is not used for the shale. This is because shale permeability is on the order of nanoD (10^{-9} Darcy) and thus, this method entails a great deal of time to reach a constant flow rate.

2.5.2. Transient pulse decay (TPD)

Brace et al. (1968) developed the transient pulse decay (TPD) method for low-permeability rocks. This measurement technique is widely used to measure the single-phase gas phase permeability of shale (Billiotte et al., 2008). In this approach, a core sample, which is usually in lab condition and filled with air and/or remaing gas from the reservoir, is connected to two reservoirs that are held at an equal constant pressure initially. Then, the upstream pressure is elevated by imposing a pulse pressure increase to the upstream reservoir. Consequently, the difference between the pressures of core ends decays over time. The rate of decay over time is used to estimate the permeability.

Brace et al. (1968) indicated that the difference between the pressures of upstream and downstream decays exponentially. Thus, the normalized decline in the pressure difference was expressed as follows:

$$\frac{\Delta P(t)}{\Delta P_o} = e^{-at} \tag{2.5}$$

where ΔP_o refers to the initial pressure difference after imposing the pulse increase in the pressure and $\Delta P(t)$ shows how this difference changes with time. a includes pertinent parameters of the experiment and allows us to estimate the gas permeability as follows:

$$a = \frac{k_g}{\mu\beta}\frac{A}{L}\left(\frac{1}{V_{up}} + \frac{1}{V_{down}}\right) \tag{2.6}$$

where k_g is the gas permeability, μ viscosity of the gas, β the compressibility factor, A cross section area of the sample, L length of the core, V_{up} the upstream reservoir volume, and V_{down} the downstream reservoir volume. Two times are measured to fit the exponential curve to the experimental (see Equation (2.5)). These times are when the ratio of the pressure differences ($=\Delta P(t)/\Delta P_o$) is equal to 0.95 and 0.50.

Jones et al. (1997) proposed a faster transient pulse decay method to accelerate the measurement. Unlike the TPD, the late-time response of the decay in the pressure difference is analyzed here. The hypothesis is that the late response is not significantly affected by the initial pressure distribution. Hence, the uniform initial pressure condition is not required here and thus, we can conduct the test faster.

2.5.3. Crushed rock method

Luffel et al. (1993) used TPD for the permeability measurement of crushed rocks to accelerate the process. They crushed the samples that were saturated with in-situ water saturation and placed them inside a small cell. Then, they connected the small cell to a

chamber containing a higher pressure gas. The pressure difference between the small cell and chamber decays with time. The rate of decay is used to predict the permeability.

Initially, gas invades the void space between the chips and this causes a sudden pressure drop. Later, the rate of pressure drop decreases as gas starts to invade the pore space of the rocks. The later pressure drop is used for the permeability estimation.

Many laboratories use this technique because the data measurement is not time consuming. However, the interpretation of the data is not straightforward and entails some assumptions. For instance, this method assumes that all the crushed rocks are cylindrical chips and also that they have the same size. Then, a simulator model is used to capture the pressure drop and from that model the permeability is extracted. This method cannot apply confining stress to the rock samples, which could play a crucial role. This is because the crushed rocks are in irregular shapes. These assumptions raise concerns about the reliability of the reported permeability.

2.5.4. Oscillating pulse technique

Suri et al. (1997) predicted the rock permeability by analyzing the pore pressure reaction of a sample to an oscillating pressure. The core sample was initially kept under a known uniform pore pressure. Then, the upstream pressure of the sample was changed with constant amplitude and frequency. The phase lag and amplitude ratio of the downstream pore pressure to upstream pore pressure were used to estimate the permeability.

Shale permeability has not been measured using this technique and thus, the performance of this technique is not clear.

2.5.5. CT-based method

Dvorkin et al. (2003) used a three-dimensional computerized tomography (CT) image of a shale sample to investigate flow properties. They extracted a network model of the sample from the CT image. Using the model, they studied the resistance of the sample against the flow.

This approach permits researchers to acquire detailed information of the void space. However, we should be aware that the images are acquired without confining stress. This means some pores for which the detailed information is obtained may not be present under confined boundary conditions. The confined boundary condition is more representative of the in-situ stress condition.

2.6. Theoretical modeling of the flow through shale

The void space contains many pore throats with different characteristic sizes and spatial locations. The overall interactions of these throats govern the resistance of the formation against the flow and thus, we need to have a thorough understanding of the physics of the flow through each throat to be able to predict the overall outcome of their interactions. Therefore, we first review the physics of the flow through a single narrow throat, whose characteristic size is similar to the characteristic size of the shale throat. Then, we review studies undertaken at larger scales.

The number of studies examining flow through the matrix of shale is limited. There have been more studies at large scales, as we will see subsequently.

2.6.1. Physics of flow through a single throat

The physics of gas flow through a nanoscale throat is of interest to us because the characteristic size of the pore throat inside the shale is on the order nanometers (Sakhaee-

Pour and Bryant, 2012). The flow studies at this scale were largely devoted to the straight tube because of the complexity of the problem. For example, Roy et al. (2003) performed a finite element analysis (FEA) to estimate the mass flow rate through nanoscale pores. Later, Zhou et al. (2006) modeled the gas flow rate for the Couette problem using the Lattice Boltzmann method.

The physics of the problem is even more challenging when interactions of the nanoscale tubes occur. This is the case if we want to represent the void space of the shale because the void space is a network of throats connected to each other. To avoid this challenge, some analyses were performed to model flow through shale by assuming that the porous medium acts similar to a single tube. In these analyses, the void space is simplified to a single-sized tube. For instance, Michel et al. (2011) investigated the effects of accounting for the non-ideality of flowing gas on transport properties. They modified the mean free-path of the gas to evaluate the slippage. In addition, Fathi et al. (2011) modeled the flow behavior by adopting a single tube. They studied the interactions of gas molecules with the pore walls of kerogen.

2.6.2. Physics of flow through a network of nanoscale throats

The void space is a network of pore throats connected to each other. Therefore, it is of interest to model the flow behavior by accounting for the interactions of the throats. It is instructive to know how the conventional pore models predict the flow behavior for shale samples. With that in mind, the Carman-Kozeny model was used to predict the liquid permeability for shale (Yang and Aplin, 2007; Mallon and Swarbrick, 2008). The Carman-Kozeny model assumes that the void space is made of conduits with circular cross-sections.

2.7. Statistics-based simulation of the reservoir

The physics of the flow through shale is very complicated and thus, it has become tempting for researchers to develop more statistics-based approaches. These approaches, indeed, require a large pool of actual production data. For instance, Xiao et al. (2011) proposed a combined physics-based and data-driven reservoir simulator. They corrected the results of the simulator that were based on the physics of the problem when there was a significant deviation from the actual data. This trend of favoring statistics over the physics of the problem was further extended. Strickland et al. (2011) attempted to predict the ultimate recovery solely by analyzing the production rate. This was implemented by the correction of the Arps' decline curve.

2.8. Implementation of the adsorbed layer

Most of the void space is inside the organic-rich region of the Barnett shale (Figure 1.3), and that is where gas desorption takes place. Recently, attempts have been made to study the influence of gas desorption on the flow behavior. Cipolla et al. (2010) modeled a fractured shale gas reservoir that incorporated the influence of gas desorption. They concluded that gas desorption does not play an important in the cumulative production. Later, Shabro et al. (2011) incorporated gas desorption into the mass conservation equation to model single-phase gas flow through the sphere packing method (Bryant et al., 1993). They assumed that the sphere packing was representative of the shale reservoir and predicted the gas production. Leahy-Dios et al. (2011) also studied the shale gas reservoir to better understand the importance of adsorbed gas. They presented a new model to capture multi-component sorptions from pure component data. The model was implemented in the form of the Extended Langmuir Isotherm in the unstructured grid reservoir simulator (Beckner et al., 2001).

2.9. Summary of Chapters

Chapter 3 analyzes the petrophysical properties of the tight gas sandstone measured in the laboratory. The laboratory measurements include mercury intrusion and withdrawal capillary pressures, porous plates experiment, and resistivity parameters. We indicate which laboratory measurements cannot be modeled by the conventional models such as sphere packing. Consequently, we propose our mutliscale model to capture the experimental data. Analyzing the mercury intrusion/withdrawal and porous plate results, this chapter classifies the pore structures of the tight gas sandstones into micro-dominant, intermediate, and macro-dominant. This classification shows the fraction of connected microporosity to total porosity in which the micro-dominant has the largest fraction of the connected microporosity.

Chapter 4 provides a major implication for the pore structure classification introduced in the preceding chapter. The major implication of the pore structure classification is the prediction of the ultimate gas recovery. For this purpose, we take the fraction of mercury saturation recovered after withdrawal to mercury saturation at the start of withdrawal as an approximation for the gas recovery. We then present the recovery results for the micro-dominant, intermediate, and macro-dominant pore structures. Analyzing the approximated recoveries of the pore structures, we show that the predicted recovery enhances with an increase in the fraction of connected microporosity to total porosity in the void space.

Chapter 5 investigates gas production from a Western US tight gas reservoir which was obtained from the production logging tool (PLT). The PLT shows neither gas production nor its decline rate is uniform with depth. Here, we test the notion of superior recovery from an interval with the micro-dominant pore structure. We present the results

per unit thickness of the interval for the comparison of the total production. The thickness of the producing interval is determined from logging. We will show that the production from an interval with a larger fraction of microporosity occurs with a slower rate because of lower permeability but its cumulative production is larger owing to its superior recovery.

Chapter 6 analyzes the pore structure of the shale. Similar to the study of the tight gas sandstone, we begin with the investigation of the mercury intrusion experiment (drainage) as they provide valuable insights into the topology of the void space. Consequently, we propose two pore structure models that are capable of capturing the mercury intrusion capillary pressure test. Using the proposed models, we predict the single-phase permeability and compare the predicted results with the existing data. Later, we test if our understanding of the pore structure is consistent with the scanning electron microscope (SEM) images available in the literature.

Chapter 7 investigates the effects of adsorbed layers of methane and of gas slippage at pore walls on the flow behavior in individual conduits of simple geometry and in networks of such conduits. The combined effects of adsorption and slip depend strongly on pressure and on conduit diameter. The results indicate that laboratory measurements made with N_2 at ambient temperature and 5-MPa pressure, which is typical for transient pulse decay method, overestimate the gas permeability at early life of production by a factor of 4. Moreover, the permeability increases nonlinearly as the in-situ pressure decreases during production. This effect contributes to mitigating the decline in production rate of shale gas wells.

Chapter 8 presents the concluding remarks and future work recommendations of this dissertation.

Chapter 3: Model for petrophysical properties of tight gas sandstone

3.1. Introduction

We are to analyze the laboratory measurements of tight gas sandstones such as mercury intrusion (drainage), withdrawal (imbibition), porous plate, and resistivity parameters. For this purpose, we develop a multiscale model to capture variation of the mercury intrusion capillary pressure (MICP) vs. wetting phase saturation. The model comprises a conventional network model and a tree-like pore structure (an acyclic network) that mimic the intergranular (macroporosity) and intragranular (microporosity) void spaces, respectively. Using the developed model, we explain why the capillary pressure increases almost exponentially with mercury saturation at high pressures. Implications of this model are supported by other laboratory measurements that are mercury withdrawal, porous plate, and resistivity parameters.

Applying the multiscale model to porous plate data, we classify the pore spaces of rocks into macro-dominant, intermediate and micro-dominant. These classes have progressively less drainage/imbibition hysteresis, which leads to the prediction that significantly more hydrocarbon is recoverable from microporosity than macroporosity.

3.2. Mercury intrusion capillary pressure of tight gas sandstone

In many conventional rocks, a significant range of saturation corresponds to a narrow range of capillary pressure during drainage. For instance, the wetting phase saturation (S_w), defined by $S_w = 1 - S_{Hg}$, decreases 0.7 (from $S_w = 0.9$ to $S_w = 0.2$) when the capillary pressure increases from 0.7 to 2.1 MPa in a carbonate sample shown in Fig. 1(a) (Al-Sayari, 2009). The capillary pressure is within 50 percent of a threshold pressure in percolation (Berkowitz and Balberg, 1993). The threshold pressure is 1.4 MPa in the carbonate sample. Figure 3.1(b) provides another percolation example in which the

wetting phase saturation decreases notably when the mercury capillary pressure goes up from 0.3 to 0.9 atm (±50 percent of the threshold of 0.6 atm), (Purcell, 1949). When percolation occurs, a large number of throats with capillary entry pressures smaller than the threshold pressure are accessed. These throats are not invaded at a lower pressure because access to them is only by way of narrower throats. In other words, the spatial distribution of the throats on an interconnected network is the reason for the percolation phenomenon. The existence of plateau-like trend in drainage curve, when capillary pressure versus wetting phase saturation plotted in a linear scale, is an indicator of this phenomenon (see both examples in Figure 3.1).

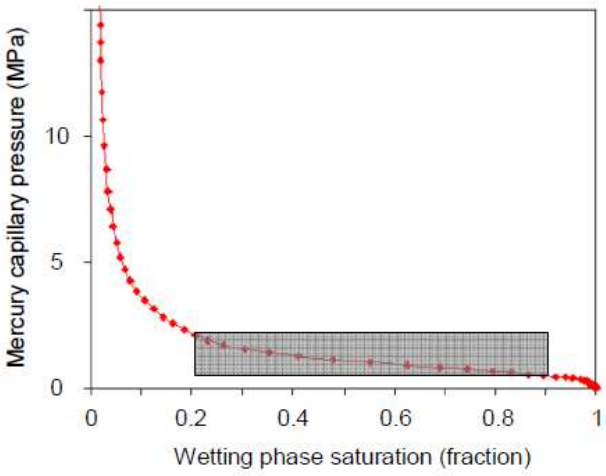

(a)

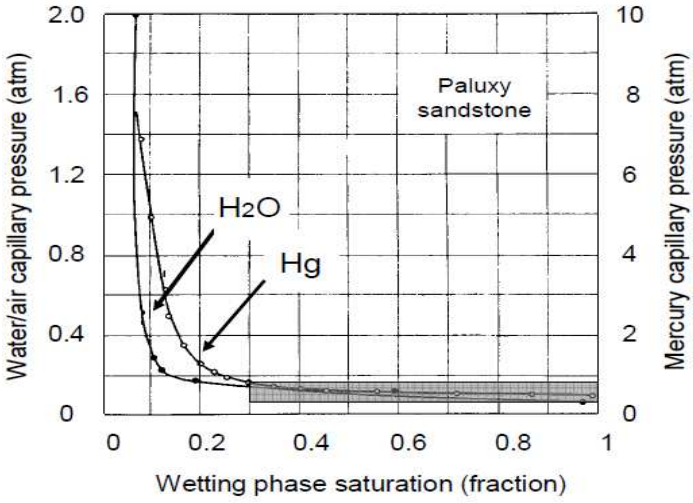

(b)

Figure 3.1: Drainage results of (a) carbonate (Al-Sayari, 2009) and (b) sandstone (Purcell, 1949) core samples obtained from mercury intrusion test. The wetting phase saturation is determined by $S_w = 1 - S_{Hg}$. (a) The mercury percolates at 1.4 MPa as the wetting phase saturation decreases from 0.9 to 0.2 (shown with gray box) when the pressure is within 50 percent with 1.4 MPa ($0.7 < P_c < 2.1$ MPa). (b) The percolation in a sandstone sample takes place at 0.6 atm during mercury intrusion. The plateau-like trend of capillary pressure with wetting phase saturation in drainage curve is an indicator of percolation.

In tight gas sandstones, the change in saturation during mercury intrusion is rarely as large as 0.7 over a correspondingly small range of capillary pressure. That is, we do not see the plateau-like trend in drainage experiments, even when capillary pressure is plotted on a logarithmic scale. Typical examples of such are shown in Figure 3.2 (see the gray boxes, which span a ±50% range of the threshold pressure). The wetting phase saturation of core #2 decreases 0.3 saturation units, from 0.85 to 0.55, when the capillary pressure is within 50 percent of 600 psi. For core #3 the decrease of wetting phase saturation is even smaller, from 0.85 to 0.6, for a similar range of capillary pressure. We say that the nonwetting phase "slightly percolates" in these conditions. More precisely, we will argue that percolation is occurring but only within a sub-network of void space in the rock, which corresponds to macro-dominated intergranular pores.

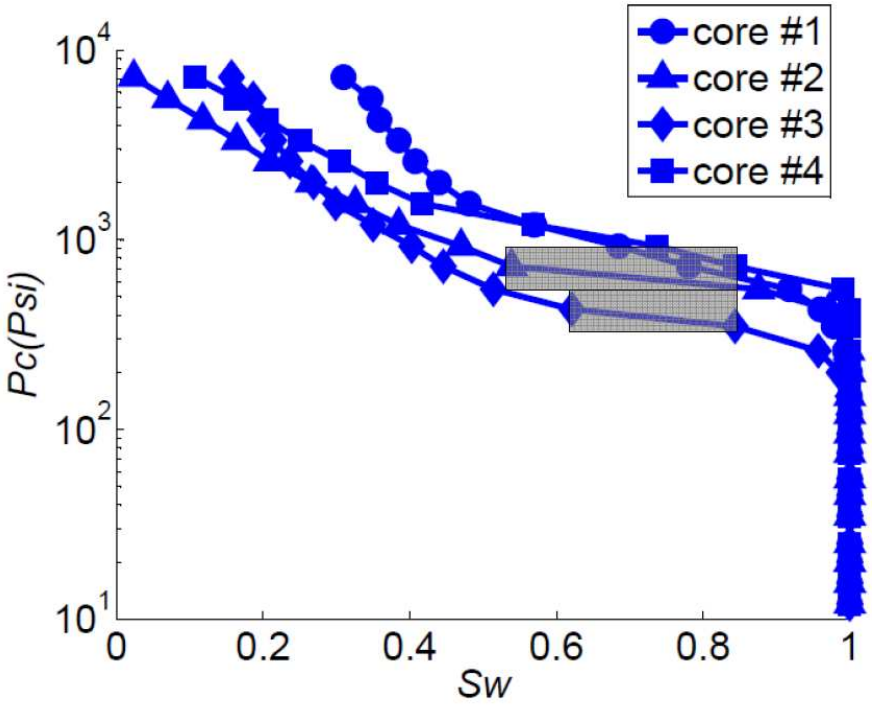

Figure 3.2: Mercury intrusion capillary pressures of confined Western tight gas sandstones versus wetting phase saturation (S_w), where $S_w = 1 - S_{Hg}$. The capillary pressure shows that partial percolations (gray boxes) take place in

cores #2 and 3. The change in saturation over a small range of capillary pressure is small compared to the conventional sample in Figure 3.1. Note the logarithmic scale on the P_c axis.

The drainage data of tight gas sandstone show that percolation does not happen over a wide range of saturation (Figure 3.2). It slightly percolates at moderate pressures. Then, the variation of the capillary pressure with saturation is exponential at high pressures (greater than 1000 psia), that is, approximately linear on the semi-log plot of Figure 3.2. This portion of the MICP corresponds to invading the microporosity region which is the intragranular void space. Figure 3.3(a) (Eichhubl, 2010) illustrates inter- and intragranular void spaces of a Western tight gas sandstone sample. From now on, we use macroporosity for intergranular void space and microporosity for intragranular void space interchangeably.

Alternative explanations for the absence of percolation are unlikely to apply to these samples. For example, percolation becomes less apparent in the MICP measurements if an operator does not give the test enough time to equilibrate. That situation is not applicable here because we are informed that enough time was given to the mercury at each capillary pressure. Samples with large surface area to volume ratios, such as irregular cuttings, can show exhibit less pronounced percolation behavior, but all the samples examined in this work were conventional plugs. Further, similar non-percolating results are available for tight gas sandstones reported by othe researchers (Cluff and Webb, 2009).

The mercury intrusion capillary pressure measurements from lab also depend on the size of a sample (Larson and Morrow, 1981; Liu et al., 1993). The percolation takes place at a larger capillary pressure for larger samples while for smaller samples, the surface effects become a crucial player (Mason and Mellor, 1995). Hence, Mason and

Mellor (1995) specified the size of a sample and later operators have adopted those specifications to report representative results for in-situ conditions. This tells us that the absence of percolation we observe here is not a because of size effect.

Understanding two-phase displacement is crucial in estimating the recoverability and its spatial variation. However, any conventional network model will exhibit percolation during drainage, and it will fail to account for drainage curves for which the pressure increase becomes almost exponential over a wide range of mercury saturation (Mousavi, 2010). We emphasize that the failure occurs regardless of how we assign the pore size distribution to the model (Mousavi 2010). The void space of the non-percolating domain constitutes almost half of the porosity as shown in Figure 3.3 and we cannot simply ignore it. Therefore, it is valuable to develop a model for capturing the capillary pressure variation over the wide range wetting phase saturation, and not only the percolating part.

3.2.1. Multiscale model of void space of tight gas sandstone

To model a two-phase displacement process in tight gas sandstones, we develop a multiscale network model which mimics both macro- and microporosity. For the large scale of the model, we use the conventional network representing the macroporosity, and for the small scale, we propose a tree-like pore structure. The notion of tree-like pore structure is introduced here for the first time in the context of tight gas sandstones and has major implications in producibility. The multiscale model is depicted in Figure 3.3(b) in which the conventional network model is shown with black lines and tree-like pore model, magnified in Figure 3.3(c), with gray circles.

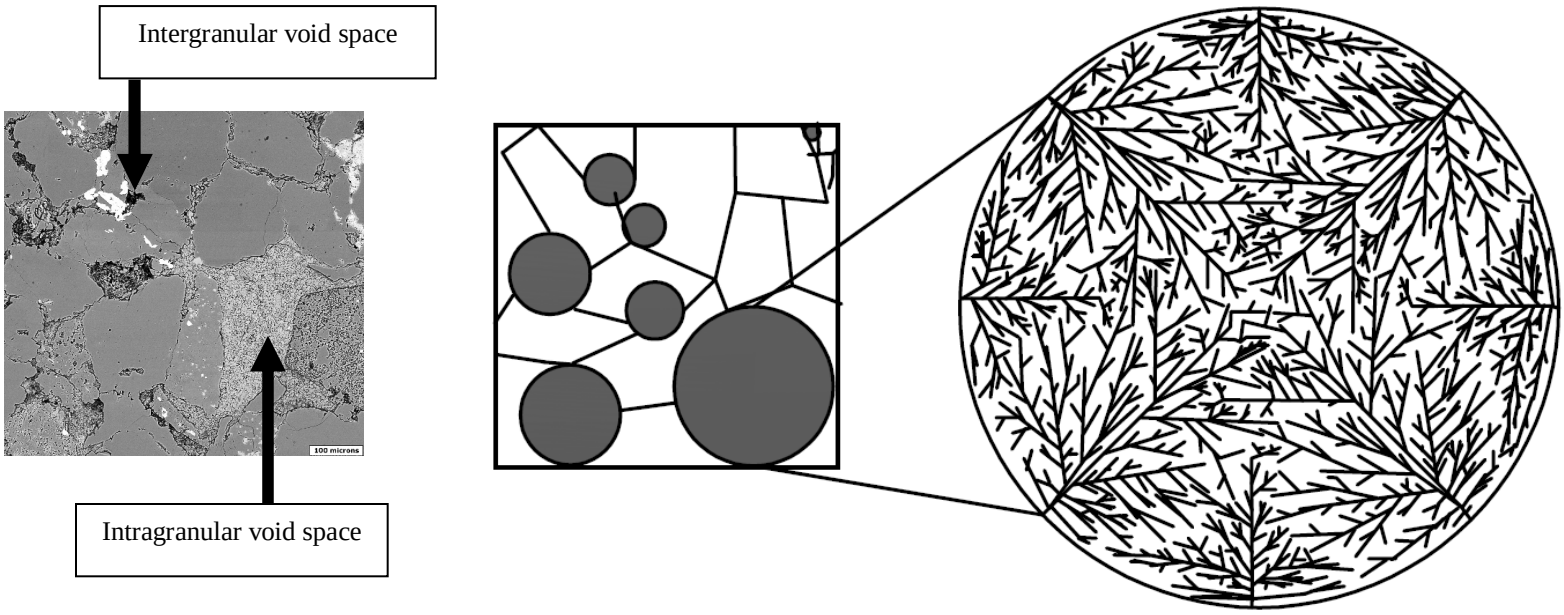

(a) (b) (c)

Figure 3.3: (a) Scanning electron microscope (SEM) image of a Western tight gas sandstone (left image from Eichhubl, 2010; scale bar at lower right = 100 micrometers). The characteristic throat sizes of the intergranular void space (macroporosity) are larger than the intragranular void space (microporosity). (b) Multiscale network model in which lines designate the intergranular void space and shaded circles the intragranular region. (c) Schematic of the tree-like pore structures that comprise the microporosity.

Depending on the fraction of macroporosity connected to total porosity, we classify the pore spaces of rocks into macro-dominant, intermediate, and micro-dominant. The schematic illustration of the corresponding multiscale model is shown in Figure 3.4. The macro-dominant pore structure has microporosity scattered upon a connected network of conventional intergranular voids. The intermediate pore family has widespread microporosity, but conventional intergranular voids also exist. Some are connected, but many are isolated between regions of microporosity. In the micro-dominant, the conventional voids are scattered and the connected paths in void space are

through microporosity. The classification indicates when the macroporosity is connected and when microporosity interferes. Thus, we expect the macro-dominant pore structure behaves more like conventional network. To clarify the difference between these models, we will explore the mercury intrusion into macro- and micro-dominant pore structures later.

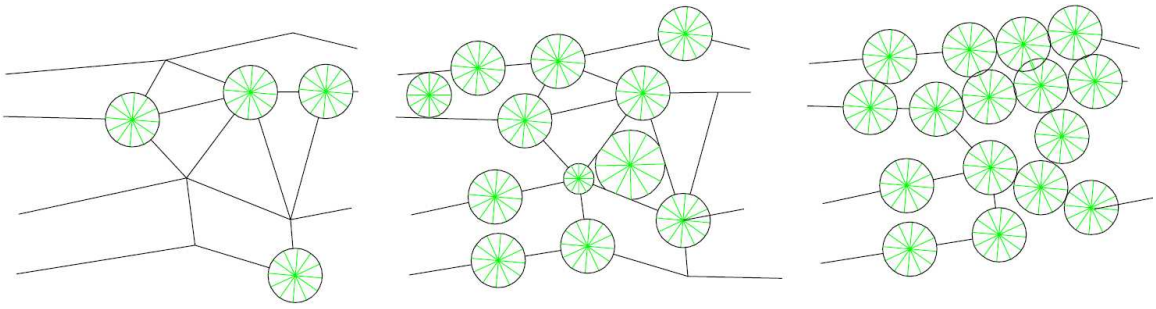

(a) (b) (c)

Figure 3.4: Multiscale network models of tight gas sandstone are classified based on the fraction of connected macro-porosity to total porosity. Black lines and wheels with green spokes represent macro-porosity and micro-porosity, respectively. (a) Macro-dominant pore space: there is widely connected network of conventional intergranular voids and the microporosity is scattered, (b) Intermediate pore space: an incomplete network of intergranular voids exists but elsewhere intergranular voids are isolated by patches of microporosity, and (c) Micro-dominant pore space: most of the voids consist of regions of micro-porosity, occasionally connected by an intergranular void.

3.2.1. Predicted MICP curves for multiscale model of void space of tight gas sandstone

First, we recall how mercury intrusion takes place in a conventional network model (see Figure 3.5). This is for the sake of completeness and more importantly, it also allows us to compare this model with tree-like pore structure. There exist numerous cycles in the network of throats; that is, starting from a pore, one or more paths lead back to that pore without retracing any segment of the path. An example of a cycle is depicted

with green arrows in (a) in Figure 3.5. Cycles in the network mean that mercury can arrive at a pore through many different paths.

We illustrate the invasion of conventional model in four steps that are at different capillary pressures. The network at the start of invasion (P_c = 0), without mercury, is shown with dashed black lines (see (a) in Figure 3.5). The line thickness represents the throat size. As the capillary pressure increases, mercury invades from left and right sides of the network. Invaded pore are accessible are depicted with red lines. Only few throats are occupied at a small capillary pressure, see (b) in Figure 3.5 where $P_c = P_1 > 0$. Mercury cannot occupy some throats that have small entry pressure because they are not (yet) accessible. There are 8 such throats and one of them is indicated by the arrow in (b) of Figure 3.5. The invasion continues as the capillary pressure increases further, see (c) in Figure 3.4 for which $P_c = P_2 > P_1$. Percolation occurs at this capillary pressure as the mercury invades a large number of throats. The throats that are not accessed at the previous step are invaded at this pressure. The spatial distribution of the pore throats is the reason for this phenomenon. The last step of the mercury intrusion is shown in (d) where all the throats are invaded at a sufficiently large P_c.

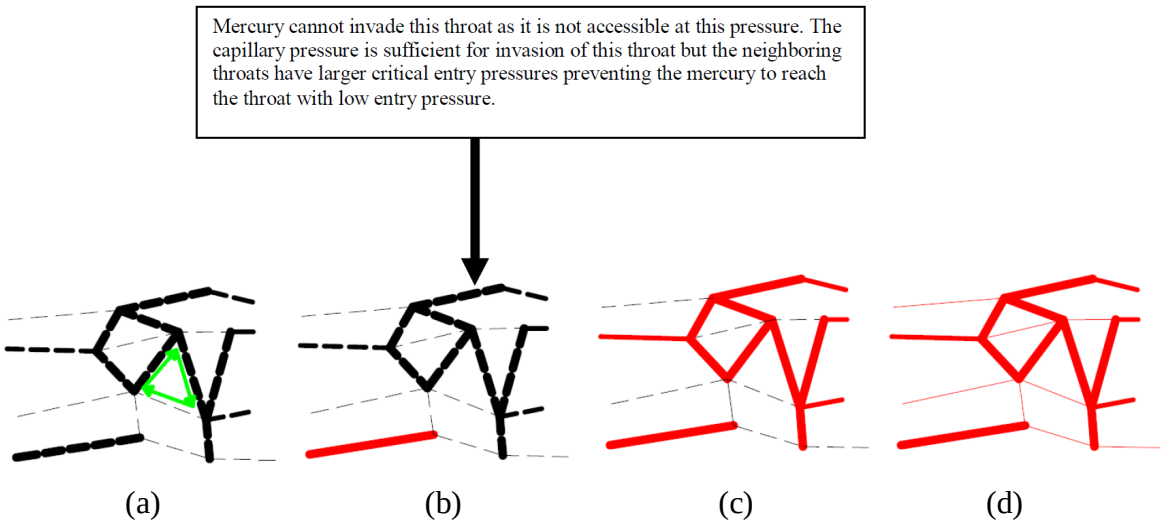

Figure 3.5: Mercury intrusion of a conventional network model in which line thickness represents the pore throat diameter. Mercury is shown with red color. There exist cycles in the conventional model which is empty initially as shown by green arrows in (a). (a) Start of mercury intrusion in which the mercury saturation in the model is zero and $P_c = 0$. (b) Nonwetting phase invades the wide throats at low capillary pressure, indicated by the one dashed line substituted with red full line, ($P_c = P_1 > 0$). Eight throats with small critical entry pressures are not invaded as they are not accessible to mercury. The surrounding throats with large entry pressures prevent mercury to reach the wide throats. (c) The invasion continues as the capillary pressure increases ($P_c = P_2 > P_1$). Percolation takes place in this step because a large number of throats are occupied. (d) This is the end of invasion as the capillary pressure is maximum ($P_c = P_{max}$) and mercury occupies all the throats.

We adopt the tree-like pore structure for the microporosity region which is the small scale of the multiscale model. The throats of tree-like pore structure have unique spatial distribution; there is no cycle in the tree-like model, in contrast to the conventional network where cycles are ubiquitous. That is, any path leaving a pore in the tree-like structure cannot return to that pore except by retracing each step. The absence of cycles means that mercury can arrive at any pore only by a single path. Further, there are multiplying branches with ever smaller throats and volume. Thus, the narrower throats are accessible only from the wider throats. These features prevent percolation from

occurring during mercury intrusion. Instead, a small increase in capillary pressure always causes a small change in saturation. As discussed below, the scaling of branch volume with branch radius leads to power law relationship between capillary pressure and saturation of the form $P_c \sim (S_{Hg})^m$. The mercury intrusion of the tree-like pore structure is depicted in four steps in Figure 3.6.

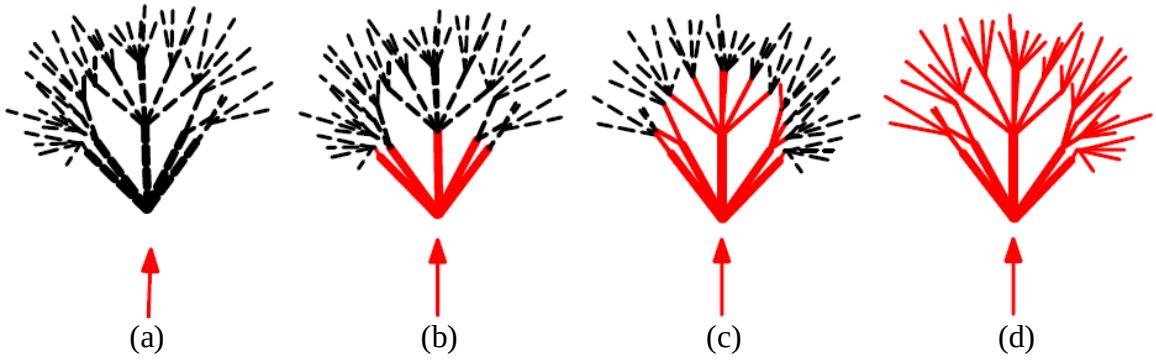

Figure 3.6: Mercury intrusion of tree-like pore model is illustrated where the nonwetting phase is shown by red color and its absence by dashed line. As in Figure 3.5, the width of each line segment is proportional to the width of the corresponding pore throat. (a) is the start of invasion ($P_c = 0$). (b) The widest throats are invaded at ($P_c = P_1 > 0$). (c) The invasion continues as the narrower throats are invaded at a larger capillary pressure ($P_c = P_2 > P_1$). (d) This is the end of mercury intrusion ($P_c = P_{max}$). The multiplying branches with ever smaller throats without cycle in the network gives power-law variation of capillary pressure with mercury saturation.

The drainage curve for a tree-like pore structure can be easily modeled. For this purpose, throat size, throat length, and the number of pore throats at each branch (n) should be specified. We do not attempt to create explicit trees with actual values of n but present the results in terms of branching number. The branching number is the ratio n_{i+1}/n_i of number of branches at two successive capillary pressures $P_{c,i+1}$ and $P_{c,i}$. In this study, our primary concern is the key qualitative behavior, namely, imbibition is a reversible process in tree-like pore structures which we will see later in the withdrawal discussion. To represent a given MICP experiment, the throat size of branches invaded at

the i^{th} capillary pressure is determined using Young-Laplace equation, $r_i = 2\sigma\cos\theta / P_{ci}$, and we assume that the throat length decreases by a factor of 2 at each branching level. The drainage results of tree-like models for three branching numbers are shown in Figure 3.7. We observe that the tree-like model leads to an exponential trend of capillary pressure with phase saturation when the branching number is defined appropriately, which is equal to 4.4 in this example.

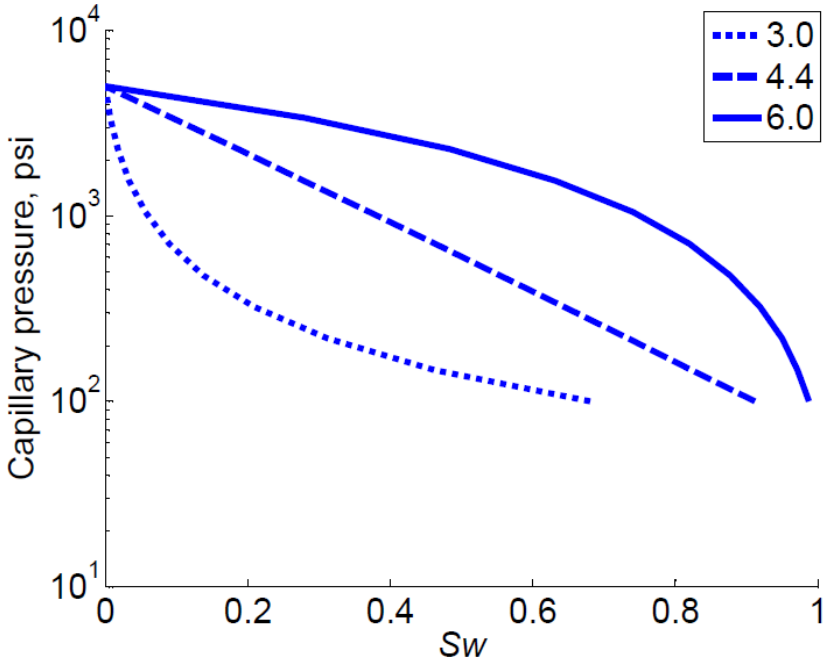

Figure 3.7: Drainage curves of tree-like pore structures (cf. Figure 3.6) with different branching numbers which is the number of branches at each node of the tree. The capillary pressure increases exponentially with mercury saturation if the branching number is between 4 and 5. The wetting phase saturation is $S_w = 1 - S_{Hg}$.

Let us analyze mercury intrusion into tight gas sandstones using multiscale network by implementing both the conventional and tree-like models. We use the macro-dominant and micro-dominant pore structures defined earlier in Figure 3.4. We show their drainages in four steps in Figure 3.8, where panel (a) corresponds to macro-dominant and panel (b) to micro-dominant. The variation of the capillary pressures (P_c)

versus wetting phase saturation (S_w) is also provided for the pore structures in Figure 3.8 (c). The mercury starts to invade the accessible wide throats first as they require low capillary pressures; see (a1) and (b1) in Figure 3.8. There is no significant decrease in the wetting phase saturation at this step for both pore structures as there are not many wide throats accessible from the boundary; see points (a1) and (b1) in Figure 3.8(c). Additional throats are invaded as we increase the capillary pressure, Figure 3.8(a2) and (b2). In the macro-dominant model Figure 3.8(a2), a significant number of throats are invaded at this pressure resulting in a percolation in the fraction of conventional network connected to outside. This leads to "partial percolation" in the multiscale model as the conventional network constitutes only a fraction of the void space of multiscale model. In the micro-dominant model Figure 3.8(b2), we do not observe a notable invasion at this pressure because the tree-like structures of very small pores mainly makes up the void space and the capillary pressure of the mercury is not sufficient to invade them. Thus, the wetting phase saturation is much smaller for the macro-dominant model (point a2 in Figure 3.(c)) than for the micro-dominant model (point (b2) in Figure 3.8(c)). Panels (a3) and (b3) correspond to a larger capillary pressure at which mercury can enter the small pores in the tree-like pore structure and conventional throats that are accessible from microporosity. The latter throats are relatively rare in both models, so the capillary pressure increases exponentially with mercury saturation which is the main feature of tree-like pore model. Note the trend of change in P_c versus S_w at this step, points (a3) and (b3) in Figure 3.8(c). Panels (a4) and (b4) illustrate the last step of drainage where all the throats are invaded. Therefore, the drainage curve of the multiscale model is more similar to that of a conventional network model, with partial percolation (points a1$\rightarrow$a2$\rightarrow$a3$\rightarrow$a4 in Figure 3.8c) rather than full percolation, or more similar to that of a tree-like pore

structure (path b1→b2→b3→b4 in Figure 3.8c), depending on the fraction of macro-porosity and its connectivity.

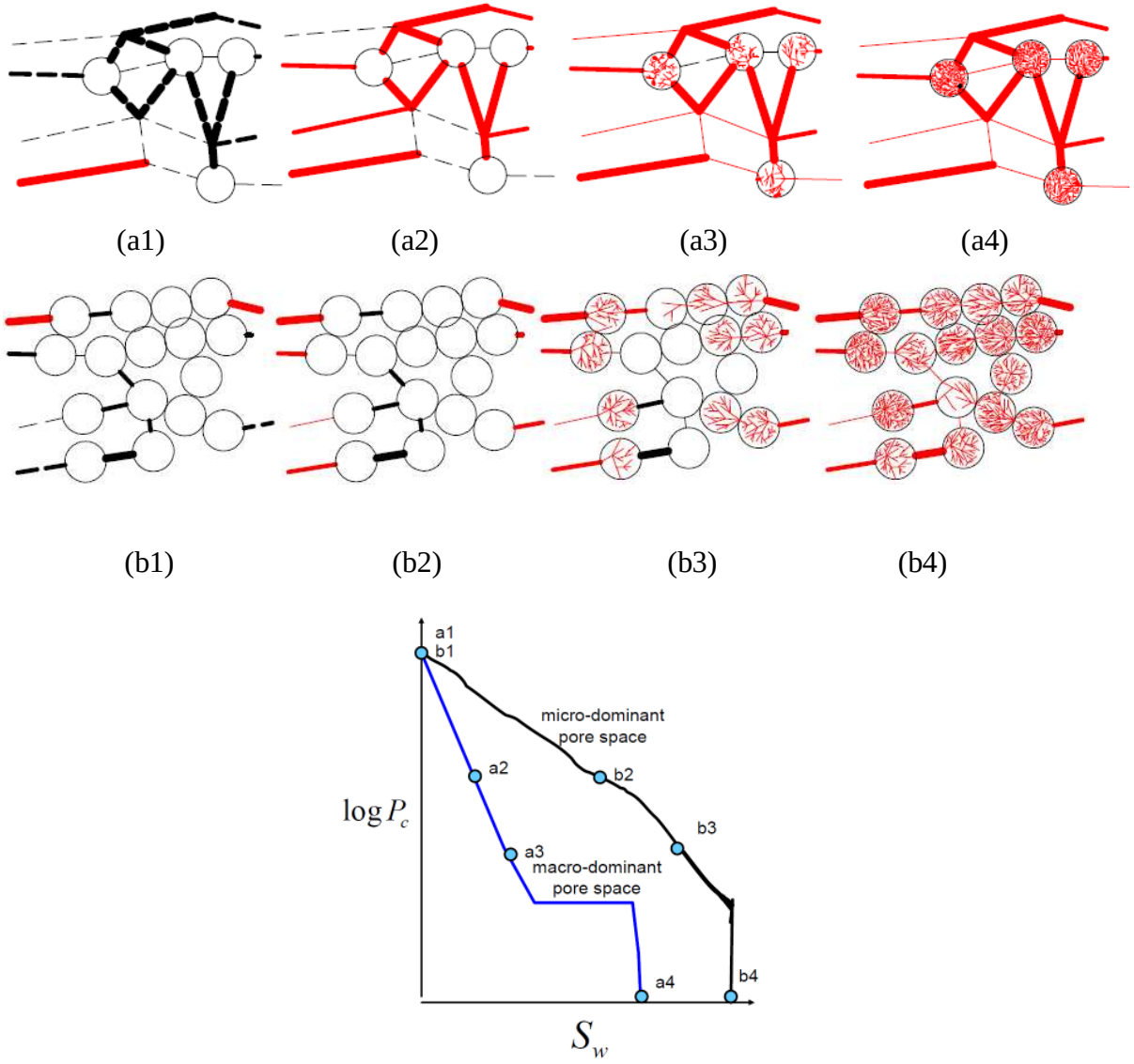

Figure 3.8: Multiscale models of macro-dominant (a1)-(a4) and micro-dominant (b1)-(b4) pore structures in mercury intrusion; corresponding drainage curves are paths a1→a4 and b1→b4 in (c). (a1) and (b1) are relevant to small capillary pressure ($P_c = P_1$) with small invasion. (a2) and (b2) refer to invasion at a larger capillary pressure ($P_c = P_2 > P_1$) where partial percolation occurs in the macro-dominant pore model (a2). The mercury intrusion of the micro-

dominant pore structure is still negligible at this pressure (see (b2)) as the void space is mainly through tree-like model. (a3) and (b3) indicate the drainage at a larger pressure ($P_c = P_3 > P_2$) where the tree-like models are occupied. (a4) and (b4) are the end of drainage ($P_c = P_{max}$) as the void space is thoroughly saturated with mercury. (c) depicts the variation of capillary pressure (P_c) with wetting phase saturation (S_w) for macro- and micro-dominant pore structures. The P_c-S_w curves of macro- and micro-dominant are provided according to the stages of invasion shown in (a1)-(a4) and (b1)-(b4), respectively.

3.2.2. Comparison with observed MICP curves

With the drainage illustrations of the multiscale models in mind, we now turn to the drainage data of tight gas sandstones shown in Figure 3.2. The wetting phase saturations, $S_w = 1 - S_{Hg}$, of core #2 decrease 0.3, from 0.85 to 0.55, and core #3 decreases 0.25, from 0.85 to 0.6, over a small range of capillary pressures. This is the partial percolation which can be captured by the macro-dominant multiscale model. The saturation change in this interval is thus interpreted as a measure of connected macro-porosity. The fraction of the connected macro-porosity is larger in the corresponding network of core #2 than in core #3. Thus, the MICP curve determines the proportion of conventional to tree-like model. We also see the drainage results of cores #1 and 4 in which the partial percolation does not occur. The micro-dominant multiscale model is appropriate for this condition as the capillary pressure increase with the wetting phase saturation is semi-logarithmic for the entire range, which is characteristic of tree-like pore model.

3.3. Mercury withdrawal of tight gas sandstone

3.3.1. Predicted mercury withdrawal from multiscale model

We illustrate how withdrawal of mercury from a conventional network model leaves some mercury behind as a residual phase in the intergranular void space. The same

phenomenon will occur within the connected intergranular voids portion of the multiscale model. Then, we describe mercury withdrawal from tree-like pore structure that constitutes the small scale of our model. Importantly, no hysteresis and therefore, no residual phase trapping occurs in the tree-like structure. Finally, by implementing the multiscale model, we indicate how it captures the mercury withdrawal from the tight gas sandstone.

We elaborate how imbibition takes place in the conventional network model here. This allows us to better understand the difference exists between this model and tree-like pore structure which we explore subsequently. First, consider the conventional network model of an intergranular void space which is initially filled with mercury, Figure 3.9(a). The thickness of each line is adjusted to show the corresponding throat size. In this model, red full lines designate the mercury and black dashed lines the absence of mercury. As mercury withdrawal begins, the smallest pores are emptied first, accompanied by withdrawal of mercury from the narrowest throats attached to those pores as their entry pressures are largest. This is indicated in Figure 3.9(b), where black dashed lines replace some of the red full lines. Then, as mercury pressure is decreased more, larger pores and wider throats attached to those pores are emptied (see Figure 3.9(c)). Figure 3.9(d) is to represent the nonwetting phase distribution when the capillary pressure is lowered to zero which is the last we consider here. The withdrawal of the mercury from any pore requires that the pore be part of the mercury phase connected to the exit (here, the left and right sides of the network). That is, we cannot withdraw the nonwetting phase if there is no path connecting it to the outside. Figure 3.9(d) exhibits this condition where the nonwetting phase (red full lines) is no longer connected to the outside; throats with nonwetting phase are surrounded by the wetting phase (black dashed line). As a result, this fraction of the nonwetting phase stays in the void space as residual,

regardless of how much the mercury pressure is decreased. The ratio of the void space of the network containing nonwetting phase (red full lines) to the entire void space in part (d) of Figure 3.9 is the residual nonwetting phase saturation (S_{nwr}). The network model holds the nonwetting phase as residual because of the spatial distribution of sizes of the throats and, more fundamentally, the lattice-like structure of the network. The lattice guarantees many alternate paths from any given throat to the outside. Thus, it is often possible to withdraw mercury from a small pore in the interior of the network and thereby disconnect mercury in a larger adjacent pore. A series of such disconnections leads to the complete isolation of volumes of mercury.

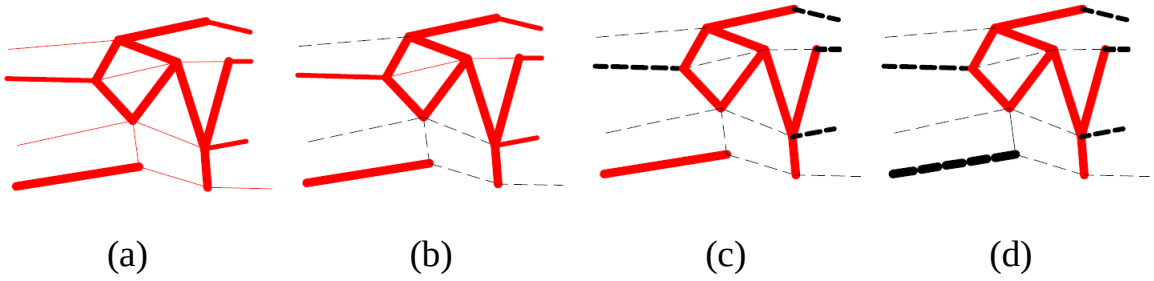

Figure 3. 9: Mercury (red color) cannot be completely withdrawn from a conventional network because it becomes disconnected. Line thickness indicates pore throat diameter and dashed line the absence of the nonwetting phase. (a) Start of imbibition in which the void space is fully saturated with nonwetting phase. (b) Nonwetting phase leaves the smaller pores by way of narrow throats (dashed lines) as the capillary pressure decrease. The nonwetting phase withdrawal continues as we lower the capillary pressure shown in (c). (d) End of imbibition in which the nonwetting phase remains in the void space as residual because there is no connected path of the nonwetting phase to the outside through which it can be displaced. The spatial distribution of the pore throats and the topology of a network are the reasons for the phenomenon.

Now, we analyze the mercury withdrawal from tree-like pore structure. See Figure 3.10 in which the mercury is shown by red full line and its absence by dashed black line. The thickness of the line of the network is intended to represent the throat size.

Suppose that the void space is initially saturated with the nonwetting phase (see Figure 3.10(a)). Then, mercury withdraws first from the narrowest throats as the capillary pressure is decreased. Some red full lines are replaced by dashed black lines to indicate this in Figure 3.10. Progressively wider throats are evacuated as the capillary pressure decreases. Because smaller throats are only accessed from wider throats, the nonwetting phase remains connected in all steps ((a)-(d) of Figure 3.10). This is possible only because the tree-like structure contains no cycles. This behavior differs qualitatively from the conventional model of Figure 3.9. Consequently, we can withdraw all the nonwetting phase from the pore space. That is, the mercury intrusion and withdrawal is completely reversible in the tree-like void space. The reversibility of the nonwetting phase withdrawal is favorable for gas production as the hydrocarbon can be completely recovered from this type of porosity, even as aqueous phase imbibes into the pore space.

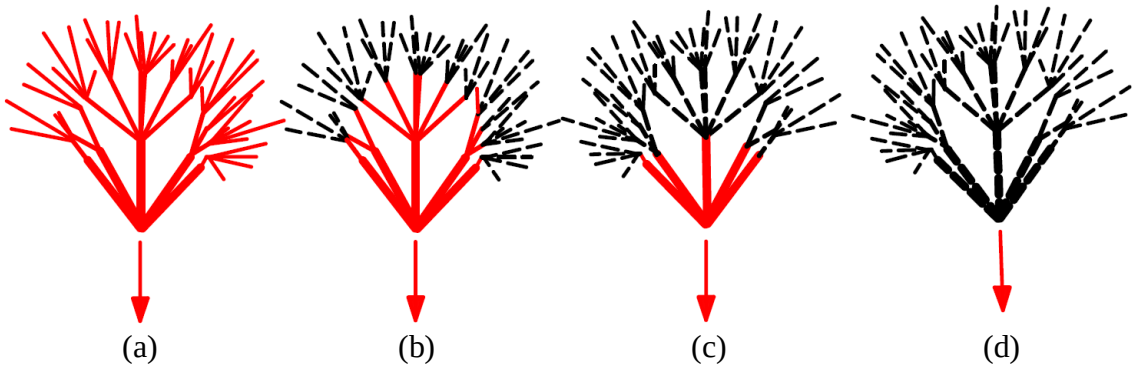

Figure 3.10: The mercury withdrawal from tree-like pore space is shown in three steps. The red color denotes the nonwetting phase and the dashed black line represents an absence of nonwetting phase, similar to Figure 3.9. (a) illustrates fully saturated pore model at the start of mercury withdrawal ($P_c = P_{max}$). (b) The narrowest throats are evacuated as the capillary pressure is reduced ($P_c = P_1 < P_{cmax}$). (c) The withdrawal continues as capillary pressure decreases ($P_2 < P_1$). (d) This is the end of mercury withdrawal ($P_3 = 0$) at which the non-wetting phase is completely withdrawn. The topology of the tree (it has no cycles) and the ordering of the throat sizes ensures that nonwetting phase in all steps is connected to the exit. Thus, unlike the

network shown in Figure 3.9, the withdrawal from tree-like pore structure does not leave a residual phase.

The conventional network model exhibits percolation in drainage (Figure 3.5) and residual mercury saturation in imbibition (Figure 3.9). We have further learned that the tree-like pore structure exhibits gradual (no percolation) and reversible mercury intrusion/withdrawal (Figure 3.6 and Figure 3.10). Implementing these concepts, we now analyze the mercury withdrawal from the multiscale network model. The macro-dominant and micro-dominant models are analyzed in Figure 3.11. We previously explored the mercury intrusions of these models in Figure 3.8. Figure 3.11(a1) and (b1) are the start of mercury withdrawal in which the models are fully saturated with nonwetting phase ($P_c = P_{max}$). See Figure 3.11(c) in which points (a1) and (b1) show the start of imbibition for macro- and micro-dominant pore structures, respectively. The mercury leaves the tree-like pore structure as we lower the capillary pressure, Figure 3.11(a2) and (b2). In this step, mercury is withdrawn only from the pores of tree-like model as their characteristic sizes are smaller (compare (a2) with (a1) and (b2) with (b1)). The increase in the wetting phase saturation is smaller for the macro-dominant than for the micro-dominant pore structures because the tree-like structures makes up a smaller fraction of porosity in the former; compare points (a2) and (b2) in Figure 3.11(c). Figure 3.11(a3) and (b3) show the situation at still lower capillary pressure where the tree-like pore structure is emptied of mercury. Here, the mercury occupying the conventional network that is accessible only through the tree-like model becomes disconnected. At the end of this step, we begin to withdraw the mercury from the fraction of the conventional network model accessible to the outside. Note the trend of P_c versus S_w in macro- and micro-dominant pore structures. Figure 3.11(a4) and (b4) show the end

of imbibition with zero capillary pressure in which the mercury remains as a residual phase in the connected network portion of the pore space, while the mercury is fully withdrawn from the tree-like pore model. Therefore, the residual nonwetting phase is much smaller in the micro-dominant pore structure, Figure 3.11(b4), as the corresponding network is mainly composed of tree-like pore model, compared to the macro-dominant pore structure, Figure 3.11(a4).

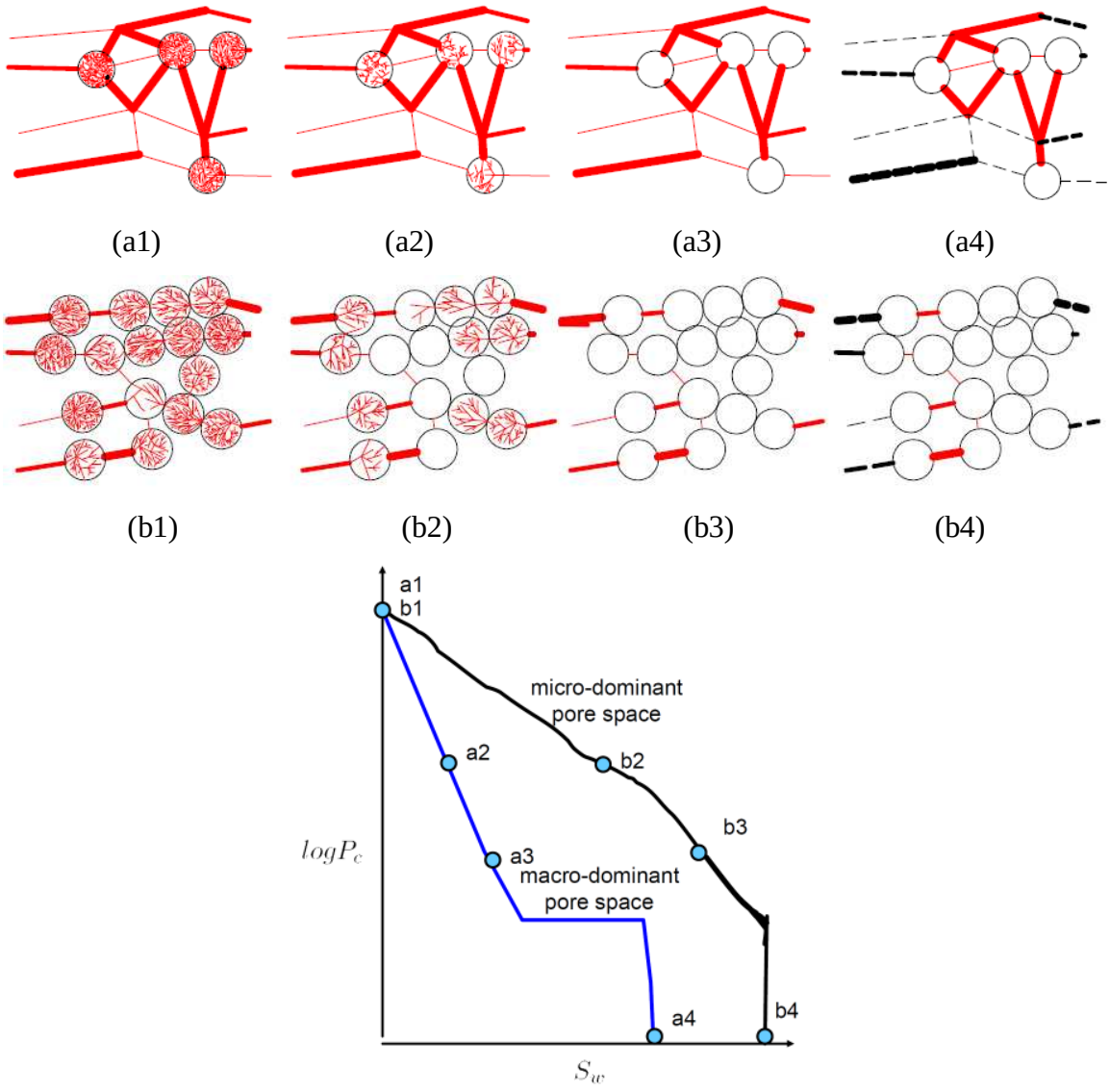

Figure 3.11: Mercury withdrawal from macro-dominant (a1)-(a4) and micro-dominant (b1)-(b4) multiscale models. Corresponding imbibition curves a1→a4 and b1→b4 in (c). (a1) and (b1) are fully saturated with mercury ($P_c = P_{max}$). (a2) and (b2) depict the models at a lower capillary pressure ($P_c = P_3 < P_{max}$). Mercury leaves the smallest pores of tree-like models by withdrawing through the smallest pore throats. (a3) and (b3) are relevant to a lower capillary pressure ($P_c = P_2 < P_3$) where mercury withdrawal continues; in (a3) the nonwetting phase of the conventional network of pore throats that is accessible only from the tree-like pore model becomes disconnected. No

such disconnection occurs in (b3). (a4) illustrates the residual mercury phase at zero capillary pressure which remains in the conventional model while (b4) shows that all mercury is withdrawn at zero capillary pressure. (c) shows decrease of the capillary pressure with wetting phase saturation for the macro- and micro-dominant pore models. This plot distinguishes the imbibition results based on the pore structures, which is usually taken into account in reporting the imbibition results (Lake, 2010).

3.3.2. Observed mercury withdrawal in samples

In light of the preceding models, consider the mercury intrusion/withdrawal measurements under confining stress shown for two Western tight gas sandstones in Figure 3.12. We assume that the effect of disjoing pressure is negligible (Derjaguin and Churaev, 1974). During intrusion, the capillary pressure of the sample with a larger entry pressure increases almost exponentially with mercury saturation and there is no percolation. Then, the capillary pressure of the sample decreases almost exponentially with mercury saturation during withdrawal, almost reversing the path following during intrusion. These are the characteristic features of the tree-like pore structure. The slight irreversibility at the end of the intrusion/withdrawal cycle is because of a small amount of intergranular void space that is accessible only through the intragranular void space; cf. Figure 3.11(b4). In other words, a small fraction of the void space in this sample is embedded in a conventional network of voids which is accessible only from tree-like pore structure. The cumulative disconnection of mercury in these voids results in the final residual saturation of about $S_{nwr} = 0.10$. Therefore, a micro-dominant multiscale network model, with a large fraction of void space embedded in the tree-like pore structure, represents the void space in this sample.

In contrast, tight gas sandstone samples that are not dominated by microporosity show strong hysteresis during mercury withdrawal and very large residual saturations. The sample with a smaller entry capillary pressure in Figure 3.12 is an example of such.

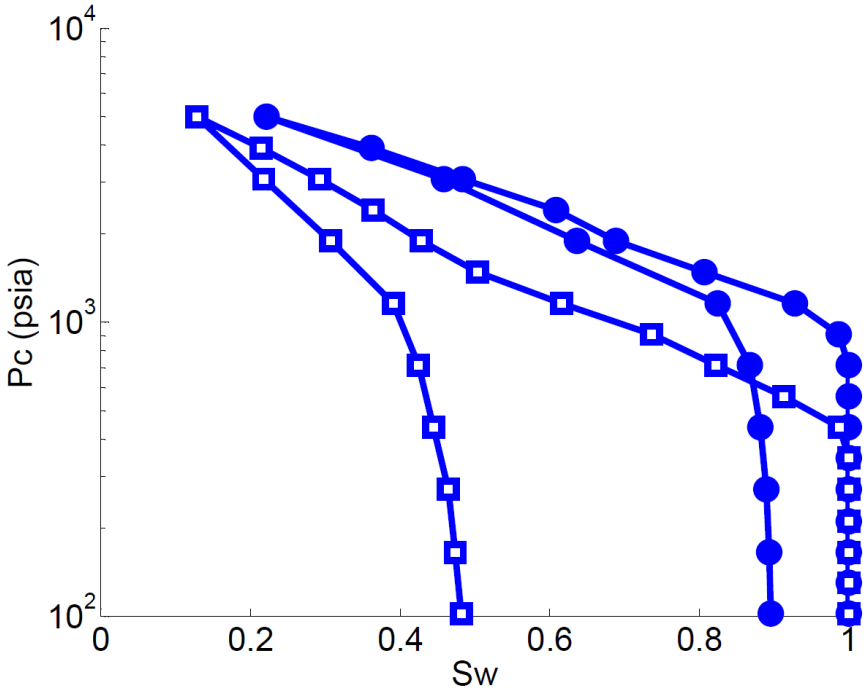

Figure 3.12: Mercury intrusion and withdrawal data on samples of two Western tight gas sandstones held under confining stress. The capillary pressure increases exponentially with mercury saturation during intrusion for both samples. The withdrawal is almost reversible for the sample with a larger entry pressure (filled symbols) until the mercury saturation ($1 - S_w$) reaches 0.10. The reversible intrusion/withdrawal over a large range of mercury saturation is indicative of void space dominated by microporosity. In contrast, strong hysteresis for the sample with a smaller entry pressure (open symbols) reveals that the macroporosity mainly constitutes the void space in that sample.

3.4. Porous plate experiment and its relation with mercury intrusion

This section examines our understanding of the pore structure which is based on the multiscale model. We first predict the drainage results of tight gas sandstone obtained

from mercury intrusion and porous plate experiments on a consistent set of samples. Then, we contrast our prediction with the measured data.

3.4.1. Predicted porous plate experiment from multiscale model

In the porous plate, air is invaded into a sample fully saturated with brine. Air is the nonwetting phase for tight gas sandstone and brine is wetting. Thus, this experiment is drainage. We predict the drainage results here from the multiscale model.

First, we suppose that there is no clay swelling occurring during the porous plate experiment. Consider the displacement of brine by gas within the tree-like pore structure of the microporosity. The microporosity is filled with water at the start of porous plate test as depicted in Figure 3.13(a). As drainage begins, gas displaces brine from the relatively large throat that connects the tree-like structure to the exit, Figure 3.13(b). However, gas cannot invade the microporous void space, no matter how large the capillary pressure is, as the brine has no way out. The gas also cannot compress the brine inside the pore space enough to enable significant saturation changes. Therefore, the pore structure of the tree-like model predicts that a significant faction of void space is not accessible in the porous plate, simply because the brine is trapped in the microporosity.

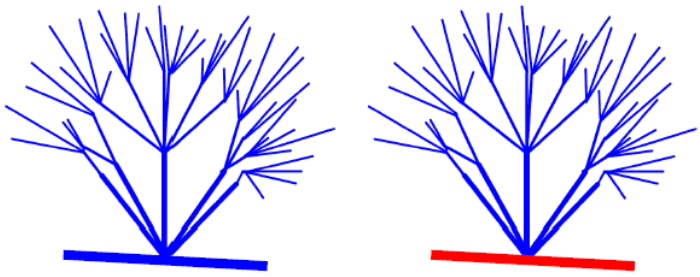

(a) (b)

Figure 3.13: (a) Schematic illustration of the tree-like pore structure which is initially saturated with brine and connected to a larger pore (thick line) also contains brine. (b) Gas drains the large throat (red) but cannot invade the tree-like void space as brine has no way out.

The trapped phase phenomenon in the porous plate experiments does not occur in the mercury intrusion test because the sample is initially evacuated. Therefore, the capillary pressure of the nonwetting phase only needs to be large enough to exceed the capillary entry pressure of the throat. There is no resident fluid that must be displaced from the void space.

Now, we assume that a notable clay swelling takes place in the microporosity region. If this is the case, the void space embedded in the microporosity is available during mercury intrusion but is no longer available in the porous plate experiment. The clays swell and occupy the adjacent void space and hence, the porosity existing in the tree-like fraction of the multi-scale model vanishes. This provides another reason for the samples having larger wetting phase saturations in porous plate than in mercury intrusion tests at similar scaled capillary pressures. Therefore, the multiscale model predicts significantly larger wetting phase saturation in the porous plate experiment.

3.4.3. Observed porous plate experiment

We now turn to the comparison of drainage results obtained from porous plate experiment and mercury intrusion. This is to test the prediction of multiscale model. For this purpose, we analyze the drainage data in the form of scaled capillary pressure. The scaled pressure presentation eliminates the difference in interfacial tensions (gas/water versus Hg/Hg vapor) and allows us to compare the accessible void space controlled by the same set of throats in both experiments. The scaled capillary pressure after assuming equilibrium is calculated as:

$$P_{cs} = \frac{P_c}{\gamma \cos\theta} \tag{3.1}$$

where P_{cs} is the scaled capillary pressure, P_c the capillary pressure obtained from laboratory measurements, γ interfacial tension, and θ the contact angle. The interfacial tension of air-brine is equal to 72 $\frac{dynes}{cm}$ and for mercury-mercury vapor, it is 487 $\frac{dynes}{cm}$. The contact angles of air-brine and air-mercury are 0 and 140 degrees, respectively. Knowing the capillary pressures from laboratory measurements, we determine the scaled pressures.

The drainage curves of mercury injection and porous plate for a set of samples of a Western tight gas sandstone are shown in Figure 3.14 in the scaled form. The wetting phase saturation in mercury intrusion is evaluated from mercury saturation, $S_w = 1 - S_{Hg}$, and in the porous plate, it is brine saturation. We observe a significant decrease in the invaded void space of the porous plate compared to mercury intrusion. The average difference in drainage endpoints is almost 0.4 saturation units between the two sets of experiments. The difference is because of brine being trapped in the samples and/or clay swelling. This corroborates our understanding from the pore structure of tight gas sandstone which is based on multiscale model.

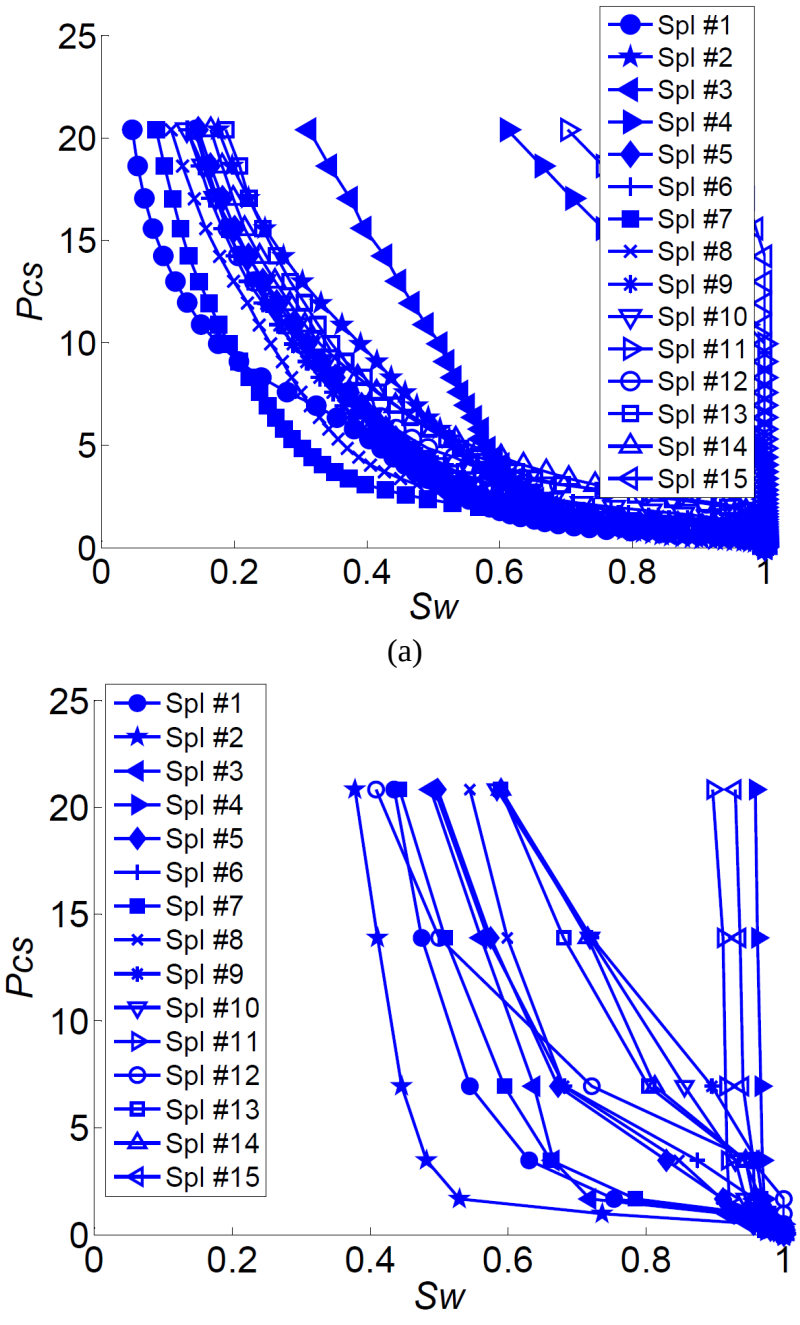

(a)

(b)

Figure 3.14: Drainage curves for a set of samples of a Western tight gas sandstone measured by (a) mercury intrusion and (b) porous plate. The capillary pressures are scaled by interfacial tension and contact angle using Equation (3.1). The average wetting phase saturation at the maximum scaled pressure is 0.35 saturation units smaller for the porous plate than for mercury intrusion. This is because of the brine trapped in the tree-like microporosity.

3.4.4. Pore structure classification based on porous plate experiment

Here, the pore structure of tight gas sandstones is categorized by comparing the drainage results. We categorize the porosities of the core samples into macro-dominant, intermediate, and micro-dominant depending on the wetting phase saturation, which is brine saturation, at the maximum scaled capillary pressure. These terms are used to indicate the fraction of porosities only relative to each other. So the term macro-dominant means that the fraction of macroporosity in that pore structure is greater than in the other groups. We do not mean that the void space is made up macroporosity similar to conventional rocks. In this classification, we also consider the trend of capillary pressure variation with wetting phase saturation.

The void space is macro-dominant if the partial percolation takes place at low capillary pressure. Figure 3.15(a) depicts examples of such. On the other hand, the invasion is negligible if the void space is mainly microporosity (see (c) in Figure 3.15). Other pore structures are considered intermediate in which the partial percolation does not occur but the wetting phase saturation at the largest capillary pressure is comparable with macro-dominant pore structure (Figure 3.15(b)). For instance, the final wetting phase saturations of intermediate pore structures are in the range of 0.4 to 0.65 while for macro-dominant they are 0.4 to 0.6. Implementing the pore structure classification to 15 samples, we find that 4 are macro-dominant, 8 are intermediate, and 3 are micro-dominant.

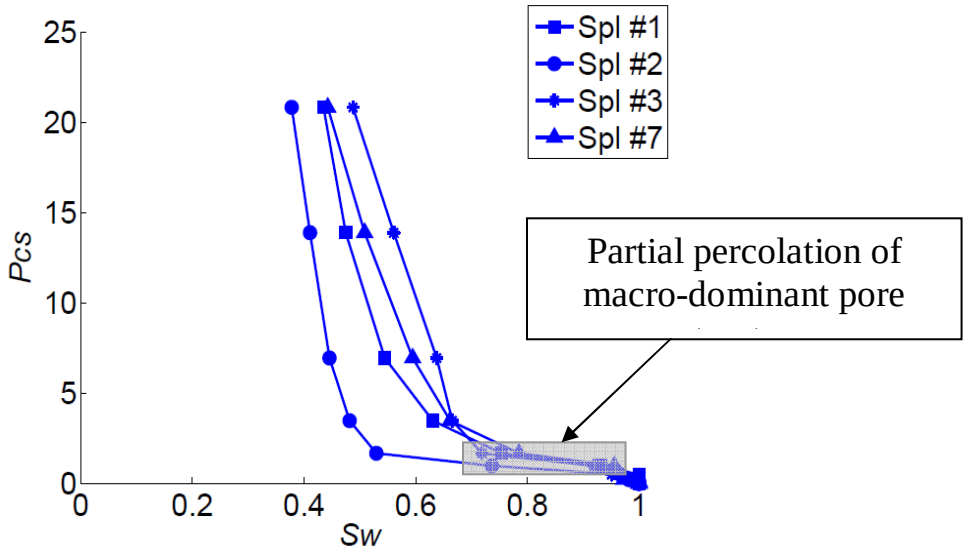

(a)

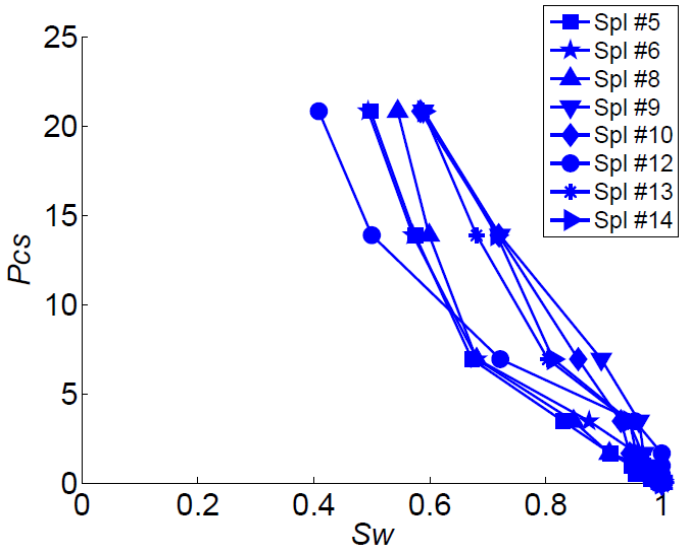

(b)

Figure 3.15

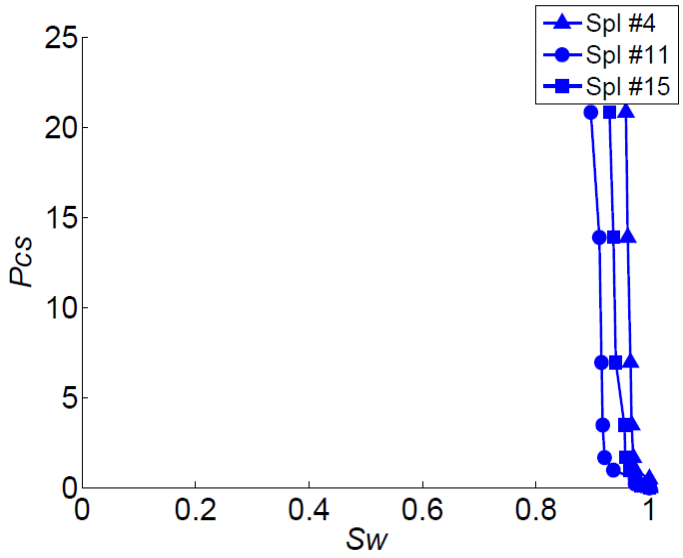

(c)

Figure 3.15: The void space of tight gas sandstone is classified based on the porous plate experiment. (a) is the macro-dominant void space in which the partial percolation (gray box) and large irreducible brine saturations are obvious, (b) the intermediate structure showing no percolation but large irreducible saturations, and (c) the micro-dominant pore structure without notable invasion. Core samples are labeled as in Figure. 3.13.

3.5. Absolute gas permeability and its relation with pore structure classification

In this section, we examine the correlation of absolute gas permeability and pore structure. This is to examine whether the fraction of microporosity determined from porous plate data is reflected in the absolute permeability. We expect the permeability decreases as the microporosity fraction increases.

We compare the average gas permeability values of the pore structures. The average (logarithmic mean) permeabilities of the samples in macro-dominant, intermediate, and micro-dominant pore structures are respectively, 8.0, 4.7 and 2.5 microD. This shows that the characteristic throat sizes of macro-dominant pore structure are the largest. So the connected void space, compared to other samples, is more through the macroporosity. We also note that the micro-dominant pore structure has the lowest

permeability indicating the largest fraction of microporosity in this pore structure. Hence, the average permeability values are consistent with our pore structure classification in indicating the fraction of microporosity.

To summarize the development thus far, we have described a multiscale model that captures characteristic features of the mercury intrusion capillary pressure test. The model allows us to explain features of the mercury withdrawal as well. Implementing this model, we explained why a significant fraction of void space is not accessible to the invading nonwetting phase in the porous plate, compared to mercury intrusion. Then, we classified the pore structures of the rocks into macro-dominant, intermediate, and micro-dominant. This classification is supported by the average absolute gas permeability values. We next use this approach to estimate the ultimate recovery of tight gas sandstone and validate it via analyzing production data.

3.6. Resistivity analysis

In this section, we examine whether the resistivity parameters are correlated with the pore structure. If a resistivity signature can be identified, it could be used to categorize logged intervals in terms of the pore space structures. This section is only to examine whether the pore structures are classified based on the resistivity parameters. Of course, we do not mean that all the resistivity parameters obtained from lab measurements provide meaningful values for tight gas sandstones similar to conventional rocks.

3.6.1. Cementation exponent

The formation factor indicates the resistivity of a fully brine-saturated sample against electrical current. It depends on the conductivity of saturated throats and

conductive grains, if the latter exist. The formation factor is commonly treated as a power law in porosity:

$$F = \frac{a}{\varphi^m} \tag{3.2}$$

a is a constant and m the cementation exponent. Here, the constant a is taken to be unity, and the cementation exponent is obtained from the laboratory measurements of F and ϕ.

We present the cementation exponent data of the pore structures in Table 3.1. The average value (arithmetic mean) of the cementation exponent is large for macro-dominant and intermediate pore structures and small for micro-dominant; the cementation exponent decreases with the fraction of connected microporosity. Thus, the cementation exponent data, similar to the absolute gas permeability values, are correlatable with the pore structures determined from drainage experiments. The value near 2 for the macro-dominant and intermediate is consistent with values for conventional networks. The smaller values of m for the micro-dominant samples are consistent with the fact that m = 1 for the bundle-of-tubes model of pore space, which in terms of conduction is analogous to the tree-like pore structure.

Table 3.1: The average (arithmetic mean), minimum, and maximum of the cementation exponents of Western tight gas sandstone samples. The pore structures were determined from the porous plate results provided in Figure 3.15.

	Macro-dominant	Intermediate	Micro-dominant
Average	1.80	1.79	1.48
Min	1.70	1.56	1.45
Max	1.89	1.85	1.51

3.6.2. Resistivity index

The resistivity index is the ratio of the resistivity of the partially brine-saturated core to its fully saturated condition. The resistivity index is commonly parameterized with brine saturation as:

$$RI = \frac{1}{S_w^{\,n}} \tag{3.3}$$

where RI is the resistivity index, S_w the wetting phase saturation, and n the saturation exponent. The saturation exponents for the same set of samples classified by pore structure are listed in Table 3.2. The saturation exponent follows a monotonic trend based on the pore structure classification. It decreases as the fraction of microporosity increases, with micro-dominant having the lowest average value, showing that the pore classification is also capable of ordering the electrical resistivity parameters of the rocks.

Table 3.2: The average (arithmetic mean), minimum, and maximum of saturation exponents of 15 samples of Western tight gas sandstone. Samples are classified as macro-dominant, intermediate, and micro-dominant pore structure based on Figure 3.15.

	Macro-dominant	Intermediate	Micro-dominant
Average	1.58	1.50	1.32
Min	1.40	1.38	1.28
Max	1.66	1.61	1.41

The analyses of cementation exponent and resistivity index show that pore structures are classified according to these parameters. As we will see in the subsequent section, this pore classification has major implication in terms of producibility. Analysis

of resistivity logs could therefore be useful in assessing the pore structure, though such analysis is beyond the scope of this paper.

3.7. Conclusions

We have analyzed the pore structure of the tight gas sandstone. To this end, we have developed a multiscale model to analyze macroporosity (primarily intergranular void space) and microporosity (primarily intragranular void space) and their interactions. The multiscale model embraces conventional network model and tree-like pore structure to mimic the intergranular and intragranular void spaces, respectively. The tree-like pore structure is proposed in this study for the first time.

We have adopted the multiscale model to analyze the laboratory measurements such as mercury intrusion (drainage), withdrawal (imbibition), porous plate, and resistivity parameters. Applying the multiscale model to porous plate data of drainage experiment, we have classified the porosities of rocks into macro-dominant (large macroporosity fraction), intermediate (combination of macro and microporosity), and micro-dominant (large microporosity fraction). Each class has different imbibition behavior and hence different expected gas recoveries. This is has major implications in terms of predicting ultimate recovery from the reservoir. We will quantify the estimated ultimate recovery (EUR) of the tight gas reservoir in the subsequent chapter using the mercury intrusion/withdrawal data.

Chapter 4: Estimation of ultimate recovery for tight gas sandstone

4.1. Introduction

We are to see the main implication of the multiscale model which we originally developed to explain the mercury intrusion capillary pressure (MICP) measurements of the tight gas sandstone. The main implication is to indicate how pore structure classification introduced from the notion of multiscale model along with mercury intrusion/withdrawal allows us to predict the ultimate recovery.

We use the residual mercury saturation of the mercury withdrawal test (S_{gr}) to evaluate producibility of each pore structure. We use the ratio of residual mercury saturation after mercury withdrawal (S_{gr}) to initial mercury saturation (S_{gi}), which is the saturation at the start of withdrawal, as a measure of gas likely to be trapped in the matrix during production and hence a proxy for estimated ultimate recovery (EUR). This is the EUR considering the capillary effects only from the matrix of a tight gas sandstone. We first calculate the recovery of the pore structure using mercury intrusion/withdrawal tests. Then, we evaluate the recovery from different initial gas saturations by investigating measurements of cyclic mercury intrusion/withdrawal.

4.2. Methodology

4.2.1. Estimation of ultimate recovery from residual mercury saturation after withdrawal

We estimate the ultimate recovery of pore structures from residual mercury saturation (S_{nwr}) of intrusion/withdrawal test. The variation of residual mercury saturation with absolute gas permeability of the core samples is illustrated in Figure 4.1. Because the porous plate data were not measured for these samples, the demarcation of S_{nwr} for each category is made by distributing pore types to have the same population distribution as observed in the porous plate samples (see Figure 3.15). In this demarcation, the

populations with the largest residual mercury saturations correspond to macro-dominant, medium residual saturations represent intermediate, and the smallest residual saturation tally with micro-dominant pore structures. Examples of mercury intrusion/withdrawal results for the pore structures are provided in Figure 4.2. In the porous plate pore structure classification implemented for 15 samples, 3 are in micro-dominant group, 8 in intermediate, and 4 in macro-dominant. Hence, from the 35 samples for which we have the mercury withdrawal results the populations of macro-dominant, intermediate, and micro-dominant are 9, 19, and 7, respectively. Using this population criterion, we draw lines between the pore types on Figure 4.1. The coincidence of the lines with "round numbers" on the y-axis is not deliberate.

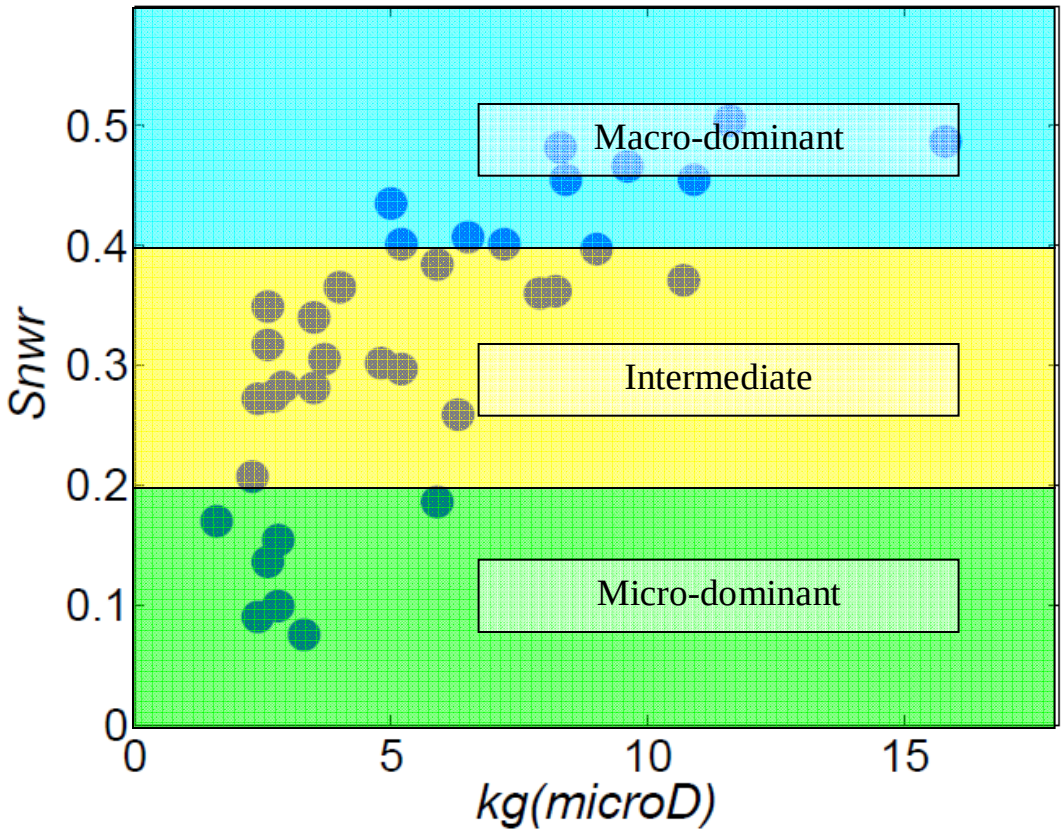

Figure 4.1: Variation of residual mercury saturation (S_{nwr}) with absolute gas permeability for samples of Western tight gas sandstone. Macro-dominant has the largest fraction of connected intergranular void space resulting in the largest S_{nwr}. From 35 core samples, 9 are macro-dominant, 19 intermediate,

and 7 micro-dominant. The frequency distribution of pore structures is adopted from the porous plate samples.

We use mercury intrusion/withdrawal results for estimating gas recovery. We take residual nonwetting phase saturation at the end of mercury withdrawal (S_{nwr}) as an estimate of the residual gas saturation (S_{gr}). This is reliable when the initial nonwetting saturation (S_{nwi}) of the test is close to initial gas saturation (S_{gi}). The recoverable fraction of nonwetting phase depends on both pore structure and initial nonwetting phase saturation. The recoverable fraction of the nonwetting phase is the complementary part of the ratio of S_{nwr} to S_{nwi} (i.e., recoverable fraction = $1 - \frac{S_{nwr}}{S_{nwi}}$). We will generalize this approach to partial cyclic intrusion/withdrawals in the subsequent section.

We illustrate the procedure for micro-dominant, intermediate, and macro-dominant pore structures. The results of mercury intrusion/withdrawal for the three samples are shown in Figure 4.2. The nonwetting phase saturation of the micro-dominant pore structure is 77% at the start of withdrawal. We take this as S_{gi}. Then, we take the nonwetting phase saturation at the end of withdrawal to be S_{gr} which is 21% for the micro-dominant sample. Hence, the fraction of residual to initial nonwetting phase saturations is 0.21/0.77 = 0.27. This indicates the fraction of original nonwetting phase that is irrecoverable. Hence, 73% (= 100% – 27%) of the initial gas saturation is recoverable when the initial gas saturation is 77%. For the intermediate pore structure, the nonwetting phase saturations at the start and end of imbibition are, respectively, 77% and 30%. This implies that 39% of the initial nonwetting phase is irrecoverable, so 61% of the original nonwetting phase is producible. The macro-dominant pore structure shows that its nonwetting phase saturation at the start and end of drainage and imbibition equal 87% and 50%, respectively. Therefore, 57% of the injected mercury is not producible. This shows that 43% (= 100% – 57%) of the initial nonwetting phase is recoverable.

We implement the same procedure for all samples in each pore structure shown in Figure 4.1 to evaluate recovery and average the values for each pore structure. The results are listed in Table 4.1 in the rows showing "Hg withdrawal" test. These recoveries can be regarded as the maximum feasible ultimate recovery. The underlying assumptions are that (i) the initial gas saturation in the field is no greater than the drainage endpoint saturation of mercury and (ii) that the only factor affecting recovery is the residual gas saturation in the matrix. Smaller recoveries could occur in practice for technical as well as economic reasons, and these other factors could mitigate the predicted difference in recovery from each pore type.

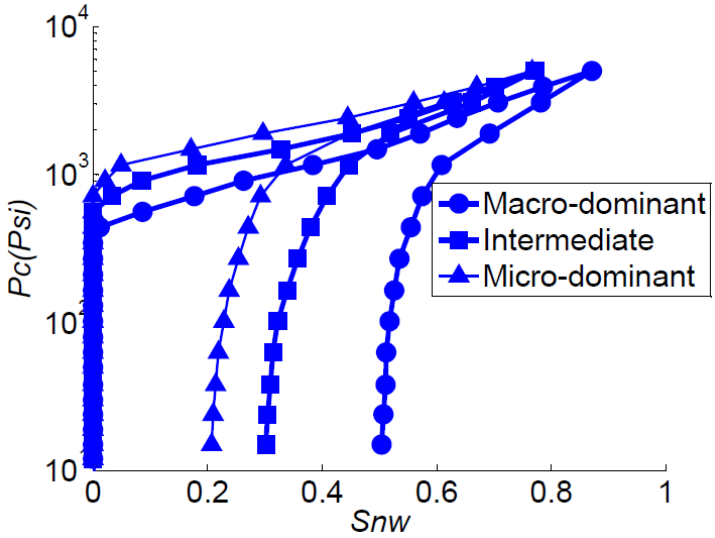

Figure 4.2: Examples of mercury intrusion/withdrawal data for Western tight gas sandstone samples that correspond to different pore structures. In each pore structure, the capillary pressure is larger during intrusion for a given non-wetting phase saturation. The macro-dominant pore structure yields the largest residual mercury saturation as it has the largest fraction of connected intergranular void space. The gas permeabilities of macro-dominant, intermediate, and micro-dominant samples are equal to 11.6, 4.8, and 2.3 microdarcy, respectively. The ratio of the residual mercury saturation at the end of withdrawal to the saturation at the start of withdrawal indicates the fraction not recoverable, and the complementary part is recoverable. The recoverable fraction is thus equal to $1-\frac{S_{nwr}}{S_{nwi}}$.

The capillary pressure was increased to a maximum of 5 kpsi in the tests shown in Figure 4.2. This is sufficient to establish similar endpoint saturations of mercury (0.8 to 0.85) in most of the samples. Hence, the differences in recoverability are due to the pore type.

Table 4.1: Estimated ultimate recovery (EUR) for different pore structures with large initial gas saturations. The recoverable fraction is approximated by computing the ratio of residual mercury saturation at the end of withdrawal (imbibition), S_{nwr}, to initial mercury saturation at the end of intrusion (drainage), S_{nwi}. The recoverable percent is the fraction of initial gas saturation that is producible if S_{gi} were equal to S_{nwi}.

Pore structure	S_{gi} (%)	S_{gr} (%)	Recoverable %
Macro-dominant	85	47	45
Intermediate	83	33	60
Micro-dominant	81	14	83

Table 4.1 presents the recovery in terms of the fraction of initial gas saturation recoverable and not the producible gas saturation itself. For instance, in macro-dominant pore structure, 45% of the initial gas saturation which is 85% is producible. So the recoverable gas saturation is 38%. Crucially, the laboratory measurements of mercury withdrawal indicate that the producible fraction of stored gas is different for different pore structures. The micro-dominant pore structure has the largest recovery (= 83%) of large initial nonwetting phase saturations.

4.2.2. Estimating ultimate recovery from cyclic mercury intrusion and withdrawal

In this section, we generalize the preceding section's approach to partial cyclic intrusion/withdrawal. This enables an estimate of recoverable fraction from smaller initial gas saturations in each pore type. We suppose that the fraction of mercury saturation recovered in each cycle provides an estimate of the fraction of gas can be recovered from the pore type involved in that cycle. For this purpose, we use cyclic mercury intrusion/withdrawal data reported by Cluff and Webb (2009). The analysis of these data is restricted to the core samples whose gas permeabilities are less than 10 microD. This is a legitimate range of permeability for non-fractured tight gas sandstones considering our laboratory measurements as indicated in Figure 4.1. In the cyclic drainage/imbibition, the capillary pressure is increased up to different values at the drainage endpoint of each cycle. A schematic of cyclic intrusion/withdrawal is shown in Figure 4.3(following Cluff and Webb, 2009). For this k = 5 microD sample, the capillary pressure was increased up to 0.75, 2, and 10 kPsia at the drainage endpoint of the three measured cycles. These capillary pressures are sufficient for the invasion of throats with characteristic sizes of 0.30, 0.11, and 0.02 micrometers. The measured cycles are indicated with red arrows in panels (a), (c) and (e) of Figure 4.3. Two other cycles are indicated in panels (b) and (d). The basis for using these cycles is that had a measurement of the indicated cycle been made, the residual saturation would have been the same as the value observed in the actual cycle. This is reasonable considering the drainage curve in each cycle continues smoothly from the drainage curve of the preceding cycle.

We classified the pore structures by analyzing their drainage results obtained from porous plate. Therefore, the recoverability of each pore structure can be assessed for different initial gas saturations if we consider the drainage/imbibition cycles of the corresponding throats in mercury intrusion/withdrawal test. Hence, we use the first and

combination of first and second cycles to analyze the recoverability of macro-dominant pore family ((a) and (b) in Figure 4.3). For the intermediate pore structure, we employ second cycle and combination of second and third cycles ((c) and (d) in Figure 4.3), and for the micro-dominant pore structure, in which the void space is primarily microporosity, we adopt the last cycle ((e) in Figure 4.3). Noting that the drainage portion rejoins the previous drainage curve, we assume the nonwetting phase configuration at the end of any portion of the drainage is unaffected by preceding imbibition loops.

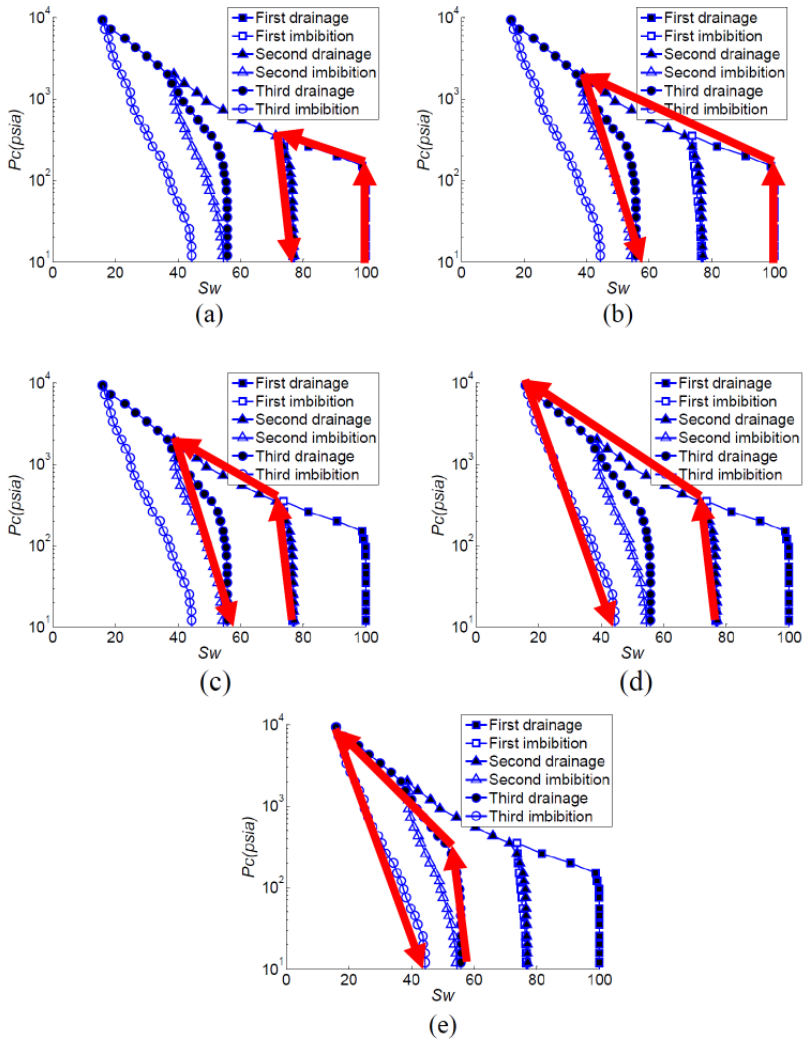

Figure 4.3: An example of cyclic mercury intrusion and withdrawal (Cluff and Webb, 2009) from which we estimate the ultimate recovery of different gas

saturations in different pore types in tight gas sandstones. The mercury withdrawal tests were continued up to zero capillary pressure and not negative values. Individual cycles indicated as sequence of red arrows. The first (a) and combination of first and second cycles (b) are to estimate the recovery for macro-dominant pore structure. Second cycle (c) and combination of second and third cycles (d) re used for intermediate pore structure. The last cycle (e) is for the micro-dominant pore structure.

For the sake of clarity, we elaborate the procedure for the macro-dominant pore structure ((a) in Figure 4.3). The wetting phase saturations, $S_w = 1 - S_{Hg}$, at the end of first drainage and imbibition cycle are 74% and 78%, respectively in Figure 4.3(a). This means that the nonwetting phase saturations for these conditions are 26% and 22%, respectively. Therefore, the produced nonwetting phase saturation is 4%, and consequently the recovery is 15% ($= \frac{4\%}{26\%}$) of the initial saturation (26%) established during drainage. This estimation implements only the first cycle and is appropriate for low nonwetting phase saturations of macro-dominant pore structure.

For larger nonwetting saturations in macro-dominant pore structure, we use the combination of first and second cycles ((b) in Figure 4.3). The wetting phase saturations at the end of second drainage and imbibition cycle are 39% and 54%, respectively. So the nonwetting phase saturations at the end of drainage and imbibition are 61% and 46%, respectively. Hence, the recovered nonwetting phase saturation is 15%. This implies that 29% ($= \frac{15\%}{61\%}$) of the nonwetting phase is producible if the initial nonwetting phase saturation is 61%.

After implementing the above approach for 9 samples, we average (arithmetic mean) the initial nonwetting phase saturations and their recoverable fractions for each pore structure to determine the ultimate recovery. The results are listed in Table 4.2. We

observe that the recovery% improves as the fraction of microporosity increases and that the micro-dominant pore structure has the largest recovery%. This is because of increase in the fraction of tree-like microporosity.

Table 4.2: The recoverable fraction is determined from partial cyclic mercury intrusion/withdrawal data (Cluff and Webb, 2009). This is a generalization of the intrusion/withdrawal approach implemented in the preceding section. The fraction of recovered mercury in different cycles, unlike the previous approach which was for a single withdrawal from drainage endpoint, is adopted to approximate the producible fraction of gas.

Pore structure	S_{gi} (%)	S_{gr} (%)	Recoverable (%)
Macro-dominant	30	26	14
Macro-dominant	59	44	25
Intermediate	34	19	44
Intermediate	58	31	46
Micro-dominant	40	13	68

Comparing the recoverable fractions (Tables 4.1-2) of each pore structure at different initial saturations, we realize that the recovery also improves as the initial nonwetting phase saturation increases for each pore structure. This is familiar from "initial-residual" curves in conventional rocks. The behavior of tight gas sandstones in this regard is amplified by the influence of microporosity. A larger nonwetting phase saturation is attained at a larger capillary pressure which leads to more invasion of narrower throats that are in tree-like pore microporosity. We also know that the tree-like pore structure has a better producibility. Thus, we interpret that the better recoverability

of pore structure at larger saturation is because of more invasion of tree-like microporosity.

It is of interest to know how much of the gas in place is producible and for that reason, we present the producible gas saturation ($S_{g,p}$) versus initial gas saturation (S_{gi}) for different pore structures (Figure 4.4). We use the predicted ultimate recoveries addressed in Tables 4.1-2. The producible gas saturation is determined by multiplying the initial gas saturation (S_{gi}) and the recoverable fraction. For instance, when the initial gas saturation of macro-dominant pore structure is 30%, the recovery fraction is 14% (first row of Table 4.2) and hence, the producible gas saturation is 4% (= 14% × 30%). This plot indicates an estimate for the gas recovery from the reservoir if one type of pore structure constitutes the void space. This plots also provides an upper and lower limits of producible gas saturation (upper limit is for micro-dominant and lower limit is for macro-dominant), as we know that the void space in a reservoir is a mixture of macro- and micro-porosity. Figure 4.4 implies that a gas saturation profile that is uniform with depth at the beginning of production will evolve to a highly variable profile if the pore types are distributed non-uniformly with depth. Large residual saturations will remain in zones dominated by macroporosity, while production will continue from zones dominated by microporosity until much smaller residual saturations are established.

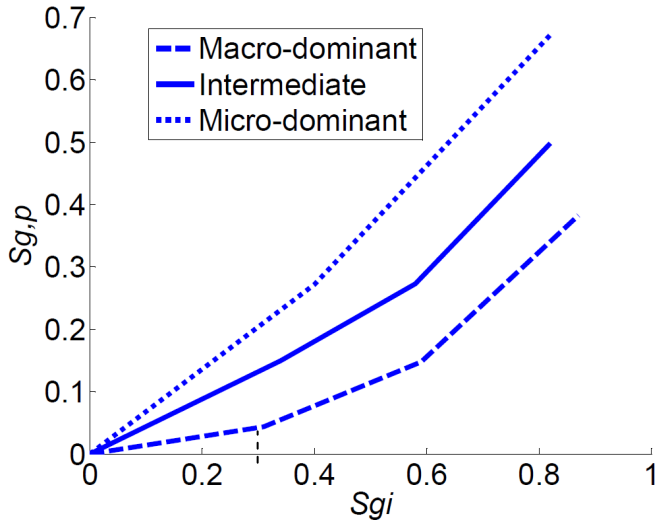

Figure 4.4: The producible gas saturation ($S_{g,p}$) versus initial gas saturation (S_{gi}) for different pore structure that is based on recoveries listed in Tables 4.1-2. This provides an estimate for the EUR from a tight gas reservoir if the one type of pore structure constitutes all the void space in the reservoir. Consequently, it provides lower and upper limits of gas production if the void space is a mixture pore types. Previously, Lake (2010) indicated the effect of having different rock types on the producible gas saturation; however, we address the effect of having different porosities in tight gas sandstone here for the first time.

4.3. Conclusions

We estimated the ultimate recovery (EUR) of tight gas sandstone using mercury intrusion/withdrawal data. The ultimate recovery is predicted to be between 14% to 83% of the initial hydrocarbon saturation depending on the ratio of microporosity to total porosity and initial gas saturation. This is an estimate for the recovery from the matrix of tight gas reservoir. The recovery increases as the fraction of tree-like microporosity increases and also improves with an increase in initial hydrocarbon saturation.

It is of interest to determine whether the predicted trend is consistent with the actual production data. Hence, we will analyze the correlation between the pore structure and the producibility in the subsequent chapter. The pore structure will be determined

from the laboratory measurements wherever it is available or production rates. The production data are from the production logging tool (PLT).

Chapter 5: Production data of tight gas sandstone and its correlation with pore types

5.1. Introduction

We now seek to validate the multiscale model developed. While direct measurements of gas production from core samples of each rock type are not available, field production data (a repeated PLT) and logs of the producing interval are available. The validation test is thus qualitative: are the data inconsistent with expectations based on the abundance of microporosity? Inconsistency would lead us to reject the hypothesis that microporosity correlates with greater producibility; consistency provides some support for the hypothesis, but there are not yet sufficient data to quantify the influence of other factors on the production data.

The essence of the test is that the larger recoverable fraction expected from microporosity-dominated intervals should result in a slower decline in the production rate from that interval. This predicted effect must be deconvolved from another first order effect: the initial production rate of micro-dominant pore structure is smaller compared to other pore structures because of its typically smaller permeability. The decline in production rate would thus be slower in absolute terms (i.e. time on production), even if the recoverable fraction were the same. Table 5.1 lists our expectations of recovery, decline rate, and initial production rate for each pore structure type.

Table 5.1: The multiscale model predicts the pore structures behave differently in terms of initial production rate, decline rate, and the recovery.

Pore structure	Recovery fraction	Decline rate	Initial rate
Macro-dominant	Small	Fast	Large
Intermediate	Small to moderate	Moderate	Moderate
Micro-dominant	Large	Slow	Small

The porosity type is not the only factor affecting the producibility. In practice, many other parameters are involved that eventually control the ultimate recovery. For instance, we could enhance the producibility by fracturing and re-fracturing the formation. The effects those parameters are not studied here and here we only focus on the influence of pore type on ultimate recovery, in effect assuming that all other factors are the same from one well to the next.

First, we investigate the gas production data of a well obtained from production logging tool (PLT) analysis along with the residual mercury saturation (S_{nwr}) for core plugs from a portion of the logged interval. The objective is to determine whether the decline in the production rate decreases with an increase in the fraction of microporosity of the void space, which is inferred from the residual mercury saturation. Because little mercury data are available, we also conduct a secondary test: we indicate where the pore structure is slightly micro-dominant or macro-dominant according to absolute gas permeability and then study the relation of decline in the production rates to the fraction of microporosity. This test is less rigorous because although large permeability is associated with macroporosity-dominated rocks, small permeabilities are observed in all three rock types, Figure 4.1. Finally, we explore the production data over a larger interval of the well to see how the estimated ultimate recovery (EUR) is related to initial production rate (IP) in tight gas sandstone.

5.2. Correlation of decline ratio with residual nonwetting phase saturation

Here, we indicate whether the fraction of microporosity increases in the producing interval by taking into account the residual mercury saturation (S_{nwr}) at the end of a mercury intrusion/withdrawal measurement as indicated in the preceding chapter. Smaller

residual nonwetting phase saturation corresponds to larger fraction of microporosity in the void space.

We use the gas production rate profile in a well completed in a long interval of a Western US tight gas sandstone determined by PLT analysis. Figure 5.1 shows the normalized production data at relative depths in the well at two different times three months apart. The normalized rates are determined from normalizing the gas entry rates obtained form PLTs to a reference value so that the normalized rates remain smaller than or equal to unity. The relative depth indicates the depth from a baseline in the well. We observe variability both in the initial production rates and in their declines. All the layers with large gas rates declined during the three months between PLT. Some of the layers with smaller rate declined little or not at all.

We use the gas production rate profile in a well completed in a long interval of a Western US tight gas sandstone determined by PLT analysis. Figure 5.1 shows the production data at different depths at two different times three months apart. Neither the production rates versus depth nor their decreases are uniform. All the layers with large gas rates declined during the three months between PLT. Some of the layers with smaller rate declined little or not at all.

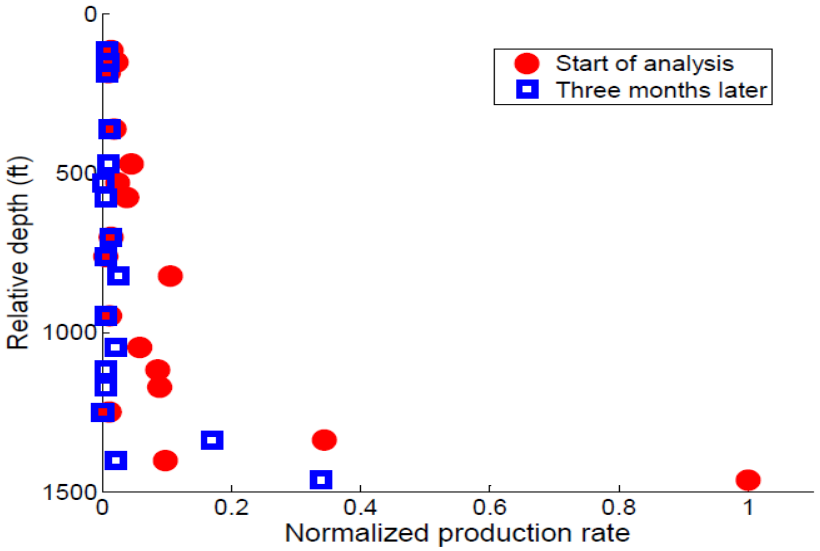

Figure 5.1: Normalized gas production rates of a Western tight gas reservoir logged versus relative depth. The relative depth is measured from a baseline in the well. The actual rates are obtained from two production logging tool (PLT) analyses taken three months apart.

To normalize the differences between the two PLTs, we define a decline ratio (R_i) as follows:

$$R_i = \frac{q_{gsc,m}(t = t_1) - q_{gsc,m}(t = t_1 + 3Mo)}{q_{gsc,m}(t = t_1)} \tag{5.1}$$

where $q_{gsc,m}(t)$ is the gas production rate of layer m of the reservoir at time t. All the production rates studied here are from a layer of reservoir and not the entire well and hence, we drop the subscript m hereafter. The decline ratio determines the ratio of decline in the production and not the decline in the production itself. It allows us to see whether the decline in the production is significant compared to the start-of-analysis rate. A smaller decline ratio means that the rate is less lowered by production.

Now, we explore the correlation of residual nonwetting phase saturation (S_{nwr}) and the decline ratio (R_i) in the production. S_{nwr} is the mercury saturation obtained from

withdrawal test (see section 4.1). The fraction of the microporosity to total porosity of each interval is decided from S_{nwr}, in which the low values correspond to slightly micro-dominant pore structure and high values to slightly macro-dominant. Core data are available only from a subset of the logged interval in Figure 5.1.

We have limited core measurements over the producing interval to decide the pore structure of the layer for which we have two PLTs. More importantly, the core measurements show heterogeneity at their scale which is below the PLT scale. Thus, we assign the pore structure of the producing interval based on trend of change in the core measurements. The pore structures of the producing intervals are taken to be slightly micro-dominant, intermediate, and slightly macro-dominant whereas the closest core measurements could be micro-dominant, intermediate or macro-dominant. For instance, at the relative depth of 145 ft the core sample is macro-dominant and we consider the producing interval as slightly macro-dominant from the trend of change in the core measurements (see Figure 5.2(a)). This is because we infer the pore structure of the interval from core measurements which is representative of a smaller scale than the PLT scale. We use the same approach in determining the pore structure from permeability measurements in the subsequent section (see Figure 5.3).

The comparison of the variation of decline ratio (R_i) and residual mercury saturation (S_{nwr}) indicates some correlation, Figure 5.2. Both increase with relative depth from 115 ft to 155 ft and decrease from 155 ft to 185 ft. There is a moderate decline ratio of 0.42 at 115 ft and large decline ratio of 0.6 at 155 ft, both of which are consistent with our model prediction for intermediate and slightly macro-dominant pore structures, respectively. However, the decline is small at 185 ft which is not what our model predicts if we assign the pore structure based on the closest core measurement available at the relative depth of 175 ft.

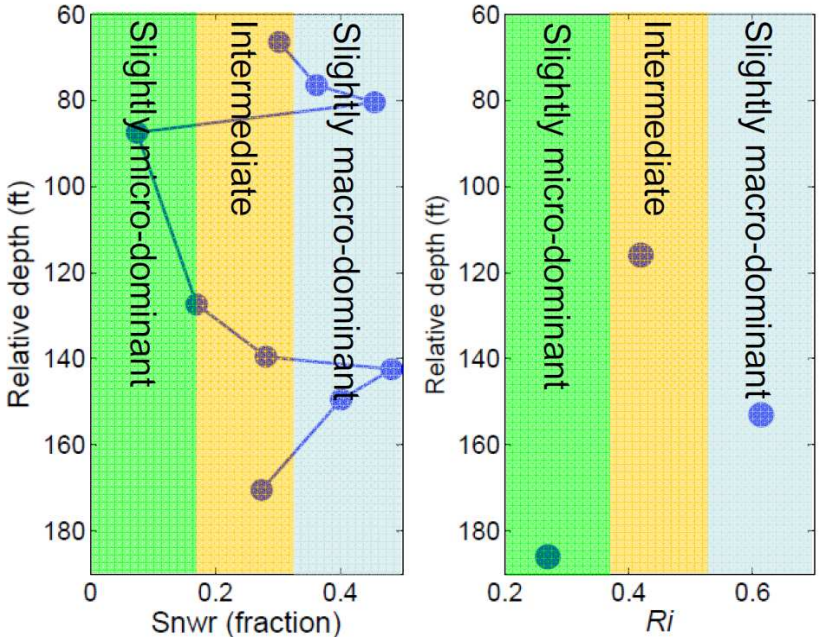

Figure 5.2: There is a correlation between the fraction of microporosity in the void space predicted from (a) residual nonwetting saturation (S_{nwr}) and (b) decline ratio (R_i). The residual nonwetting phase saturation is obtained from mercury withdrawal (section 4.1) and the decline ratio is evaluated by comparing the gas production rates with three months difference using Equation (5.1). The comparison of the decline ratio and residual nonwetting phase saturation is limited to the intervals for which the core data are available and not for the entire well shown in Figure 5.1. The relative depth here is defined similar to Figure 5.1 and thus, we explore the top interval of the well shown in Figure 5.1.

5.3. Correlation of decline ratio with absolute gas permeability

In this section, we estimate the pore structures from absolute gas permeability and consequently, the correlation of pore structures with decline ratio (R_i). In average, the

slightly macro-dominant pore structure has the low, intermediate pore structure the average, and slightly macro-dominant pore structure the high permeabilities.

The decline ratios of the production rate along with the pore structures determined from absolute permeability are presented in Figure 5.3. The gas production rates indicate moderate decline ratio at the relative of depth 115, large decline ratio at 155, and small decline ratio at 185. This trend is in agreement with the pore structures, where we expect the slightly micro-dominant exhibit the low decline ratio, intermediate the average, and the slightly macro-dominant the highest decline ratio. Therefore, the well production rates are strongly correlated with the pore structures obtained from absolute permeability and hence, the notion of lower decline rate, listed in Table 5.1, is supported by the actual production data.

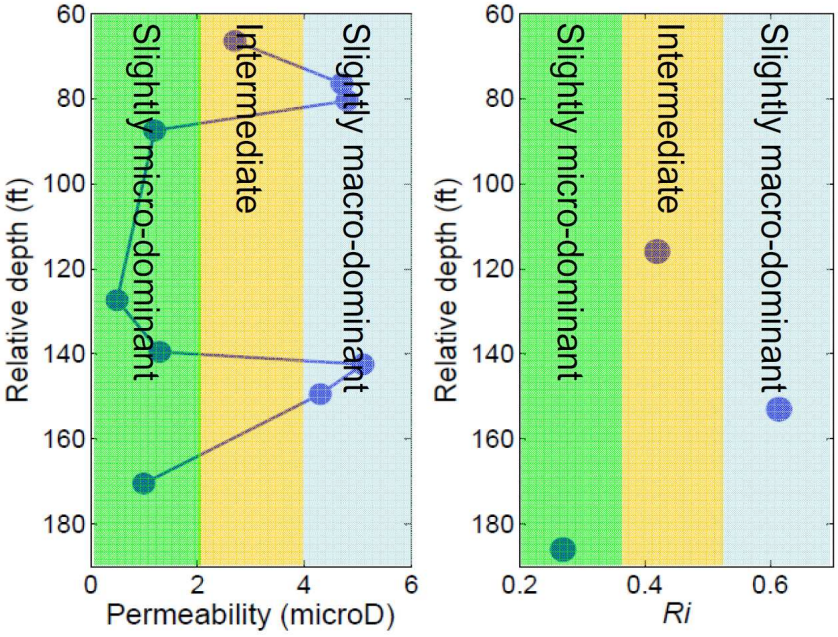

Figure 5.3: Variations of the (a) absolute gas permeability and (b) decline ratio (R_i) with relative depth for the same tight gas reservoir as Figure 5.2. The comparison of the decline ratio and permeability is only for an interval whose core data are available and not for the entire well. The fraction of microporosity to total porosity, which is indicated by slightly micro-dominant, intermediate,

and slightly macro-dominant, is assigned based on permeabilities, cf. Fig. 16. We observe a strong correlation between pore structure assigned from permeability and decline ratio. There are moderate decline at the relative depth of 115 ft, large decline at 155 ft, and small decline at 185 ft in both permeability and decline ratio. The relative depth here is defined similar to Figure 5.1 and thus, we explore the top interval of the well shown in Figure 5.1.

It might be argued that the lower decline ratio of the formation in the slightly micro-dominant interval is primarily because of smaller permeability and not larger recovery. To analyze this, we explore the cumulative production of a gas reservoir per unit thickness of the producing interval. For this purpose, we use the tank model (Walsh and Lake, 2003) to represent individual layers in this well; thus, we assume negligible vertical communication. The production rate of a gas reservoir is calculated as:

$$q_{gsc} = \frac{q_{gsci}}{\left[1 + \frac{q_{gsci} z p_{sc} t}{V_p (1 - \overline{S_{wi}}) p_i}\right]^2} \tag{5.2}$$

where q_{gsci} is the initial gas production, q_{gsc} gas production rate at time t, z compressibility factor of the gas, V_p reservoir pore volume, $\overline{S_{wi}}$ the average initial water saturation, and p_i reservoir initial pressure. Since we want to implement the effect of pore type on residual gas saturation, the $(1-\overline{S_{wi}})$ term should be replaced by $(1-\overline{S_{wi}}-S_{gr})$. Thus, we consider $V_p(1-\overline{S_{wi}}-S_{gr})$ as a recoverable pore volume. Other parameters are not of interest here as we want to distinguish the influences of permeability and producible pore volume on the decline ratio. As a result, we use the following equation after assuming other parameters being constant:

$$q_{gsc} = \frac{q_{gsci}}{(1+\beta t)^2} \tag{5.3}$$

where q_{gsci} is proportional to permeability, and consequently β is proportional to permeability and inversely proportional to recoverable pore volume.

We suppose that the reservoir consists of three layers, based on the prior analyses in Figures 5.2-3, with equal initial gas saturation and with no cross flow (Figure 5.4). If two values of production rates (q_{gsc}) from each layer are measured at different times, then the coefficients q_{gsci} and β can be determined for each layer. The actual gas entry rates of the well for which the normalized rates are shown in Figure 5.4 are measured by PLTs after 124 and 225 days of production. Using the actual rates, we determine the corresponding values of q_{gsci} and β for each layer. The pore structure of each producing layer was assigned from the core laboratory measurements that we analyzed earlier (Figures. 5.2-3).

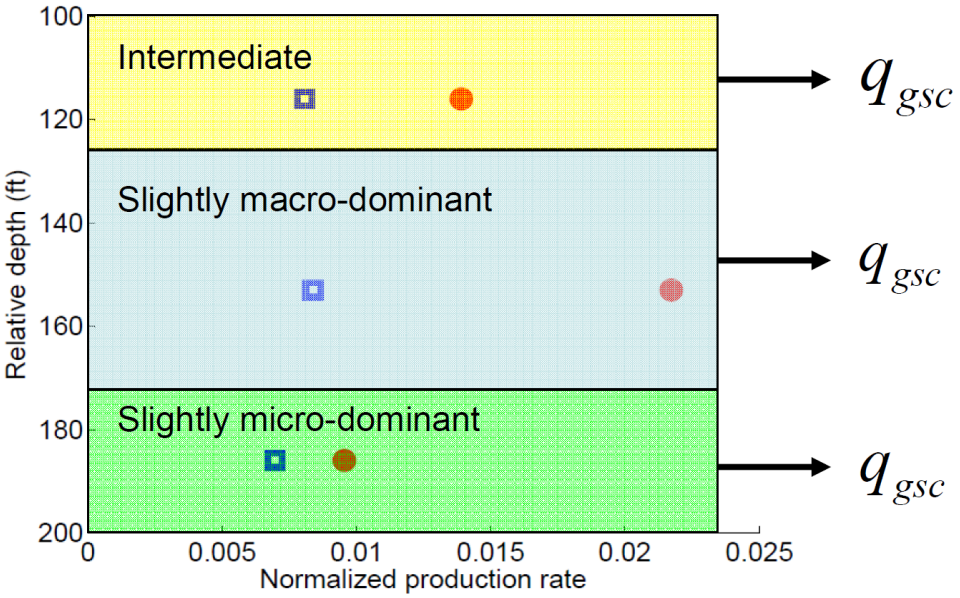

Figure 5.4: Two normalized production rates (first rate is red circle and second is blue square) of the layers of tight gas reservoirs obtained from production logging tool (PLT) after 124 and 225 days from start of production. The relative depth and normalized rate are defined similar to Figure 5.1. We suppose that there is no cross flow between layers and thus, we predict the cumulative gas production behavior of each layer using Equation (5.3). The

determination of pore structure is based on analysis of core laboratory measurements (cf, Figures. 5.2-3).

Now, for the sake of comparison between the producibilities of the reservoir layers with different pore structures, we turn to the analysis of cumulative production by the use q_{gsci} and β of the three layers. We integrate Equation (5.3) over time and to get rid of the effect of thickness, we compare the results per unit thickness of each layer. The thickness of each layer is determined from the log.

Figure 5.5 plots the normalized cumulative gas production per unit thickness of each layer. The cumulative productions are normalized to a reference value so that they remain smaller than or equal to unity. The cumulative production of the slightly macro-dominant interval is the largest at early life of production which is because of its superior permeability and at a later time, it becomes the smallest resulting from an inferior producibility. The difference in the cumulative production is because of residual gas saturation; the slightly micro-dominant interval has the best producibility and macro-dominant the worst, see Table 5.1.

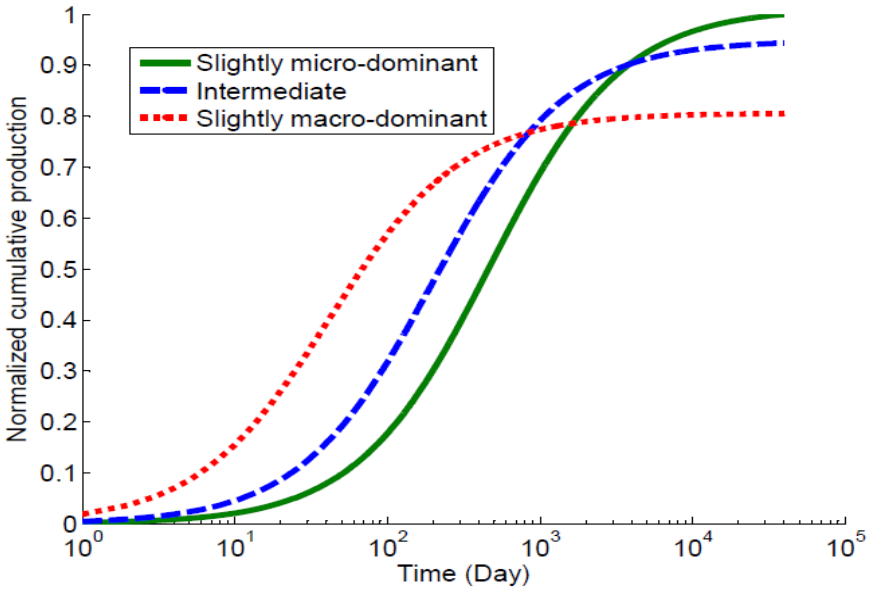

Figure 5.5: Normalized cumulative gas productions of the three layers of the tight gas reservoir shown in Figure 5.4. The early cumulative production of the slightly macro-dominant interval is the largest because of its permeability. Then, it becomes smaller than other layers at a later time resulting from an inferior producibility. The slightly micro-dominant interval has the best recovery despite its low initial production (IP). The normalization used here only scales the results linearly.

Figure 5.5 is a quantitative illustration of the behavior described in Table 5.1. Different pore types in tight gas sandstones can overprint the usual correlation between large initial production (IP) and large EUR. Each category yields a different producibility at a different pace, and as a result, the ultimate recovery of the tight gas varies depending on the distribution of the pore types. In other words, IP alone will not predict EUR unless only one pore type is present.

5.4. Estimated ultimate recovery (EUR) for the producing interval and the well using tank model

The core measurements data are not available over the entire depth of the well, as it is often the case in practice. This prevents us from assigning the pore structure over the

entire well. Therefore, we examine the correlations of the tank model parameters with the estimated ultimate recovery (EUR). First, we explore the dependency of EUR on initial production (IP) as it is often used in conventional reservoirs. Then, we use β of the tank model in a scaled form to explore its performance in screening the EUR.

We present the results in the normalized form and not the actual value. This allows the use of what we learn from this research for other tight gas formations if the thickness of producing interval and initial pressure are not similar to the well investigated here. This, of course, depends on the presence of two-scale porosities interacting with each other similar to here.

Initial production (IP) is often adopted for EUR in conventional reservoirs. We test this approach here with the use of tank model; we determine q_{gsci} and β for all the producing intervals. The production rates which we use for tank model are from the PLTs whose normalized values are shown in Figure 5.1.

The tank model is derived on the basis of constant pore volume (see Eq. 5) and this means no cross-flow between the layers if we use the model for a specific interval with known producing thickness. However, there are shifts in the production rates of some layers which is presumably because of flow from adjacent intervals. An increase in the production rate from a given layer yields a negative β (see Equations (5.2) and (5.3)) if the tank model is used. Hence, we do not analyze a reservoir layer whose β is negative. We also suppose that the tank model can capture the entire well and thus, predict the gas production based on that. The coefficients of tank model for the entire well are found to be positive.

Figure 5.6 shows variation of the normalized predicted cumulative gas production per unit thickness, which can be considered normalized EUR per unit thickness, with normalized IP which is for unit thickness of the interval. To predict the cumulative gas

production, we integrate Equation (5.3) over time for a unit thickness. We observe that EUR (predicted from pore type and repeat PLTs) does not correlate with IP. This observation agrees with our analysis of core measurements earlier in which we showed that EUR has to be estimated from two-phase displacement and not from permeability, especially for tight gas sandstones. Our pore structure analysis reveals that there is a significant scatter in the recovery despite having almost similar permeability (Figure 4.1). Therefore, the lack of dependency of EUR on IP is because of the pore structure. Regarding the position of the "entire well" datum, we should note that it depends strongly on the overall fraction of microporosity. This means that the entire well could have a small IP and still have large EUR, larger even than the one shown.

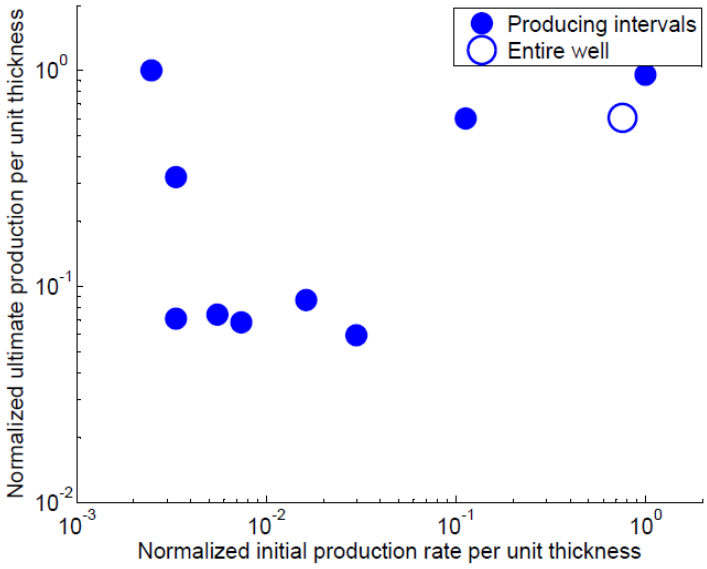

Figure 5.6: The normalized ultimate gas production predicted from Equation (5.3) is not a function of normalized initial production (IP). This means that unlike conventional reservoirs, initial production rate alone does not control the ultimate recovery in tight gas reservoirs. The ultimate gas production and initial production (IP) are normalized after dividing them to the thickness of the producing interval so that the normalized parameters are smaller than or equal to unity. This normalization only scales the plotted results linearly.

The ultimate gas production is calculated with integrating tank model over time. The coefficients of tank model are determined from two PLT logs for which the normalized production rates are shown in Figure (5.1).

Now, we are to use a scaled parameter of the tank model for the analysis of EUR. Equations (5.2) and (5.3) reveal that β is equal to $\frac{q_{gsci} z p_{sc}}{V_p (1-\overline{S_{wi}} - S_{gr}) p_i}$ if we account for the residual gas saturation (S_{gr}). Assuming that the initial gas pressure (p_i) is almost the same in the layers, we deduce that the variation of β is because of recoverable pore volume ($V_p(1-\overline{S_{wi}} - S_{gr})$) and initial production rate (q_{gsci}). Moreover, the pore volume is proportional to the thickness of producing layer. Thus, to compare the ultimate recoveries of the layers, we form a scaled parameter as follows:

$$\beta_s = \frac{h \times \beta}{q_{gsci}} \propto \frac{1}{(1-\overline{S_{wi}} - S_{gr})} \tag{5.3}$$

Our expectation is that the normalized EUR of the producing layer per unit thickness increases with decreasing the scaled parameter (β_s) because of the dependency of β_s on S_{gr}. β_s decreases with decreasing S_{gr} (Equation (5.3)) and we expect intervals with lower β_s to be more micro-dominant. To test this, we plot the variation of the normalized EUR with β_s (Figure 5.7). We observe that an increase in β_s lowers the EUR and this indicates that the proposed parameter can be used to screen the layers according to their EURs. More importantly, intervals with large EUR have low β_s. These layers with low β_s are expected to be micro-dominant based on how we define β_s in Equation (5.3).

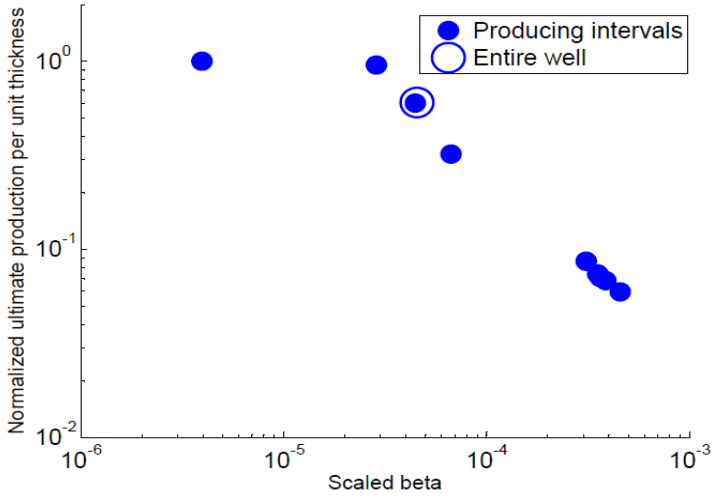

Figure 5.7: The normalized expected ultimate gas production per unit thickness of the layer decreases with an increase in β_s ($=\frac{h\times\beta}{q_{gsci}}$). This indicates that β_s can be employed for EUR instead of initial production (IP) which was used in Figure (5.6). Further, large EUR occurs at low β_s which is expected to correspond to micro-dominant interval based on Equation (5.3). The ultimate production here is normalized here similar to Figure 5.6.

5.5. Conclusions

We have used field data (repeat PLT logs) to test our multiscale model. For this, we classified the pore structure using laboratory measurements like permeability and mercury withdrawal. We observe that the production rate of macro-dominant interval is larger initially but goes below micro-dominant more quickly. The larger initial production rate is because of larger permeability and more loss in the production (larger decline ratio) is a consequence of inferior recovery. This means that the available field data are encouraging and they should be tested as larger sets of data become available.

We extrapolated the production rates of the layers of the tight gas reservoir obtained from PLT and integrated over time to compare the cumulative production. The projected cumulative production per unit thickness indicates that the hydrocarbon

recovery of the micro-dominant interval is the largest, and this agrees with our hypothesis of having better producibility with an increase in the microporosity fraction. Knowing that micro-dominant pore space has the lowest initial production (IP) in the well, we conclude that initial production (IP) alone is not an appropriate tool to probe EUR. This highlights the importance of having a better understanding from pore structure of unconventional rocks which could be true for shale gas reservoirs as well.

We are aware of the importance of the in-depth understanding of the pore structure after investigating the pore structure of the tight gas sandstone in the first part of this dissertation (chapters 3-5). We have been able to predict the hydrocarbon recovery from the study of the pore structure. With that in mind, we will turn to the analysis of the pore structure of the shale gas in the second part of this dissertation. We will take advantage of our understanding from the study of the tight gas sandstones.

Chapter 6: Pore structure of shale

6.1. Introduction

This chapter investigates the pore structure of un-fractured shale to better understand hydrocarbon flow through this type of unconventional resource. We adopt a pore-scale modeling approach which means that we account for the interactions of pores to predict the flow behavior.

Similar to the study of tight gas sandstones in the previous chapters, we begin with investigation of the mercury intrusion (drainage) measurements because it provides valuable insights into not only the pore size distribution but also the topology of the void space. We also check if our understanding of the pore structure is consistent with scanning electron microscope (SEM) images of the shales.

6.2. Mercury intrusion capillary pressure (MICP)

We learned from the study of tight gas sandstones that the capillary pressure measurements are essential to understanding of the pore structure of a void space. Thus, we analyze mercury intrusion results of a shale sample in this chapter.

Figure 6.1 shows mercury intrusion capillary pressure (MICP) results of a Barnett shale sample. The capillary pressure (P_c) here is the mercury pressure during injection and wetting phase saturation (S_w) is determined from the mercury saturation, $S_w = 1 - S_{Hg}$. We observe that no percolation take places; there is no plateau in the P_c-S_w curve. There is not even a slight percolation unlike some tight gas sandstones (see Figure 3.3). This absence of slight percolation has a major implication in terms of the pore structure model. We discuss this subsequently when we propose new pore structure for un-fractured shale.

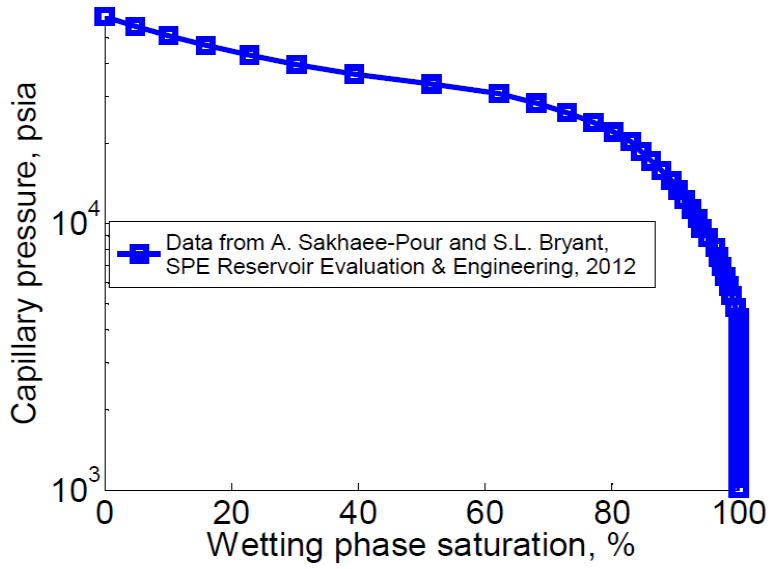

Figure 6.1: Mercury intrusion capillary pressures (MICP) of a Barnett shale sample versus wetting phase saturation (S_w), where $S_w = 1 - S_{Hg}$. The drainage results show that no percolation (invasion of large fraction of pore space after small increase in capillary pressure) takes place (courtesy of Sakhaee-Pour and Bryant, 2012).

6.3. Pore structure models for shale

We propose two pore structure models for the shale. We elaborate the pore throat geometry and connectivity of the pores that are the main features of the each model.

The pore throat is the narrowest part of the void space connecting two neighboring pores. It is crucial to analyze the pore throat geometry because it controls the resistance of flow path between the pores. Thus, we classify the pore throats here and study the implications of each throat on the pore structure characterization. Our pore structure characterization allows us to predict the single-phase permeability of the formation from MICP. We classify the pore throats based on their aspect ratios; the pore throats are either circular (aspect ratio = 1) or slit (large aspect ratio). Examples of such

throat geometries are shown in Figure 6.2. The large-aspect-ratio throats are indicated with blue color.

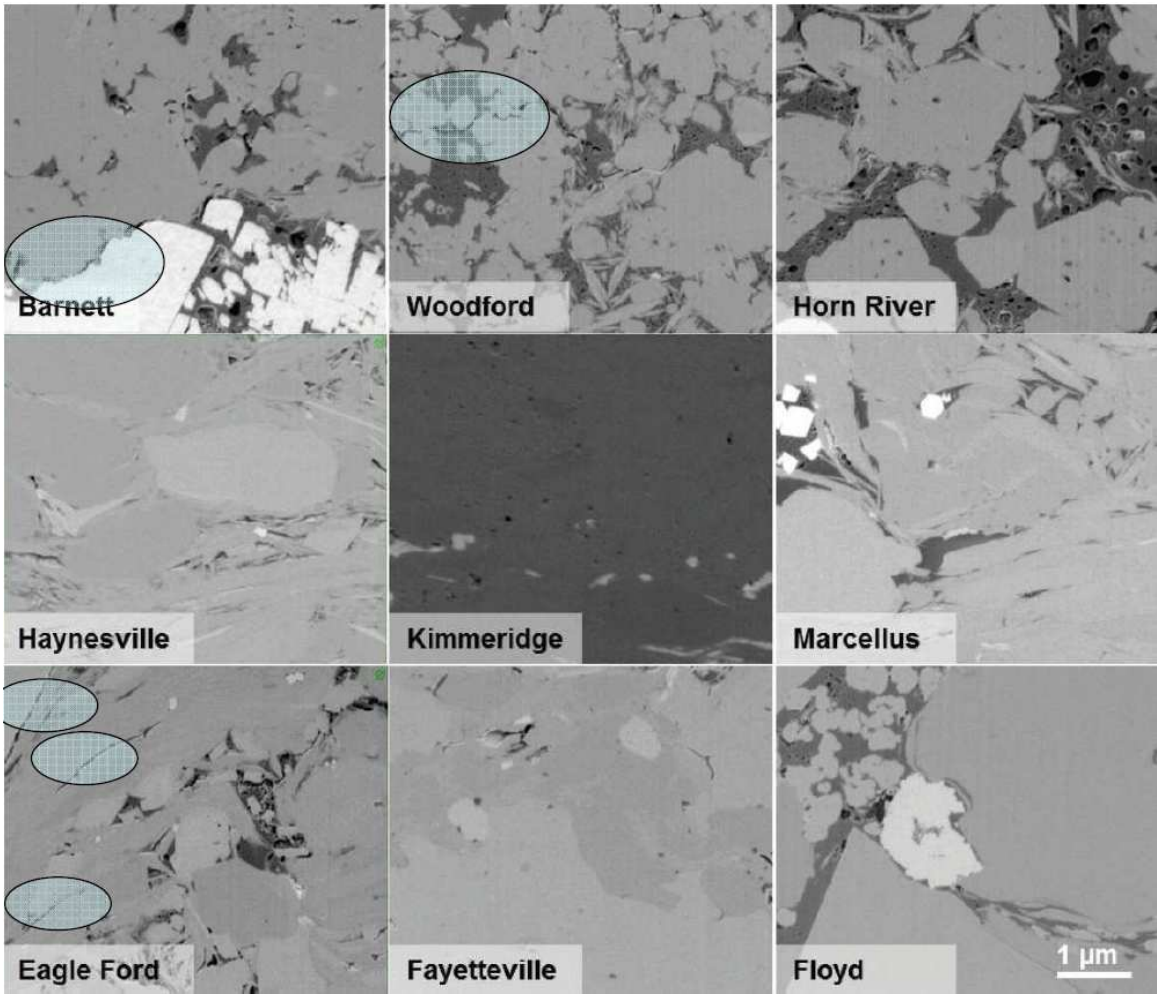

Figure 6.2: Scanning electron microscope (SEM) images of shales (courtesy of Curtis et al., 2010). We classify the pore throats into circular and slit based on their aspect ratios. The microcrack-like throats are indicated with blue color.

Pore connectivity explores interactions of pores from a larger scale than the pore throat. The pore connectivity is concerned with the connectivity of one pore to all its adjacent pores while the pore throat is related to only two adjacent pores. The pore

connectivity is presented in the form of coordination number (z). By investigating the coordination numbers of the pores, we will be able to have an idea about the connectivity of the pores across the sample. This means that we are interested in knowing about not only the pores within one throat distance but also how they form a connected network through the rock. The connected network through the rock is required for the hydrocarbon to flow.

The coordination number (z) of each pore shows the number of pore throats connecting that pore to the adjacent pores. As an example, pores with coordination numbers equal to 2 and 3 are depicted in Figure 6.3.

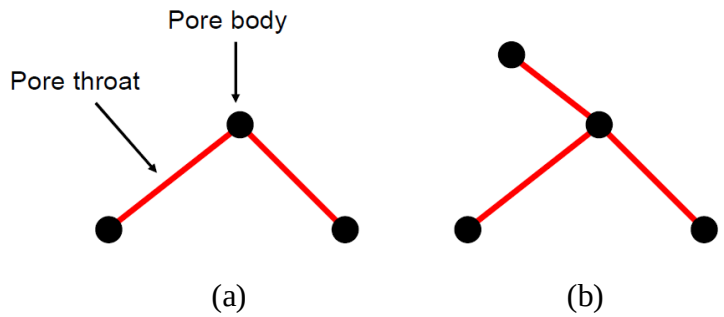

Figure 6.3: Pore structure models for which the coordination numbers (z) of the middle pores are equal to 2 and 3 in (a) and (b), respectively.

To elaborate the effect of coordination number (z) on the connected network of the pores, we review three hypothetical cases here. First, we assume that the coordination number of the pores, except the inlet and outlet, is equal to 2. In this case, the bundle-of-tubes model (Purcell, 1949) is representative of the void space (see Figure 6.4). We elaborated this model in the literature review in chapter 2. The second case is when the coordination number of the pore is equal to 1. This shows that each pore connects to only one neighboring pore which is relevant to the tree-like pore model. We will face this in

many pores of the shale. The last clarifying example is when the coordination number is equal to zero. This indicates that the pore is not connected to any other place and thus, this coordination number denotes isolated pores.

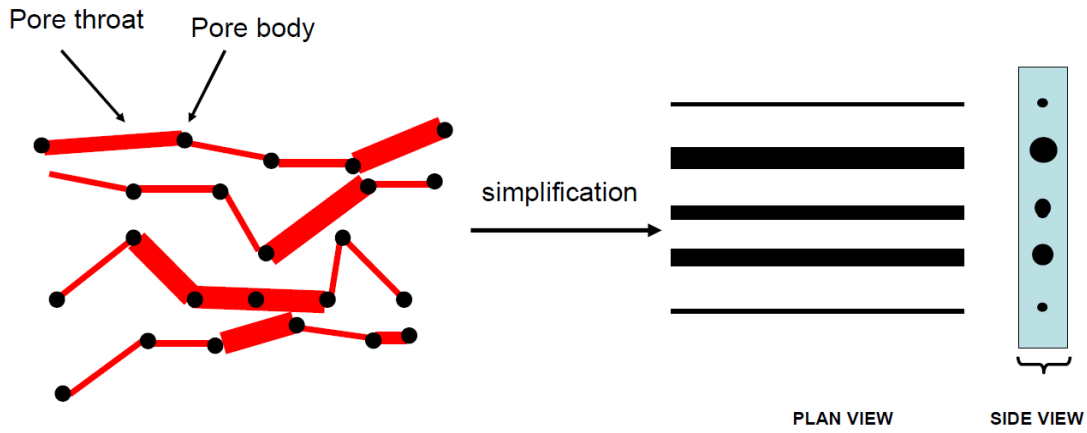

(a) (b)

Figure 6.4: The bundle-of-tubes model (Purcell, 1949) shown in (b) is representative of the void space model shown in (a). This is because the coordination number (z) of the pores is equal to 2 except for the inlet and outlet pores.

6.3.1. Tree-like model

We observe that no percolation takes place during the mercury intrusion capillary pressure measurements (Figure 6.1); more importantly, there is not even a slight percolation unlike tight gas sandstone (Mousavi, 2010). This means that the conventional pore model with high pore connectivity, such as the network defined by a grain packing (Bryant et al., 1993) or any regular lattice, is not representative of the void space.

We learned from the study of tight gas sandstone that the tree-like pore model is capable of capturing non-percolating trend of capillary pressure vs. wetting phase

saturation. Thus, we suppose here that the void space of shale mostly includes the tree-like pores as shown in Figure 6.5.

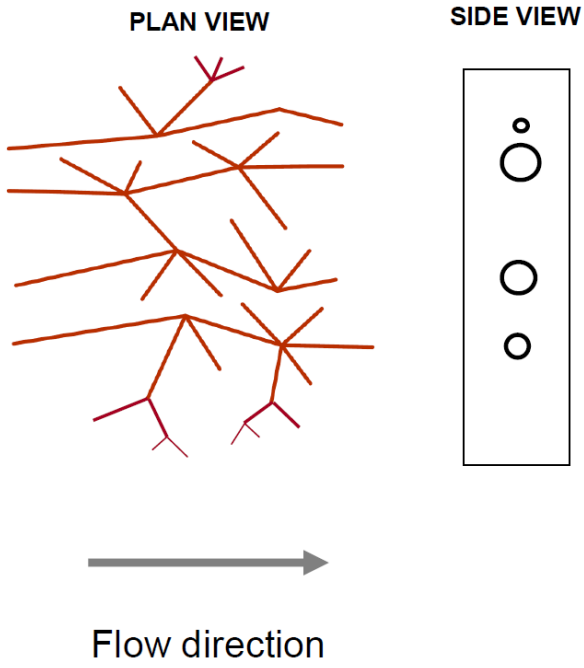

Figure 6.5: The plan and side views of the pore model we propose for the matrix of the shale. No percolation takes place in the mercury intrusion test (Figure 6.1) and thus, we conclude that the void space mainly includes tree-like pores. The tree-like pore model allows us to capture the non-percolating trend of capillary pressure with wetting phase saturation as we learned from the study of tight gas sandstone.

We briefly elaborate the tree-like pore model here for the sake of completeness. This model was thoroughly clarified in the tight gas sandstone part of this dissertation (see chapter 3). In the tree-like pore model, there are multiplying branches with ever smaller throats and volume and this means that the narrower throats are accessible only from the wider throats (Figure 6.6). Further, by definition, there is no cycle in this model. That is, for any two pores, there is one and only one path of throats that connect those

pores. These features prevent percolation from occurring during mercury intrusion. Any increase in the capillary pressure during intrusion will invade the pore throats that are accessible only from the pore throats that are larger from them. Figure 6.6 shows a schematic of the tree-like pore model at three capillary pressures in which mercury is indicated with red color.

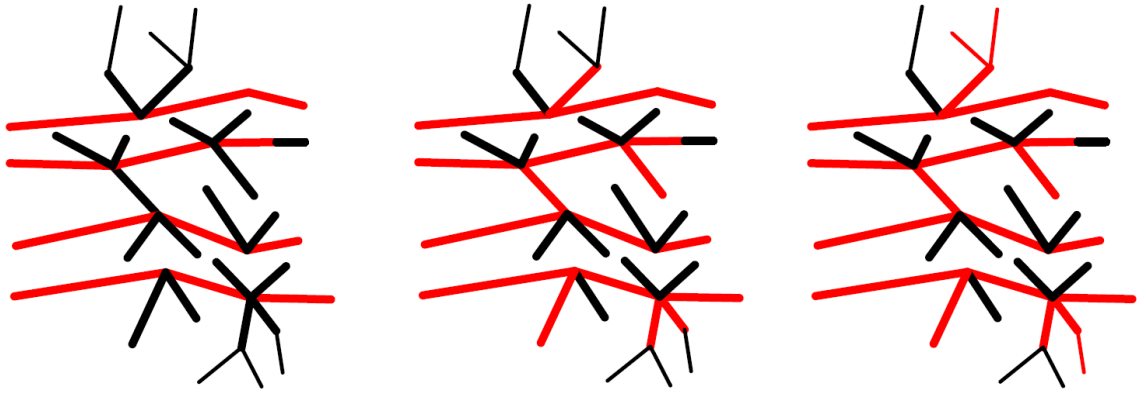

(a) (b) (c)

Figure 6.6: Schematic illustration of the mercury intrusion into tree-like pore model in which line thickness represents the pore throat diameter. The non-percolating increase in the capillary pressure is to invade the narrower throats that are accessible from wider throats (see (a), (b), and (c)). Mercury is shown with red color.

We also assume that each pore throat is circular in cross section in tree-like pore model. This is for computational convenience, though we note that the nanopores observed in kerogen within gas shales commonly exhibit a circular section (Ambrose et al., 2010).

6.3.2. Nooks and crannies (NC) model

An alternative pore model that yields non-percolating drainage curves during MICP can be built from large-aspect-ratio throats. This leads us to the proposition of

another pore model (see Figure 6.7). This approach assumes that the pore throats are mostly connected through the rock similar to the bundle-of-tubes model (Purcell, 1949) but the pore throat geometry is microcrack-like. We term this model nooks and crannies (NC) because of the existing similarity between the pore throat geometry and nooks and crannies (see plan view in Figure 6.7).

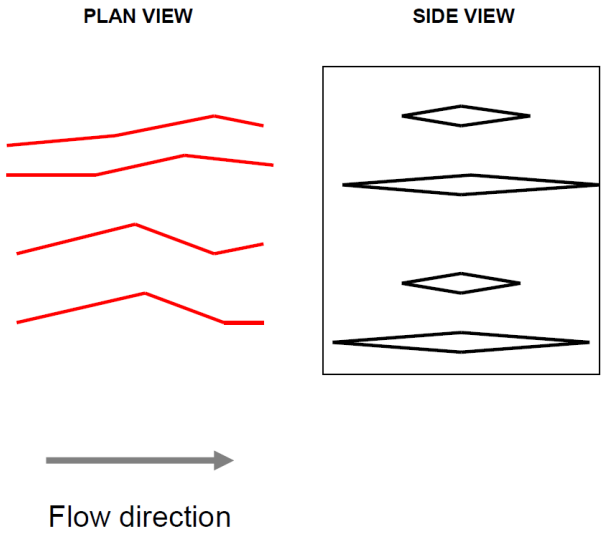

Figure 6.7: Nooks and crannies (NC) model for the matrix of the shale which contains large-aspect-ratio throats. This model is similar to the bundle-of-tubes model (Purcell, 1949) in terms of pore connectivity across the sample as demonstrated in the plan view. However, the pore throat geometry of this model is microcrack-like unlike the bundle-of-tubes model which takes circular tubes as the representative throat geometry.

Figure 6.8 shows how large-aspect-ratio throat behaves during mercury intrusion. The central portion of the throat is widest and hence, the mercury meniscus will enter that part first. Once invaded, as indicated in Figure 6.8(a), subsequent increases in the capillary pressure steadily move the meniscus into the corners of the throat, Figure 6.8(b). This yields an ever increasing, non-percolating capillary pressure curve. This reveals that,

unlike the tree-like pores model, the increase in the capillary pressure is not to invade a previously unoccupied, smaller pore body but to occupy a larger fraction of the void space in an already invaded pore, which is at the corners. These large-aspect-ratio throats must be connected in series to form bundles, and the central portion of each bundle must have nearly constant cross section; otherwise the drainage curve would exhibit percolation.

(a) (b)

Figure 6.8: Mercury intrusion into a large-aspect-ratio throat which is adopted in the nooks and crannies (NC) model. The non-percolating increase in mercury saturation after an increase in the capillary pressure is to occupy the corners. Compare (a) and (b) in which the mercury is shown with red color.

6.3.3. Evidence of the models in SEM images

We take a look at the SEM images of shales to examine the presence of the throat geometries we proposed. We observe both the circular and microcrack-like throats that are shown with dashed and solid lines in Figure 6.9, respectively. This suggests that both models could be adopted. We will, however, evaluate both models further. For this purpose, we will study the effect of confining stress on the features evident in the SEM images, and upon MICP data available in the literature. That analysis suggests that the microcrack-like throats are probably closed under in-situ stress conditions (see 6.6. Image analysis of shale). Thus, the tree-like pore model is representative of in-situ condition.

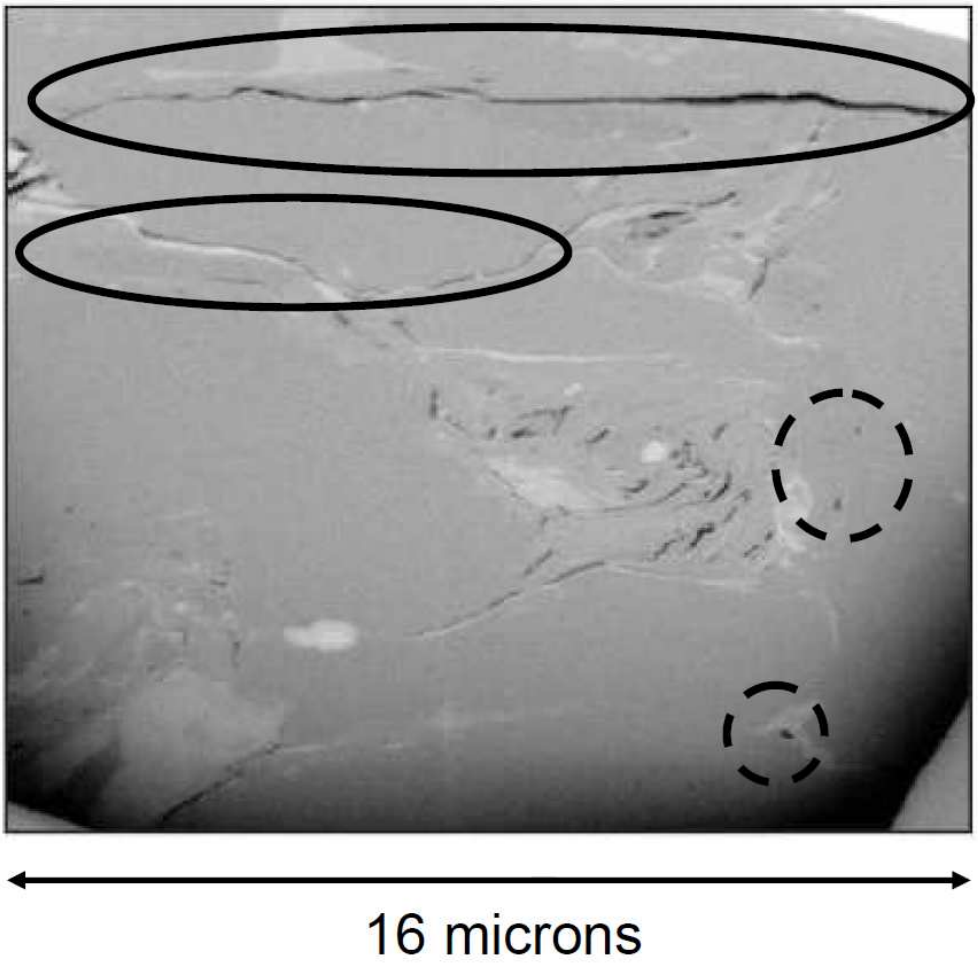

Figure 6.9: Scanning electron microscope (SEM) image of a shale sample shows that both the circular- and microcrack-like throats are present (courtesy of Heath et al., 2011). The circular- and microcrack-like throats are, respectively, indicated by dashed and solid curves.

6.4. Characteristic throat length of the nooks and crannies (NC) model

We are to show the characteristic lengths of the NC throats from MICP data shown in Figure 6.1. We first suppose that the microcrack-like throats are mono-size. This is a limiting case. In reality, pore throats include a distribution of sizes which we will discuss later.

Here, we analyze the NC model with mono-size throats. The main objective is to predict the characteristic length of the throats that allows us to capture MICP data shown in Figure 6.1. We model the large-aspect-ratio throat (Figure 6.10(a)) by a telescopic geometry (Figure 6.10(b)) and predict its corresponding length. Then, we check if the microcrack-like throat with the predicted length is available in the SEM images. If such a throat does not exist, we conclude that the NC model is not representative of the void space.

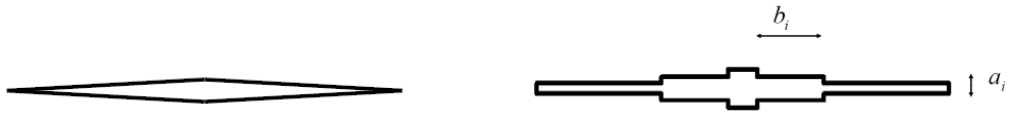

(a) (b)

Figure 6.10: Microcrack-like throat shown in (a) is simplified to a telescopic rectangular geometry (b). We will use the telescopic throat geometry to analyze the flow properties.

Figure 6.10 shows telescopic rectangular throat geometry (series of rectangular sections of increasing aspect ratio transverse to axis of throat) that we take to assess the plausibility of the NC model. The smaller dimension of the i^{th} rectangle is denoted by a_i, and the larger by b_i. To determine the width (a_i) of each rectangle (one of the rectangles forming the telescopic shape) invaded at a given capillary pressure, we use the Young-Laplace equation ($P_c = \frac{2\sigma\cos\theta}{a_i}$). We then determine a lower limit of the length of the rectangle (b_i) by assuming ($b_i = a_i$). We know that the length of each rectangle is not smaller than the width and that is why the assumed length ($b_i = a_i$) provides a lower limit.

We presume that the mono-size pore throats (many telescopic throats similar to Figure 6.10(b)) that are extended through the rock can capture the MICP data. We also presume that the total pore volume is proportional to the total cross section area of the

rectangles because the microcrack-like throats are extended through the rocks. This means that the incremental increase in the wetting phase saturation at each capillary pressure (ΔS_{wi}) is proportional to the total cross section areas of the pore throats invaded at that capillary pressure. Meanwhile, we are aware that the total cross section area of the throats is proportional to the cross section area of one throat because we adopt a mono-size model here. Hence, the incremental increase in the wetting phase saturation is related to the cross section area of one rectangular throat as follows:

$$\Delta S_{wi} \sim a_i b_i \tag{6.1}$$

We first determine the characteristic widths of the pore throats invaded at the entry pressure (a_1) and larger capillary pressures (a_i) using the Young-Laplace equation. We then employ Equation (6.1) to compute the characteristic lengths of the pore throats at larger capillary pressures (b_i) based on the characteristic length of the pore throat at the entry pressure (b_1). Knowing the incremental increase in the wetting phase saturation from MICP data at the entry pressure (ΔS_{w1}) and at larger capillary pressures (ΔS_{wi}), we express the characteristic dimensions of each throat relative to those invaded at entry pressure as follows:

$$\frac{b_i}{b_1} = \frac{a_1 \Delta S_{wi}}{a_i \Delta S_{w1}} \tag{6.2}$$

This relationship expresses the ratio of the throat length at larger capillary pressure (b_i) to the throat length at entry pressure (b_1). This tells us that the determination of b_i also entails b_1 to be known which we take it to be equal to the width of the throat invaded at the entry pressure (a_1). This gives us a lower limit for the length since the throat is rectangular.

Here, we obtain the entire length of the telescopic throat which is to represent the microcrack-like throat (Figure 6.10). The entire length of the telescopic throat is equal to

the summation of the lengths of rectangles. We use the MICP data shown in Figure 6.1 for which the entry pressure is equal to 4836 psi. This says that the characteristic width of the widest throat (a_1) equals to 22 nm. The narrowest parts of the throats were invaded about 60 kpsia, corresponding to a_i = 2 nm.

Using the above approach, we estimate the entire length of the telescopic throat. The capillary pressure (P_c), change in the wetting phase saturation at that pressure (ΔS_{wi}), characteristic height of each rectangle (a_i), and the characteristic length of each rectangle (b_i/a_i) are listed in Table 6.1. We determine the entire length of the telescopic rectangle by calculating the summation of lengths of the rectangles (b_i). The entire length of the telescopic rectangle is found to be 29.5 micrometers.

Table 6.2: Characteristic sizes of the rectangles forming the telescopic pore throat geometry are determined from the MICP data shown in Figure 6.1. P_c refers to capillary pressure during mercury intrusion, ΔS_{wi} change in the wetting phase saturation at the measured capillary pressure, a_i characteristic width of the rectangle, and b_i characteristic length of the rectangle. The entire length of the telescopic throat is found to be equal to 29.5 micrometers which is the summation of the lengths of the rectangles (b_i) listed.

i	P_c (psi)	ΔS_{wi}	a_i (micrometers)	b_i (micrometers)
1	4837	0.005	0.022	0.022
2	5367	0.005	0.020	0.024
3	5832	0.005	0.018	0.027
4	6339	0.005	0.017	0.029
5	6891	0.005	0.016	0.031
6	7490	0.005	0.014	0.034
7	8139	0.005	0.013	0.037
8	8845	0.011	0.012	0.081
9	9614	0.011	0.011	0.088
10	10449	0.005	0.010	0.048
11	11355	0.011	0.009	0.103

Table 6.2

12	12340	0.011	0.009	0.112
13	13408	0.011	0.008	0.122
14	14575	0.011	0.007	0.133
15	15838	0.016	0.007	0.216
16	17215	0.016	0.006	0.235
17	18710	0.016	0.006	0.256
18	20331	0.016	0.005	0.278
19	22099	0.027	0.005	0.501
20	24017	0.032	0.004	0.656
21	26102	0.043	0.004	0.949
22	28369	0.048	0.004	1.167
23	30831	0.059	0.003	1.550
24	33505	0.106	0.003	3.039
25	36413	0.122	0.003	3.791
26	39573	0.090	0.003	3.061
27	43009	0.074	0.003	2.723
28	46742	0.069	0.002	2.748
29	50797	0.059	0.002	2.547
30	55207	0.053	0.002	2.493
31	59991	0.048	0.002	2.431

Now, we turn to the SEM images of the shales available in the literature to see whether a 30-micrometer microcrack-like throat exists (see Figure 6.11). We observe that the images do not show such a long microcrack. Hence, the NC model with a mono-size pore size distribution is not realistic.

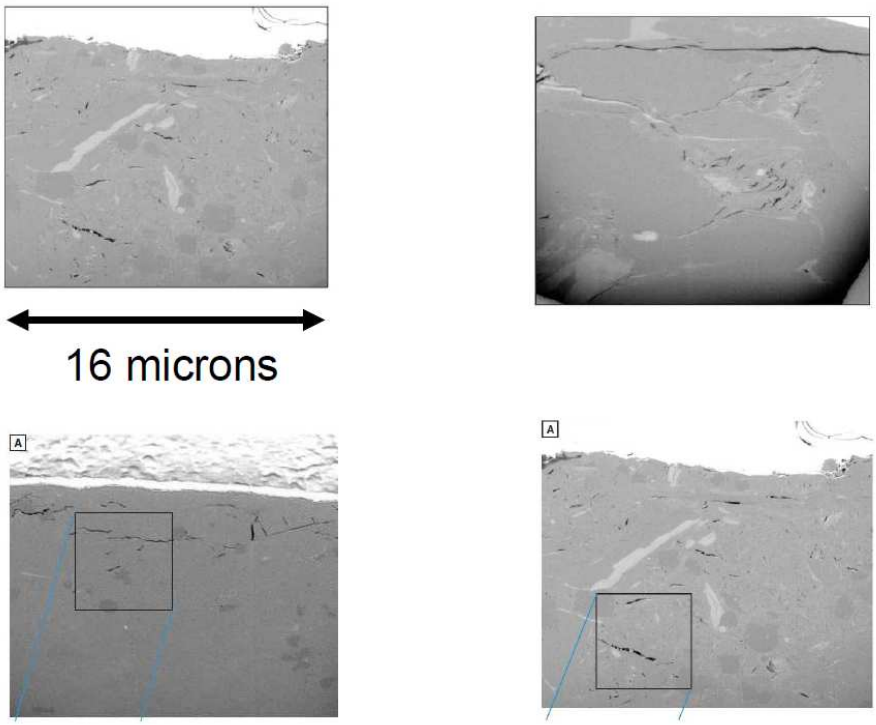

Figure 6.11: Scanning electron microscope (SEM) images of shales (courtesy of Heath et al., 2011). We do not observe a 30-micrometer microcrack and thus, MICP curves typical of such shales, such as Figure 6.1, do not support the notion of the NC model with mono-size throats.

It might be possible to capture the MICP data by implementation of a distribution of throat sizes but yet keeping the notion of large-aspect-ratio throat geometry. This scenario is very unlikely to occur at in-situ condition with confinement as we indicate subsequently from analysis of the shale images.

6.5. Effects of confining stress on the throat size

We investigate the effect of confining stress on the MICP experiment to better understand the pore structure of the shale. For confined and unconfined samples, we compare the capillary pressures at the same wetting phase saturation. This is to determine whether the size of the pore throat depends on the confinement and also which pore

throat geometries are more probable to be closed at in-situ condition. The in-situ condition here refers to the confined boundary condition.

Figure 6.12 shows mercury intrusion capillary pressures (MICP) of Kirtland and Tuscaloosa shale samples with and without confinement. We observe that the invasion is delayed to larger capillary pressures in the presence of confining stress. This is more obvious at low capillary pressures which correspond to throats with large characteristic sizes. This tells us that some throats with large characteristic sizes are closed at in-situ stress condition. With this observation in mind, we will analyze the SEM images of the shales (Figures 6.13-14) to decide whether the microcrack- or circular-like throats are more probable to be closed at in-situ condition.

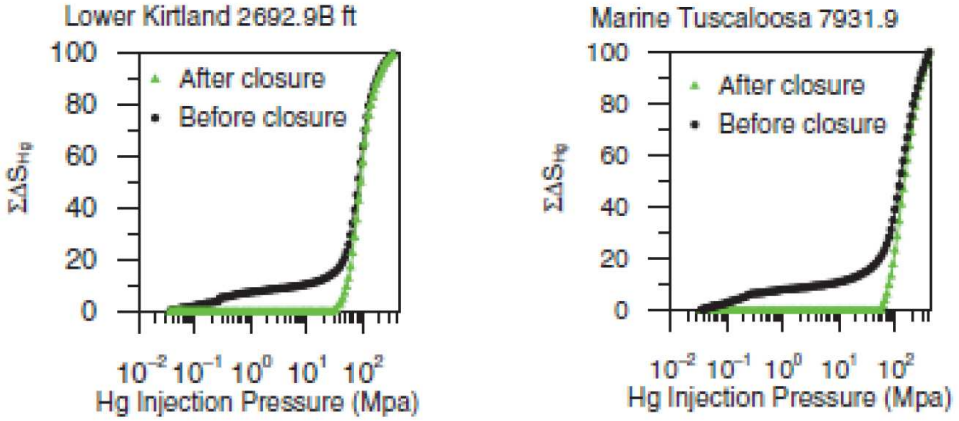

(a) (b)

Figure 6.12: Mercury intrusion capillary pressures (MICP) of (a) Kirtland and (b) Tuscaloosa shales (courtesy of Heath et al., 2011). The results show that the invasion of the void space occurs at a large capillary pressure if the in-situ stress condition is enforced. This imparts that some throats are closed at in-situ stress condition. The in-situ condition is represented by the confined test which is indicated by “After closure”.

6.6. Image analysis of shale

We are to explore SEM images of shales to see whether the microcrack-like throats have any orientation preference. This is to examine whether they are created because of unloading during the extraction.

Figure 6.13 shows the SEM images of the Eagle Ford and Barnett shales in which the up direction is not clear. Therefore, we are not able to indicate whether the microcrack-like throats are created because of unloading. However, we observe that the large-aspect-ratio throats have preferential orientation. Most of them are oriented from SW to NE direction in Figure 6.13(a) and from west to east in Figure 6.13(b). We conclude that these throats are not randomly oriented and have a preferential alignment. Our prediction is that they are created in the direction of maximum unloading. To assess this conclusion, we subsequently analyze the SEM images of shales for which the up direction is known.

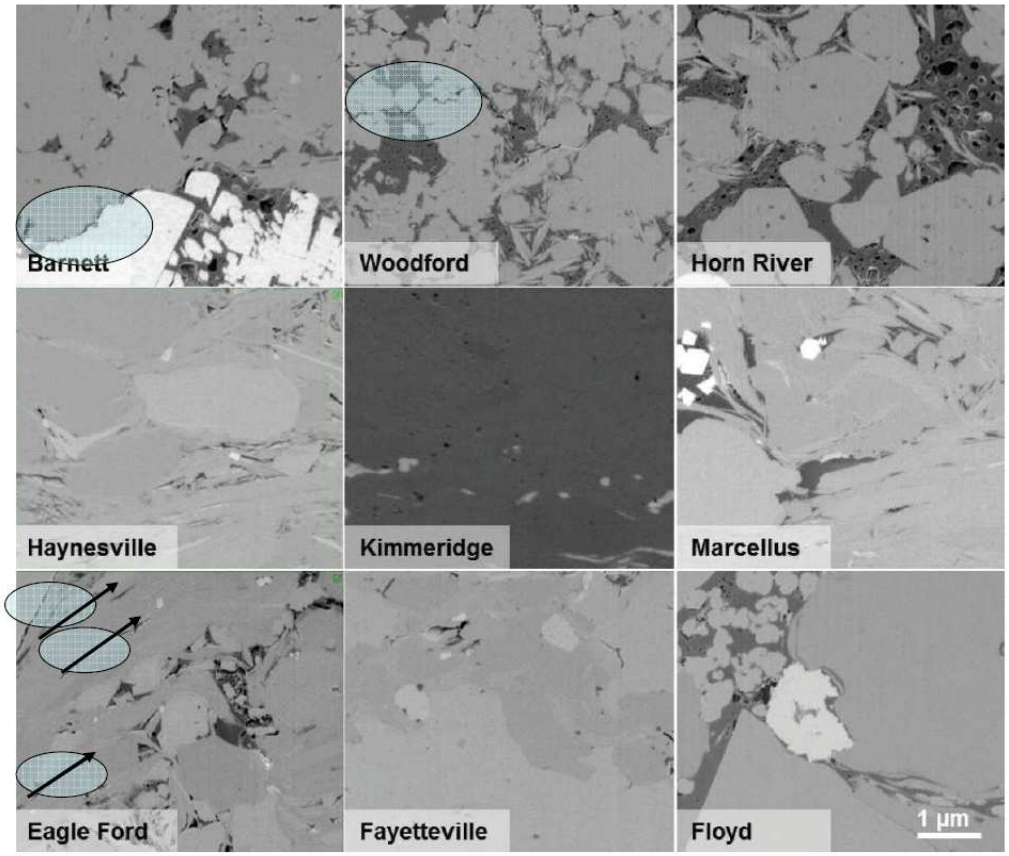

(a)

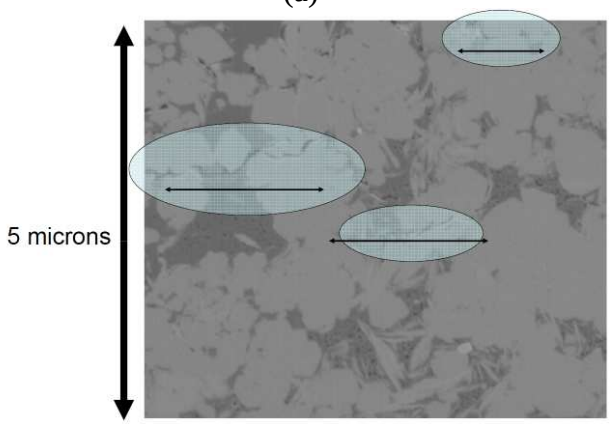

(b)

Figure 6.13: Scanning election microscope (SEM) images of (a) Eagle Ford and (b) Barnett shale samples. The Eagle Ford image is from Curtis et al., (2010) and the Barnett image from Sondergeld et al., (2010). The up direction of the reservoir is not clear here and thus, we are not fully sure if the microcrack-like throats are a result of unloading.

Now, we turn to the analysis of the shale images for which the up direction of the reservoirs is known. Figure 6.14 shows the SEM images (Heath et al., 2011) for which the up direction of the reservoirs is either top or bottom of the images. This means that we lower the confining stress in the up direction of the images the most. We observe that most of the microcrack-throats, which are highlighted with blue color, are perpendicular to that direction. The extension of the microcrack-like throats being perpendicular to the up direction of the reservoirs leads us to the conclusion that they are induced because of unloading and thus, they are closed at in-situ stress condition.

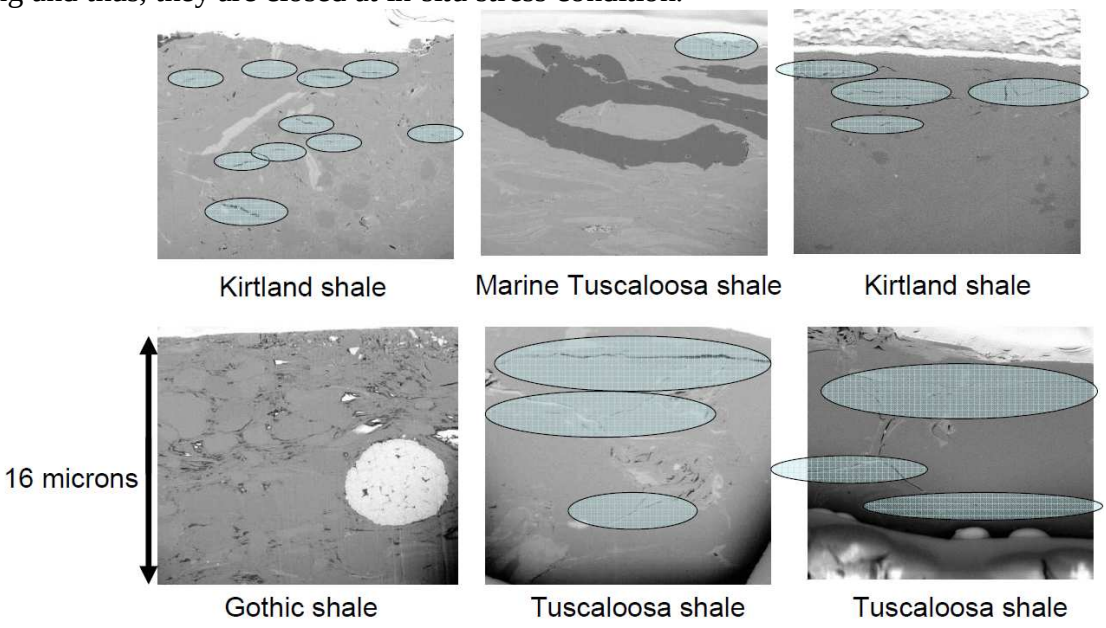

Figure 6.14: Scanning electron microscope (SEM) images of shales for which the up direction of the reservoirs is either top or bottom of the images (courtesy of Heath et al., 2011). This means that we have maximum stress decrease in the up direction of the images. We observe that most of the microcrack-like throats, indicated with blue color, are perpendicular to the up direction of the reservoirs. This shows that the unloading is the main reason for the creation of these large-aspect-ratio throats and thus, they are most probably closed at in-situ condition.

Our interpretation of the microcrack-like throats being perpendicular to the maximum load decrease is that they are induced because of load removal. Hence, they are more likely to be closed at in-situ boundary condition. This indicates that the tree-like pore model is more representative of the void space as the pore throats are circular and not microcrack-like.

6.6.1. Coordination number (z) of the shale

Both of our models suppose that the coordination number (z) of the pore is 3, 2, or 1. While this is clear for the NC model, it may not seem apparent for the tree-like pores. In the tree-like model, the characteristic lengths of the throats should be defined appropriately so that the coordination number remains smaller than or equal to 3. We will explain this in detail later. The coordination number of each pore shows the number of neighboring pores that are directly connected to that pore. It might be argued that the pores might have a larger coordination number and thus, our model has no advantage over a conventional pore model such as sphere packing (Bryant et al., 1993) in terms of representing the pore connectivity. The coordination number of the pore could be as large as 4 or 5 in a conventional pore model such as sphere packing. To investigate the pore connectivity of the shale, we analyze the image analysis results available in the literature (Dewers et al., 2012).

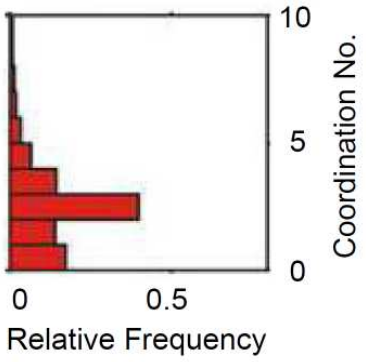

Figure 6.15: The relative frequency of the coordination number (z) of a Haynesville shale sample shows that the coordination number is mostly smaller than or equal to 3 (courtesy of Dewers et al., 2012). This corroborates our models by indicating that most pores have small coordination numbers (z).

Dewers et al., (2012) showed that the coordination number of a Haynesville shale sample is usually smaller than or equal to 3 (Figure 6.15). This indicates that our models provide a realistic representation of the void space in terms of pore connectivity. In the tree-like pore model, the coordination number is smaller than or equal to 3 under certain circumstances and in the NC model it is smaller than or equal to 2. We will elaborate the circumstances required for the tree-like model to have coordination number smaller than or equal to 3 later in the permeability estimation from MICP data.

We should emphasize here that the image analysis results are obtained without confinement and thus, we expect some pore throats vanish at in-situ condition. This says that the coordination number of the pores tend to be smaller than the results provided in Figure 6.15.

6.7. Permeability estimation from MICP

We estimate the single-phase permeability of the shale from MICP data. For this purpose, we first use the bundle-of-tubes model (Purcell, 1949) from the conventional

modeling approaches. Then, we employ the NC and tree-like pore models. This is to determine whether the predicted permeability is on the order of 10-100 nD, which is accepted for the matrix of the un-fractured shale (Sakhaee-Pour and Bryant, 2012).

6.7.1. Purcell method

We adopt the Purcell (1949) model here in which the void space is assumed to behave similar to the bundle-of-tubes. This means that the tubes can be taken to model the macroscopic transport properties of the porous medium such as permeability. We elaborated this model in chapter 2.

The bundle-of-tubes model assumes that the characteristic size of the pore throat invaded at the measured mercury pressure controls the flow behavior. The characteristic size the pore throat is determined assuming that the pore throat geometry is circular. We determine the permeability for the shale sample whose MICP is shown in Figure 6.1 after assuming that Purcell's lithology factor (F) is unity.

Table 6.2 shows the permeability estimation from the bundle-of-tubes model. Table 6.2 shows the permeability estimation in which P_c represents the capillary pressure, ΔS_{wi} the incremental change in the wetting phase saturation at the given pressure, d_i characteristic size of the throat, and $(\Delta S_{wi} d_i^2/32)$ the conductance of the throat. The sample permeability is obtained after determining the summation of the last column which is equal to 3.44 microD and implementing porosity of the sample which is equal to 4.64%. The single-phase permeability of the shale is found to be 160 nD. This calculation ignores the effects of non-continuum flow at high Knudsen numbers ($Kn > 10^{-3}$) and of adsorbed layer of methane molecules on walls of pores in kerogen (Sakhaee-Pour and Bryant, 2012). The adapted network modeling approach predicts that the

permeability decreases by a factor of about 4 if we account for both effects (Sakhaee-Pour and Bryant, 2012).

Table 6.3: Permeability estimation using the bundle-of-tubes model is indicated here. Here, P_c denotes the capillary pressure during mercury intrusion, ΔS_{wi} change in the wetting phase at the measured capillary pressure, d_i characteristic diameter of the tube. The estimated permeability is obtained after obtaining the summation of the last column and including the porosity effect ($=\phi\sum_i \frac{d_i^2}{32}\Delta S_{wi}$).

i	P_c (psi)	ΔS_{wi}	d_i (micrometers)	$\Delta S_{wi}\, d_i^2/32$
1	4837	0.005	0.044	323.27294
2	5367	0.005	0.040	261.98305
3	5832	0.005	0.037	222.66622
4	6339	0.005	0.034	188.77826
5	6891	0.005	0.031	159.74069
6	7490	0.005	0.029	135.01496
7	8139	0.005	0.026	114.10239
8	8845	0.011	0.024	193.08843
9	9614	0.011	0.022	163.84309
10	10449	0.005	0.020	69.17553
11	11355	0.011	0.019	117.50000
12	12340	0.011	0.017	99.49801
13	13408	0.011	0.016	84.04588
14	14575	0.011	0.015	70.86436
15	15838	0.016	0.014	90.88265
16	17215	0.016	0.012	76.67553
17	18710	0.016	0.011	64.80718
18	20331	0.016	0.011	54.97839
19	22099	0.027	0.010	78.19980
20	24017	0.032	0.009	78.99934
21	26102	0.043	0.008	89.41489
22	28369	0.048	0.008	84.15060
23	30831	0.059	0.007	87.05286

Table 6.3

24	33505	0.106	0.006	136.17021
25	36413	0.122	0.006	133.08344
26	39573	0.090	0.005	82.40027
27	43009	0.074	0.005	58.17819
28	46742	0.069	0.005	45.72473
29	50797	0.059	0.004	32.25399
30	55207	0.053	0.004	25.28258
31	59991	0.048	0.004	19.38830

6.7.2. Nooks and crannies (NC) model

We adopt the NC model here to predict the single-phase permeability. This method supposes that the void space includes microcrack-like throats extended through the rock. This is similar to the bundle-of-tubes model, in terms of connectivity, because it assumes that the parallel tubes can model the transport properties of the void space. However, unlike the bundle-of-tubes model, this model assumes that the pore throat geometry is rectangular. The single-phase permeability using the NC model can be expressed as follows:

$$k = F\phi\sum_i \frac{a_i^2}{12}\Delta S_{wi} \tag{6.3}$$

where a_i is the characteristic height of the pore throat and other parameters are similar to bundle-of-tubes model we elaborated in the literature review.

We assume that the lithology factor (F) is equal to unity here similar to our analysis in the bundle-of-tubes model for the sake of comparison. The NC model predicts that the permeability is equal to 106 nD for the shale sample whose MICP data are shown in Figure 6.1.

6.7.3. Tree-like model

By definition, the tree-like pore model cannot sustain steady-state flow. However, we can analyze transient pattern flow relatively simply in this model. A transient flow pattern can be induced in the void space by transient pulse decay (TPD) method which is often used to measure the gas permeability of the shale. In this method, gas is injected into a sample to elevate the pore pressure to a known value. Then, the sample is connected to a reservoir with constant volume which is at a lower pressure. Therefore, there is a pressure difference between the sample and the reservoir which decays as gas leaves the sample. The rate of decay with time is used to determine the permeability in this approach.

Figure 6.16 shows the pressure distribution in the void space from the tree-like pore model perspective. The pore pressure is a maximum value (P_{max}) initially everywhere (see Figure 6.16(a)) and it decreases along the throats when we start to evacuate the sample (Figure 6.16(b)) from the pore at the 3 o'clock position (one of the largest throats). Using the pressure distribution shown in Figure 6.16(c) which is based on the flow path from a larger pressure to a lower pressure, we estimate the permeability subsequently.

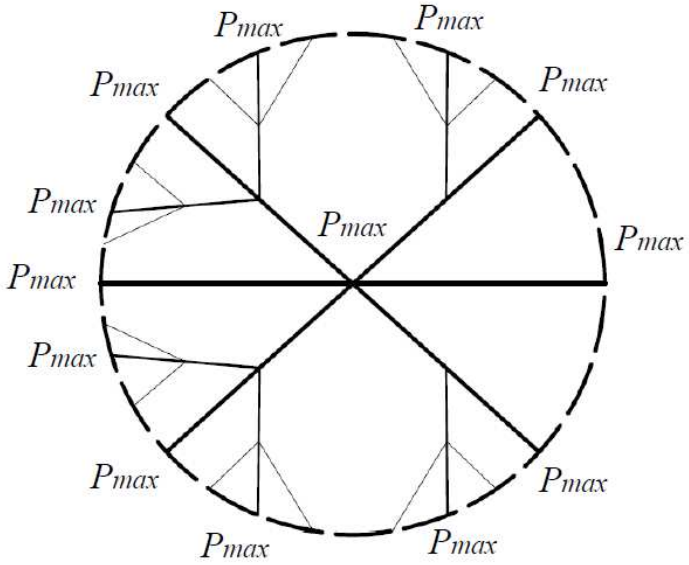

(a)

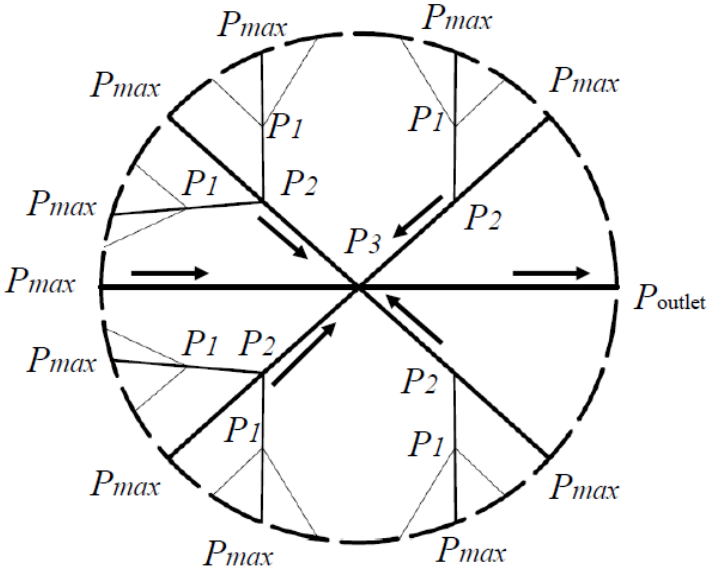

(b)

Figure 6.16: (a) illustrates the tree-like pore model at the start of transient pulse decay method ($t = t_0$) in which the pore pressure is uniform and equal to P_{max}. (b) The pore pressure distribution ($P_{max} \geq P_1 \geq P_2 \geq P_3 \geq P_{outlet}$) and flow pattern are shown after we start to evacuate the sample (($t > t_0$). The flow direction is indicated by arrows.

Following the flow path from a larger pressure to a smaller pressure, we determine the permeability. The conductance of pore throat, its porosity, and spatial distribution of the throats control the permeability. Here, the permeability is calculated using an equi-pressure plot. The equi-pressure plot is an equivalent demonstration of the pressure distribution in the network model in which pore throats with an identical characteristic size between equal pressures are lumped to an equivalent tube. The permeability of the equivalent tube is estimated as follows:

$$k_{tube} = \frac{\phi r^2}{8} \tag{6.4}$$

where k_{tube} is the permeability of the equivalent tube, ϕ porosity of the shale sample, and r the characteristic size of the pore throats for which we estimate from the MICP data.

For the permeability estimation, we also need to specify the length and cross section area of the equivalent tube. We suppose that the length of the equivalent tube is equal to the length of the pore throats accessed at the measured capillary pressure in MICP. The pore throats with similar characteristic size have the same length in the tree-like pore model and thus, we assign a single length to the equivalent tubes. In addition, we assume that the length of the widest throats is equal to the length of the sample (= L_1). The subscript refers to the measured capillary pressures so P_{c1} is the entry pressure. Further, the pore throats invaded at larger capillary pressures have smaller lengths. The throat lengths are assumed to decrease by a factor of 2 at each measured capillary ($L_1 = 2L_2 = 2^2L_3 = \ldots$).

We show a schematic of the tree-like pore model which contains pore throats with three characteristic sizes. We clarify the permeability estimation for this model. The equi-potential plot shows that the equivalent tubes are arranged in a mixture of series and parallel pattern. The equivalent tubes 3 and 2 with lengths equal to $L_1/4$ are between P_{max}

and P_3. These tubes form a parallel pattern and thus, we first obtain their outcome which is effective tube 3 (see Te_3 in Figure 6.17(b)). Te_3 is in series with the rest of equivalent tube 2 which is between P_3 and P_2. Hence, we determine their outcome which is effective tube 2 (Te_2). Te_2 then forms a parallel structure to the remainder of the plot and thus, same procedure should be followed to determine the effective permeability of the model. This is a loop-like procedure which should be adopted based on the number equivalent tubes. We will use this approach to estimate the permeability from the actual MICP data.

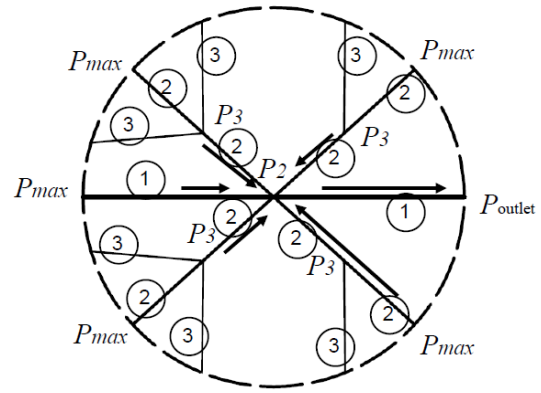

(a)

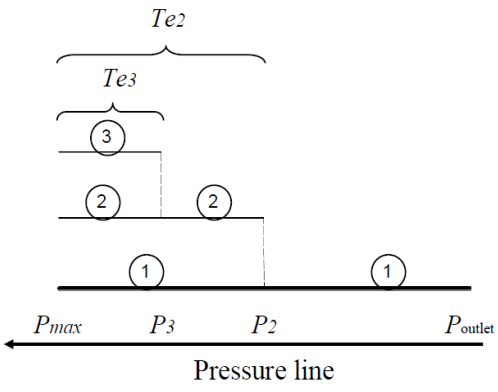

(b)

Figure 6.17: (a) Tree-like pore model with three characteristic throat sizes. Flow pattern indicates the pressure distribution during transient pulse decay (TPD). (b) is the equi-potential plot of the tree-like pore model with three equivalent tubes. In the equi-potential plot, the equivalent tubes are used to represent the pore throats with similar lengths, cross section area, and pressure drop as they are numbered.

The conductance of the equivalent tube is proportional to its permeability and total cross section area (~ $k_{tube} \times A_{tube}]_i$). We calculate the permeability from the characteristic size of the throats. However, the cross section area of the tube ($A_{tube}]_i$) is a strong function of the incremental pore volume invaded at each capillary pressure ($A_{tube} \times L_{tube}]_I = V_p \times \Delta S_{wi}$). This indicates that the cross section area of the tube is dependent on its length because the incremental pore volume is known from the MICP data. Thus, the predicted permeability of the tree-like pore model is a function of tube lengths and hence, it depends on the branching ratio ($L_{tube}]_i / L_{tube}]_{i+1}$). The tree-like pore models with branching ratios equal to 2 and 1.1 are shown in Figure 6.18 for clarity.

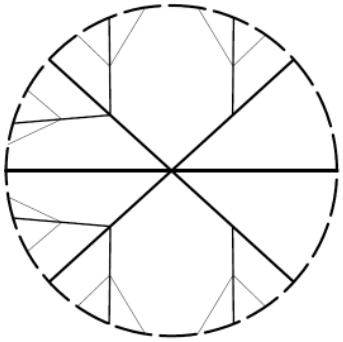

(a)

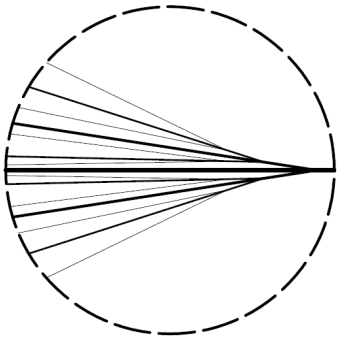

(b)

Figure 6.18: Tree-like pore models with branching ratios equal to 2 and 1.1 are shown in (a) and (b), respectively. The branching ratio is the ratio of the lengths of the throats accessed at two subsequent capillary pressures. The tree-like pore model assumes that a wider throat is longer.

To fully specify the tree-like pore model that mimics the shale pore structure, we calculate the number of pore throats accessed at each capillary pressure. This is to capture the MICP data shown in Figure 6.1. The number of the widest throats (d_1 = 44 nm) required could be determined from knowing the cross section area of the core sample, the sample porosity (4.64%), and increase in the wetting phase saturation at the entry pressure (ΔS_{w1} = 0.005). The characteristic length of the widest throat has also to be known, which we supposed earlier that it is equal to the length of the core samples. We present the number of throats (n_i) required at each capillary in a ratio form (n_{i+1}/n_i), in which the subscript i refers to the steps of capillary pressures as clarified see Table 6.2. The results are presented with respect to the wetting phase saturation, which is taken from Figure 6.1, and for different branching ratios. This calculation indicates that our tree-like pore model is capable of capturing non-percolating MICP the shale.

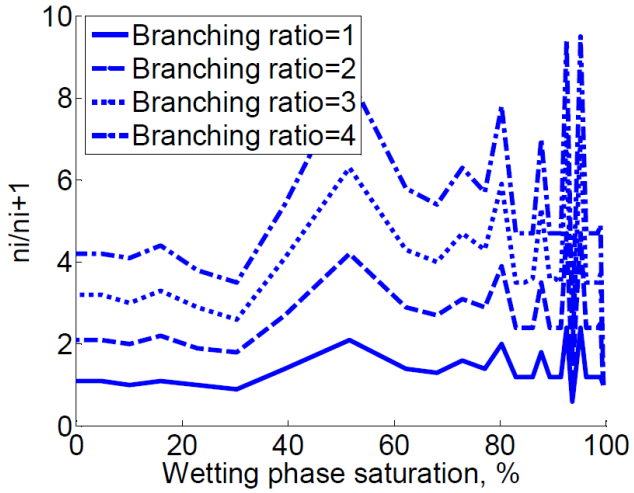

Figure 6.19: The number of throats of the tree-like pore model is determined to capture the MICP data shown in Figure 6.1. The number of pore throats required at each capillary pressure in the tree-like pore model (n_i) is presented in a ratio form ($=n_{i+1}/n_i$). The subscript i is clarified in Table 6.1.

Now, we analyze the coordination number (z) of the tree-like pore model. This is to determine whether the tree-like pore model yields a reasonable range of the coordination number (z) if the branching ratio is defined appropriately. The image analysis shows that the average of the coordination number is smaller than or equal to 3 (cf, Figure 6.15). To examine this, we average the coordination numbers obtained from the preceding analysis. Figure 6.20 indicates that the average of the coordination numbers value is close to 3 for small branching ratios. This means that the tree-like pore model with small branching ratio is representative of the void space and it is consistent with the image analysis results (cf. Figure 6.15).

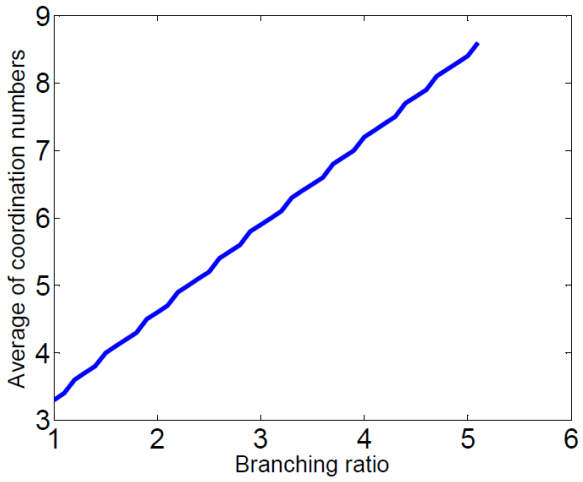

Figure 6.20: The average of the coordination numbers (z) of the tree-like pore model vs. branching ratio.

We implement the permeability determination approach described in Figure 6.17 for the MICP data shown in Figure 6.1. The estimated permeability vs. branching ratio is shown in Figure 6.21. The results indicate that the permeability of the model is between 15-27 nD which is in the acceptable range (~ 10-100 nD) for the un-fractured shale in the laboratory condition (Sakhaee-Pour and Bryant, 2012). This permeability is smaller at the

in-situ condition even by a factor of 4 because of the combined effects of the adsorbed layer of gas and gas slippage on the pore walls (Sakhaee-Pour and Bryant, 2012).

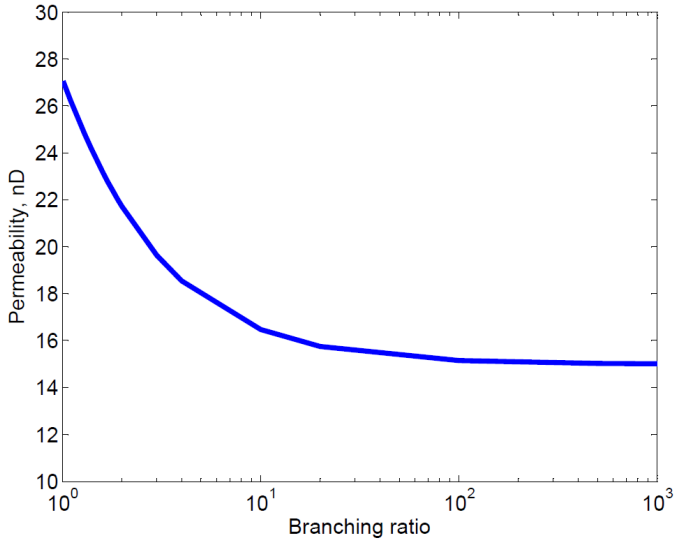

Figure 6.21: Variation of the permeability with branching ratio obtained from the tree-like pore model. The predicted permeability is between 15-27 nD which is in acceptable range for the matrix of the un-fractured shale (Sakhaee-Pour and Bryant, 2012). The branching ratio is clarified in Figure 6.18.

6.8. Conclusions

It is of great interest to have a better understanding of the pore structure of the shale in contrast to the conventional rocks such as unconsolidated sandstones that can be modeled by the sphere packing. With that in mind, we analyzed the mercury intrusion capillary pressure (MICP) data of the shale and proposed two pore structure models, i.e. tree-like model and nooks and crannies (NC). The proposed models adopt different pore throat geometries and connectivities. The void space of the tree-like structure takes circular tubes to model the pore throats that are connected in an acyclic pattern. In the tree-like model, there are multiplying branches with ever smaller throats. On the other

hand, the NC model assumes that the void space comprises microcrack-like (large-aspect-ratio) throats that are connected through the rock similar to the bundle-of-tubes model.

We took both models to predict the single-phase gas permeability without slippage and without adsorbed layer of gas from the MICP data. The NC model predicts that the permeability is 106 nD whereas for the tree-like pore model it is between 15-27 nD. These are both in the acceptable range of permeability (< 100 nD, Sakhaee-Pour and Bryant, 2012). We, however, judged that the NC model is not representative of the shale void space because the microcrack-like throats are more probably closed at in-situ condition in the presence of a confining stress. Hence, we deduce that the pore connectivity of the shale is more similar to the tree-like structure.

Chapter 7: Effects of adsorbed layer and slippage on the gas permeability of shale

7.1. Introduction

This chapter analyzes the dependency of the in-situ shale matrix permeability on the reservoir pressure. In this regard, we implement the effect of adsorbed layer in simple conduit geometries as a function of gas pressure. Subsequently, we adopt non-continuum flow models to account for non-zero slip velocity in the conduits. The presence of an adsorbed layer of gas molecules has a geometric implication (it reduces the cross section available for transport) and an influence on microscale boundary condition (slippage of gas being transported through the pore). Here, we examine a macroscopic consequence of these phenomena, namely the effect on the permeability of the rock to gas, by implementing these phenomena in a network model of the void space. The effects of adsorption and slippage depend on the size of the conduit, and though a network is not a literal model of shale pore space, it does serve as a convenient vehicle for examining the effect of a distribution of pore sizes. The results have implications for interpreting measurements of shale permeability to gas at laboratory conditions and for interpreting flow rates from production wells over time.

We refer to lab and field conditions extensively in here and for the sake of clarity, we define them here. The temperature is equal to 300 K and 360 K at the lab and field conditions, respectively. The pressure at the lab condition is presumed to be 5 MPa which is a common pressure for permeability measurement using transient pulse decay (TPD) (Billiotte et al., 2008). The gas permeability of shale at this condition is on the order of 10 nD (Billiotte et al., 2008). We assume the thickness of adsorbed layer is negligible at lab condition. This is a plausible assumption as the ratio of no-slip hydraulic conductance without adsorbed layer to no-slip hydraulic conductance with adsorbed layer at 5 MPa is

close to unity regardless of throat size, as we will show later in Figure 7.4. For estimating the gas conductance and permeability, we further suppose the gases at the lab and in-situ conditions are, respectively, N_2 and CH_4. For convenience, we use the terms "liquid conductance" and "liquid permeability" to refer to hydraulic conductance computed with a continuum model and no-slip boundary condition at pore walls. We use the terms "gas conductance" and "gas permeability" to refer to the conductance when slippage is taken into account. Both "gas" and "liquid" conductance can be computed when an adsorbed layer is present. We denote the gas and liquid permeabilities at the lab condition by $k_{g,lab}$ and $k_{l,lab}$, respectively. The pressure varies at the field condition controlling the thickness of the adsorbed layer. The pressure also affects the Knudsen number (Kn) and the slippage. For the field condition, the gas and liquid permeabilities are represented by $k_{g,in\text{-}situ}$ and $k_{l,in\text{-}situ}$, respectively.

7.2. Gas flow regimes

Knudsen number (Kn) (Knudsen, 1909) is used to differentiate flow regimes in conduits at micro- and nanoscale. This non-dimensional parameter is defined as:

$$Kn = \frac{\lambda}{\Lambda} \tag{7.1}$$

where λ denotes the mean free-path length of gas molecule and Λ the characteristic length of the channel. The flow regime changes from continuum model to discrete particles as Kn increases. Substituting the mean free path yields the following relation (Roy et al., 2003):

$$Kn = \sqrt{\frac{\pi}{2\bar{R}T}} \times \frac{\mu}{\rho\Lambda} \tag{7.2}$$

where μ is the gas viscosity, ρ the density, T the prevailing temperature, and $\bar{R}$ the specific gas constant. The specific gas constant is the ratio of universal gas constant, R, to the molar mass, m. On the other hand, the length scale Λ equals the diameter and aperture

height in circular tube and slit, respectively. For N_2 and CH_4 at the range of temperatures (300 K to 360 K) and pressures (5 MPa to 28 MPa) of interest here, the range of values of λ is 0.3 to 2.2 nm. For pore sizes Λ in the range 3 nm to 30 nm, we thus encounter values of *Kn* in the range of 10^{-2} to 10^{0}.

7.2.1. Continuum regime

The flow regime is categorized based on *Kn* as summarized in Table 7.4 (Roy et al., 2003). This table indicates the Navier-Stokes equations with no-slip boundary condition are appropriate only for small *Kn* ($Kn < 10^{-3}$). In other words, the classical continuum model assumptions (momentum transfer via bulk phase viscosity, fluid velocity matches solid velocity at walls) cannot always provide accurate results.

Table 7.4: Fluid flow regimes defined by ranges of Knudsen number (*Kn*).

Kn	$0\text{-}10^{-3}$	$10^{-3}\text{-}10^{-1}$	$10^{-1}\text{-}10^{1}$	$>10^{1}$
Flow regime	Continuum	Slip	Transition	Free-molecular

Here, we indicate how Knudsen (1909) classified the flow regimes as listed in Table 7.4. We elaborate how the ratio of the mean free-path length of gas molecule (a) to the characteristic size of the conduit (*d*) changes. For this purpose, we show the number of gas molecules inside a constant-size conduit at different gas pressures ($P_1 < P_2 < P_3 < P_4$). The number of gas molecules inside a conduit decreases (less dense population of the gas molecules) as we lower the gas pressure. Lowering the gas pressure also increases the mean free-path of the gas molecules (*a*). Compare the number of gas molecules in Figure 7.1(i). The increase in the mean free-path results in a higher *Kn* as the characteristic size of the conduit (*d*) is assumed to be constant. It is more appropriate to adopt a continuum model for a more dense population of the gas molecules. With that in mind, Knudsen

defined *Kn* as a distinguishing parameter for selecting flow models. He stated that the continuum flow models are legitimate for low Knudsen number flows, corresponding to a more dense population of the gas molecules, and other non-continuum models should be taken at higher *Kn*.

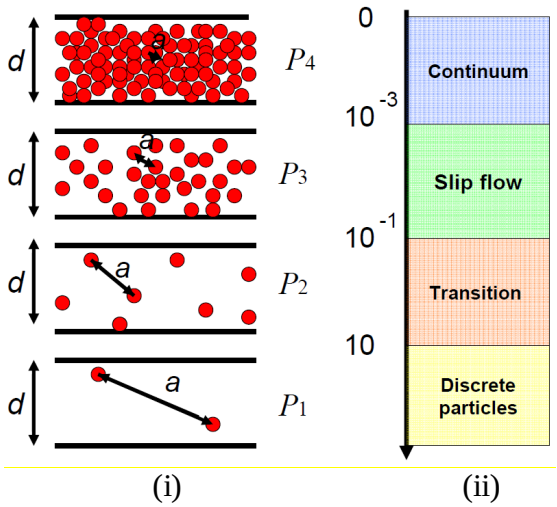

Figure 7.1: (i) shows the mean free-path of the gas molecules (*a*) at different gas pressures ($P_1 < P_2 < P_3 < P_4$) . The gas molecules are shown by red dots. The mean free-path of the gas molecules increases at lower pressures and this leads to a higher *Kn* for a constant size conduit (*d*). (ii) indicates the corresponding flow regimes for the assumed gas pressures.

7.2.2. Slip-flow regime

The ratio of molecule-wall to molecule-molecule collisions increases as *Kn* increases However, the molecule-molecule interaction is still dominant in the slip-flow regime. Therefore, Navier-Stokes equations were suggested (Karniadakis et al., 2005) to remain valid for this domain ($10^{-3} < Kn < 10^{-1}$). A first-order slip boundary condition was applied to include the effect of molecule-wall collisions (Roy et al., 2003). After

implementing the tangential momentum coefficient as shown in Appendix, the gas permeability can be estimated as:

$$k_g = k_l(1+\alpha_1 Kn) \tag{7.3}$$

where k_l is the permeability of the conduit to liquid (when the no-slip boundary condition applies), k_g the gas permeability of the conduit, and α_1 the permeability enhancement. The liquid permeability is assumed constant (i.e. independent of pressure) and estimated based on the characteristic length size of throat from conventional theory. The coefficient α_1 depends on the geometry of conduit. It is about 5 for circular cross sections (see Equation A.9).

The slip flow regime can also be simulated using dusty gas model (DGM) (Mason and Malinauskas, 1983). This model adopts a linear combination of gas transport mechanisms to predict the overall flow rate. It was mainly based on the empirical observation (Graham, 1876) and the theoretical explanation was proposed later (Mason and Malinauskas, 1983). The total mass flux of single-size conduit is calculated as:

$$J_{total} = J_{visc} + J_{Kn} = -\frac{k_l}{\mu} n\nabla p - D_{Kn}\nabla n = -(\frac{k_l}{\mu} p + D_{Kn})\frac{\nabla p}{RT} \tag{7.4}$$

where ∇p is the pressure gradient and D_{Kn} the Knudsen diffusivity coefficient. This relation can also be written in terms of gas permeability as shown in below:

$$J_{total} = -(\frac{k_l}{\mu} p + D_{Kn})\frac{\nabla p}{RT} = -\frac{k_g p}{\mu}\frac{\nabla p}{RT} \tag{7.5}$$

where k_g is the single phase gas permeability. Substituting the Knudsen diffusivity coefficient and implementing ideal gas assumption yield the gas permeability relative to the no-slip permeability in terms of Knudsen number as follows:

$$\frac{k_g}{k_l} = (1+\frac{D_{Kn}\mu}{k_l p}) = 1+\lambda_1 Kn \tag{7.6}$$

where λ_1 is the permeability enhancement equal to 13.58 for circular cross section as clarified in Appendix. This relation indicates that the first-order models (Equation (7.3))

and DGM (Equation (7.8)) suggest similar trend for the gas permeability, i.e. a linear function of Knudsen number.

Equation (7.6) is the analog of Klinkenberg's correction (Klinkenberg, 1941) for a single conduit. In the Klinkenberg's correction, the permeability to gas is evaluated at several pressures for a core sample instead of a single conduit. For steady flow experiments, the pressure is replaced by the average of inlet and outlet pressures across the core. The term $\frac{D_{Kn}\mu}{k_l}$ is determined empirically as the slope of the measured gas permeabilities plotted against reciprocal pressure.

While the first-order slip model and DGM indicate a qualitatively similar trend for the gas permeability, the rate of change with Knudsen number is different. The high Knudsen number is attained by decreasing the throat size in the first-order slip model. In this case, molecule-molecule collisions are not necessarily infrequent, rather, they are less frequent than molecule-wall collisions. On the other hand, the low density of the gas is the reason for the slippage in DGM. Note that reductions in both the throat size and the density increase the Knudsen number (see Equation (7.2)). Consequently, the permeability enhancements are obtained by measuring the flow rates. The in situ condition for gas shale corresponds to large gas density (~ 100 kg/m^3). The Knudsen number in this situation is large because shale conduits are very small. Thus, in this study, we use the first-order slip model in the range $10^{-3} < Kn < 10^{-1}$.

7.2.3. Transition regime

The physics of the transition flow regime is complicated and most models are to predict the computational results of the Monte Carlo simulations (Karniadakis et al., 2005). The proposed models implement different shear stress laws in the Navier-Stokes equations. The higher order gradients of the velocity are implemented in the proposed

models and the velocity profile is subject to higher order boundary conditions. To capture the flow rate, the corresponding mass flow rate for a circular tube was proposed as (Karniadakis et al., 2005):

$$\dot{M} = [1+1.358\tan^{-1}(4Kn^{0.4})\times Kn][1+\frac{4Kn}{1+Kn}]\frac{\pi R^4}{8\mu}\bar{\rho}\nabla P \tag{7.7}$$

where $\dot{M}$ is the mass flux and $\bar{\rho}$ the average density. The coefficients are obtained by fitting the equation to the Monte Carlo simulation results. We can express the gas permeability by dividing the mass flow rate to no-slip condition. Therefore, the ratio of gas permeability to no-slip permeability can be expressed as:

$$\frac{k_g}{k_l} = [1+1.358\tan^{-1}(4Kn^{0.4})\times Kn][1+\frac{4Kn}{1+Kn}] \tag{7.8}$$

This indicates the nonlinearity of permeability increase with *Kn*. For the sake of convenience, we develop a polynomial form for the permeability enhancement for $0.1 < Kn < 0.8$, which lies within the range of interest for shale gas reservoirs. A second order polynomial works well:

$$\frac{k_g}{k_l} = 0.8453 + 5.4576Kn + 0.1633Kn^2 \tag{7.9}$$

where the coefficients are calculated using the nonlinear regression model (Mendenhall et al., 1989) and the coefficient of regression is found 0.99. Note that the above equation is valid only for transition flow regime. Also, the gas permeability is no longer a linear function of *Kn*. This reveals that the Klinkenberg's correction cannot be employed for higher Knudsen number flow regimes.

We use gas permeability term "k_g" (Equations (7.3), (7.6), and (7.9)) to express flow rate with respect to no-slip viscous Stokes model that is usually denoted by "k_l". Thus, we adopt the gas permeability expression only to present the results in a familiar form for the petroleum industry and "k_l" is only representative of the "continuum model".

7.2.4. Free-molecular regime

For completeness, we include the free-molecular regime, which is relevant for gas phase transport at ambient conditions. The mass flow rate of free-molecular regime was modeled by Knudsen (1909). This model implements flux due to a density gradient of the molecules as follows:

$$J_{Kn} = -D_{kn} \nabla n_i \tag{7.10}$$

where J_{Kn} is the mass flux of component i, D_{kn} the Knudsen diffusivity coefficient, and ∇n_i the density gradient. Unlike ordinary diffusion, only one component is considered to predict the flow rate in this mechanism. This model requires Knudsen diffusivity which is usually measured experimentally (Reinecke and Sleep, 2002). It was analytically derived only for a long tube with a constant circular cross section area (Roy et al., 2003) as follows:

$$D_{kn} = \frac{d}{3}\sqrt{\frac{8RT}{\pi m}} = \frac{d}{3}\bar{v} \tag{7.11}$$

where d is the tube diameter, m the molar mass, T the ambient temperature, R the universal gas constant which is equal to 8.314 in SI units, and $\bar{v}$ the average velocity of molecules.

7.3. Adsorbed layer

The effect of adsorbed gas is neglected in modeling flow through conventional rock. This is reasonable because the occupied volume is negligible compared to the total void space in conventional rocks. However, the adsorbed volume of CH_4 is crucial in shale as the throats are often smaller than ten nanometers and much of the void space is in the organic material, for which CH_4 has a large affinity. While molecular adsorption

can occur on any surface, the adsorbed layer of interest here is on the organic material. This layer diminishes in thickness as the pressure decreases.

We analyze the effect of adsorbed layer on the single throat conductance. The ratio of the throat conductance without adsorbed layer to that of in-situ condition (gas adsorbed at in-situ temperature and pressure) is evaluated. The conductance without the adsorbed layer is computed by assuming a liquid phase is flowing. The purpose of this calculation is simply to isolate the geometric effect of the adsorbed layer. We assume the thickness of adsorbed layer is 0.7 nm at 28 MPa (Ambrose et al., 2010) and decreases linearly with reducing pressure. We further suppose the cross sectional area of the throat is circular considering the scanning electron microscope (SEM) images (Cipolla et al., 2010; Karniadakis et al., 2005). For the calculation of "liquid" (i.e. no-slip) flow, we assume the conductance of the circular tube depends on the fourth power of characteristic size, in agreement with Stokes flow of a Newtonian fluid. The influence of adsorbed layer is important for the throat sizes smaller than 50 nm which constitute a significant fraction of shale pores. For a typical shale sample, the characteristic throat size of 6 nm corresponds to the largest fraction of conduits as shown in Figure 7.2.

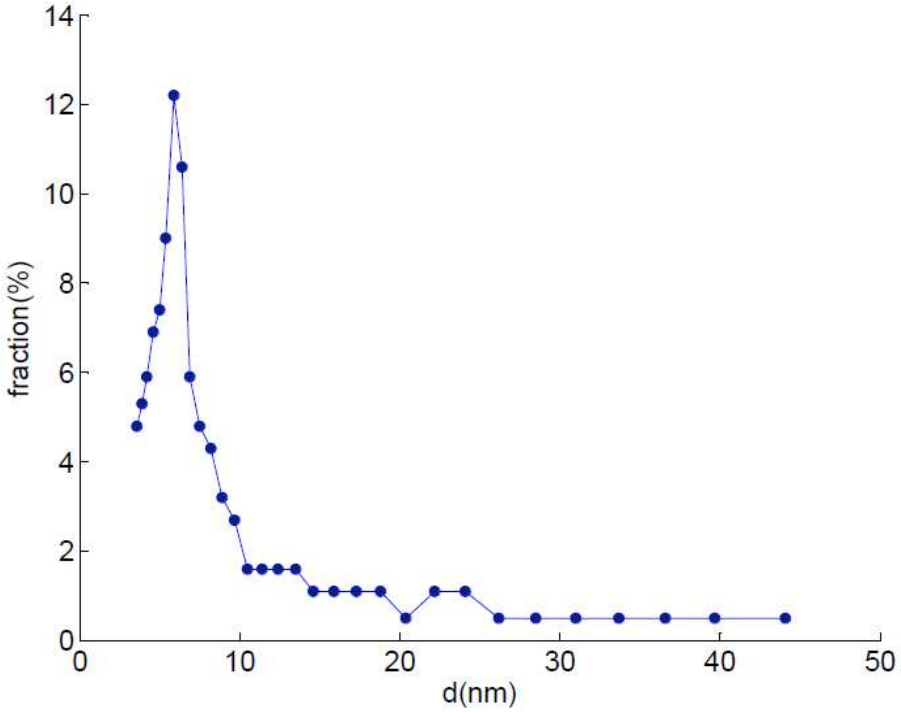

Figure 7.2: Pore size distribution of a Barnett shale sample obtained from mercury intrusion capillary pressure (MICP).

The adsorbed layer of CH_4 on pore walls significantly reduces cross-section in pores smaller than 10 nm, as illustrated in the cross section of circular tubes in Figure 7.3. The pore throat at lab condition is reduced by the adsorbed layer that is indicated by green color. The thickness of adsorbed layer is assumed to be 0.7 nm which is representative of in-situ condition at 28 MPa here. We observe that the change in the cross-section area is significant and, thus, it has to be taken into account if we want to have a better understanding of in-situ condition.

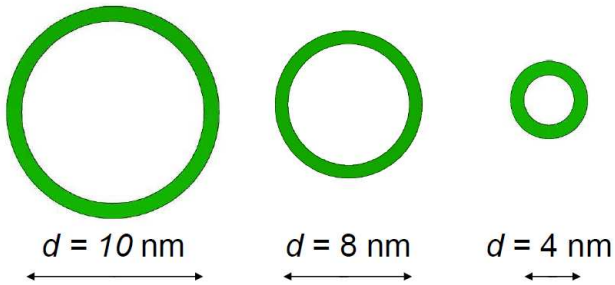

Figure 7.3: Change in the cross section area of the pore throats smaller than 10 nm is shown here. The adsorbed layer is shown with green color and assumed to be 0.7 nm which is representative of 28 MPa. The decrease in the cross-section area is notable because the pore throats are extremely narrow.

We build our pore space model based on the SEM images of shale and the drainage experiment. Some images of Barnett shale available in the literature are shown in Figure 7.4. The high resolution images indicate many throats exist in organic materials. The affinity of gas molecules for organic materials means that these throats constitute the void space which is altered by desorption. It has been argued that the fluid flow in organic materials is mainly single gas phase (Wang and Reed, 2009). Therefore, we propose a network model for gas permeability that includes only voids within organic matter.

7.4. Analysis of single cylindrical conduit

We analyze the conductance of a single-sized throat to study the effects of adsorbed layer and slippage. Then, we build a network model to examine these effects when the connected throats exhibit a distribution of sizes. Although the network does not explicitly represent the arrangement of voids in a shale, it does yield a first-order estimate of difference in the gas flow behavior through the shale at different conditions, e.g. high pressure (early in life of a well) versus low pressure (after substantial gas production) or field condition versus lab condition. We take into account the effects of adsorbed layer

and slippage on the conductance of each throat in the network. Consequently, we develop a characteristic plot mapping the measurements taken at typical lab conditions to the in-situ conductance of each throat.

Before considering the network, we investigate the effects of adsorbed layer and flow slippage on the conductance of a single throat. In this regard, we consider pore size distribution (inferred from mercury porosimetry) and SEM of the Barnett shale sample shown in Figures 7.2 and 4, respectively. We assume the void space is a network of cylindrical throats.

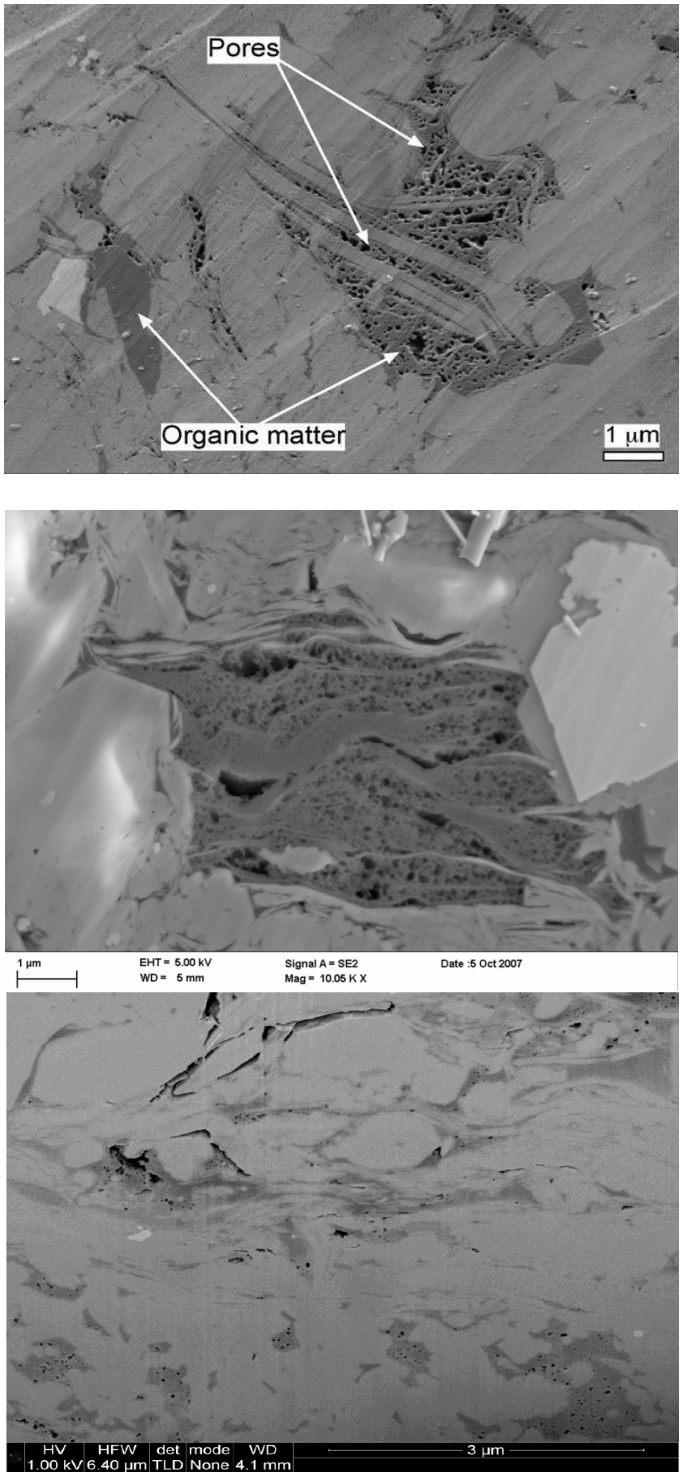

Figure 7.4: Scanning electron microscope (SEM) images of Barnett shale (Wang and Reed, 2009; 2008; Ambrose et al., 2010).

We begin by analyzing the effect of adsorbed layer on the liquid conductance of a single-sized throat. The goal is simply to quantify the geometric effect of reducing the throat size as the thickness of the adsorbed layer increases. Thus, slip is ignored; the calculations assume no slip on the adsorbed layer. The role of pressure in this analysis is merely to change the thickness of the layer. The results are presented in terms of the ratio of throat conductance without adsorbed layer to the conductance with adsorbed layer (see Figure 7.5). We observe that the adsorbed layer is crucial in estimating the conductance (with a no-slip boundary condition), especially at larger pressures and in smaller pore throats in the ranges of interest. The ratio of liquid conductances is larger at smaller throat sizes because the layer thickness, which is constant at a given pressure, occupies a greater fraction of the cross-section in smaller throats.

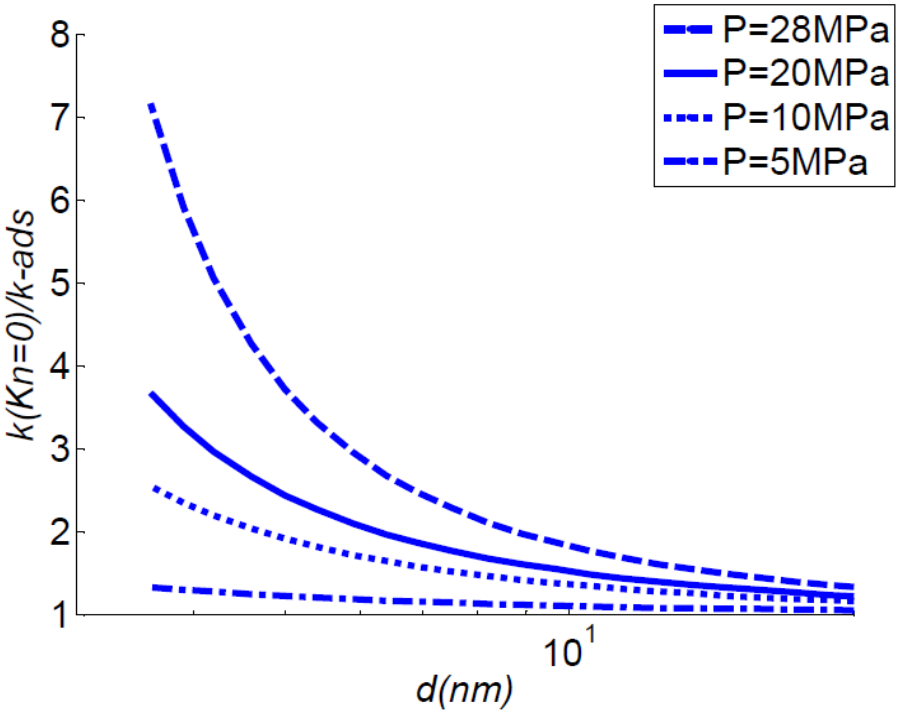

Figure 7.5: Effect of adsorbed CH_4 layer(s) on hydraulic conductance of a single cylindrical conduit. The ratio of "liquid" conductance without adsorbed layer ($k(Kn=0)$) to "liquid" conductance with adsorbed layer (k_{ads}) increases as pressure increases and as conduit diameter decreases. Liquid conductance refers to single phase laminar flow with no-slip boundary. Thickness of adsorbed layer is proportional to pressure.

Next, we explore the importance of slippage on the gas conductance. To this aim, we calculate the ratio of gas to liquid conductances. The conductances are computed assuming that no adsorbed layer exists. The only effect of pressure is thus to change *Kn* and hence the degree of slip. The temperature is fixed at 300 K. As before, the liquid conductance is computed with no-slip boundary condition to serve as a reference value. The ratio of gas to liquid conductances is shown in Figure 7.6. The calculation reveals the slippage plays an important role in smaller throat sizes and at lower pressures. For instance, the gas conductance of a 6 nm throat, which has the largest fraction of throat sizes in Figure 7.2, is larger than the liquid conductance by a factor of 1.5 at P = 20 MPa. This ratio increases nonlinearly with decrease of pressure revealing that the slippage becomes more important at late production.

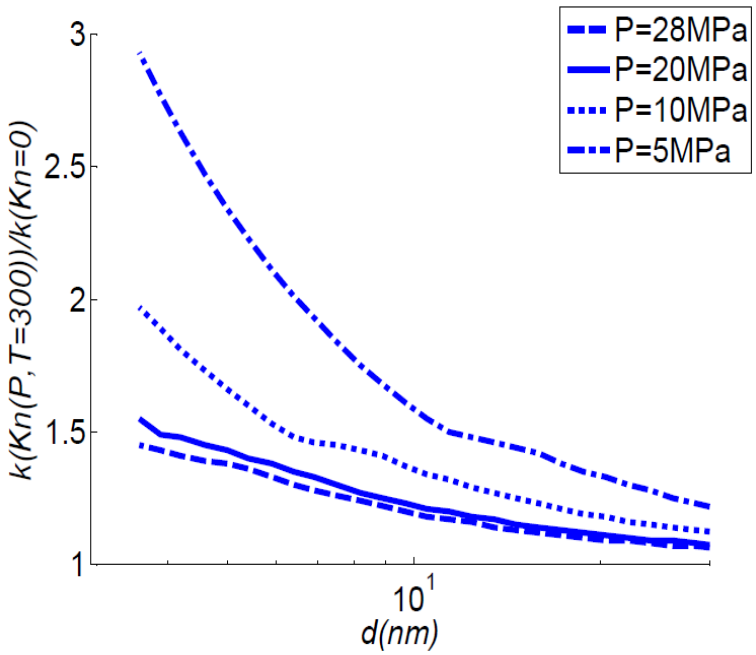

Figure 7.6: Effect of slip at pore walls on hydraulic conductance of a single cylindrical conduit. The ratio of gas conductance with slippage (*Kn* evaluated at 300 K and at pressure as per legend) to liquid conductance without slippage, $k(Kn=0)$. Both conductances assume no adsorbed layer is present. The value of Knudsen number changes with pressure.

Now, we consider the combination of the competing effects of the adsorbed layer and slippage on the gas conductance. The adsorbed layer reduces the conductance by reducing the cross sectional area. Slippage enhances the conductance by facilitating the molecule movements at the throat surface. Both effects depend on pressure. To analyze this competition, we calculate the ratio of gas conductance with adsorbed layer to liquid conductance without adsorbed layer. As above, the liquid conductance is calculated with no-slip boundary condition to serve as a reference value. The gas conductance is obtained by computing slip flow within the open cross-section of the throat remaining after implementing the adsorbed layer at the specified pressure. The temperature is held constant at 360 K. Figure 7.7 shows qualitatively different trends, depending on pressure. At large pressures, the ratio of gas conductance at in-situ conditions to the corresponding no-slip conductance increases as the pore size increases. At small pressures, the ratio decreases as the pore size increases.

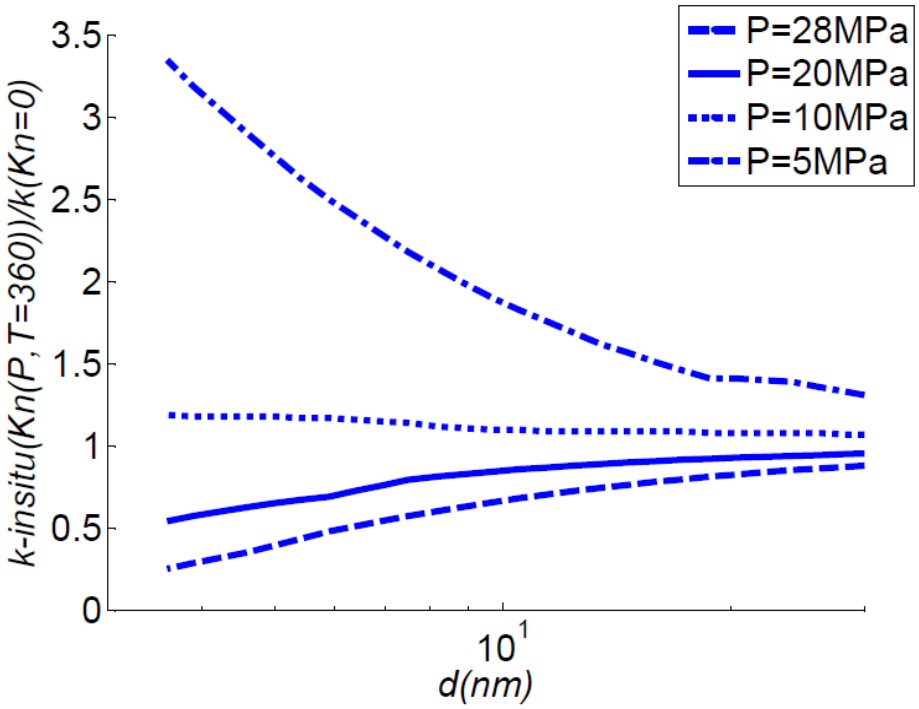

Figure 7.7: Combined effects of adsorbed layer and slip on hydraulic conductance of a single cylindrical conduit. The ratio of gas conductance, $k_{in\text{-}situ}$, with adsorbed layer and slippage (in-situ condition of 360 K and P as per legend) to liquid conductance, $k(Kn=0)$, without adsorbed layer and without slippage. This behavior is relevant to evolution of permeability during production.

This calculation helps us understand which effect governs the flow behavior at different stages of production. The comparison between gas and liquid conductances is to analyze the gas conductance variation versus a reference value. It compares the gas conductance (360 K, various P) which is representative of reservoir condition to liquid conductance, the reference value evaluated in the absence of an adsorbed layer and ignoring slip. The analysis shows the adsorbed layer dominates the flow behavior at high pressure (P = 28 MPa in Figure 7.7) regardless of the throat size. That is, the gas conductance is smaller than the reference conductance for all throat sizes because the adsorbed layer significantly reduces the cross-section for gas flow. The influence is

greater for smaller throats. However, the slippage has the primary effect at small pressures (P = 10 MPa or P = 5 MPa). That is, the gas conductance is greater than the reference conductance for all throats, with the effect being greater in narrower throats. The implication of Figure 7.7 is that the adsorbed layer should be taken into account for modeling gas transport during early production while the influence of slippage is dominant during later production.

Finally, we compare the gas conductances at lab and in-situ conditions for the single tube study. This is useful for estimating gas permeability in field from laboratory measurement. The adsorbed layer is presumed negligible at lab condition as the pressure (5 MPa) is low; the curve for the corresponding pressure in Figure 7.5 shows that the correction is less than 25% for all throat sizes. The thickness of adsorbed layer varies at in-situ condition depending on the pressure. Note that the slippage occurs in both conditions. We calculate the gas conductance at lab condition (T = 300 K) from the liquid conductance accounting for slippage at lab pressure in the relevant flow regime (Knudsen number criterion evaluated at 300 K and 5 MPa) by means of Equation (7.2), (7.3) or (7.9). For the in-situ condition, we compute the cross sectional area open to flow depending on the thickness of adsorbed layer. The gas conductance is computed from the liquid conductance at the field pressure after implementing the slippage. Figure 7.8 shows that the gas conductance at laboratory condition is notably higher than the in-situ condition at larger pressures. This is because of the lack of adsorbed layer and the enhancement of slippage at laboratory condition vs. in-situ condition. Clearly, the laboratory measurements should be corrected for any flow modeling at the field condition. Considering the importance of this issue, below we will analyze the laboratory measurements using network modeling and propose a correction.

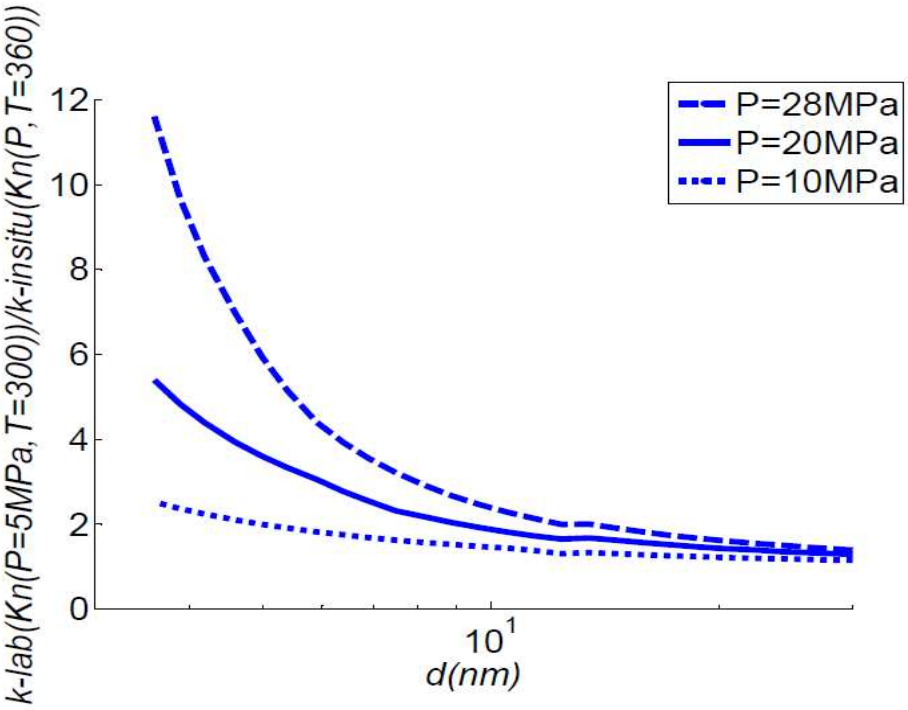

Figure 7.8: The ratio of gas conductance, k_{lab}, without adsorbed layer and with slippage (lab condition 300 K and 5 MPa) to gas conductance, $k_{in\text{-}situ}$, with adsorbed layer and slippage (field condition 360 K and pressure as per legend) increases as pressure increases and as cylindrical throat size decreases. These curves are relevant to estimating field permeability from laboratory measurements.

Liquid permeability is also of interest in shale, either for the problem of water production or for the challenge of "tight oil" production. To estimate liquid permeability at field condition from the gas permeability measured at laboratory condition, we calculate the ratio of gas to liquid conductances of a single cylindrical conduit. As above, the adsorbed layer at lab condition is negligible because of the low pressure. Therefore, the gas conductance at the laboratory condition is computed from the liquid conductance by implementing the slippage at the laboratory pressure and temperature (5 MPa, 300 K). For the liquid conductance at the in-situ condition, we calculate the throat area not obstructed by the thickness of adsorbed layer. The thickness of adsorbed layer depends

on pressure. We ignore the swelling effect for the in-situ condition which may reduce the hydraulic conductance. This may occur because of the presence of the water in the formation which is not available to the same amount at the laboratory condition. The ratio of gas to liquid conductances at lab and field conditions is shown in Figure 7.9. The results reveal the gas permeability obtained at lab condition is significantly larger than the liquid permeability at in-situ condition. The ratio of permeabilities estimated here is larger than the preceding analysis (Figure 7.8) since the liquid does not slip at lab condition. In reality, the ratio of gas to liquid conductances may be even greater than in Figure7.9 since the hydraulic conductance of throat decreases because of possible swelling clays present in the formation.

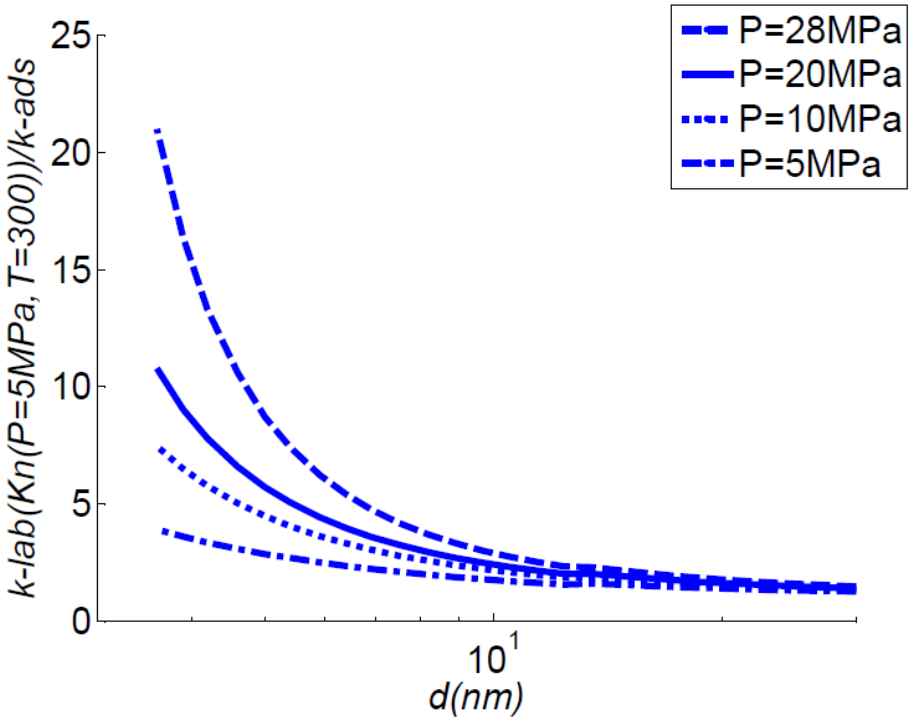

Figure 7.9: For a single cylindrical tube, a lab measurement of gas permeability greatly overestimates the permeability to liquid in the reservoir, as shown by the ratio of gas conductance, k_{lab}, with slippage and without adsorbed layer (lab condition of 300 K, 5 MPa) to liquid conductance, k_{ads}, without slippage and with adsorbed layer (field condition 360 K, P as in legend). Pressure determines thickness of the adsorbed layer.

7.5. Analysis of network of cylindrical conduits of distributed sizes

We employ a regular square lattice network (Bennett et al., 1962) to model the gas flow through organic materials in shale. We adopt the pore size distribution from the drainage experiment shown in Figure 7.2. We also assume the width of network (transverse to the direction of flow) and throat length are, respectively, 17 nm and 50 nm. The model width is chosen so that the network model yields a desired porosity. Here, 17 nm is the value which results in the desired porosity of 10%. The small width means that the network corresponds to a thin 2D slice through the organic material oriented along the axes of the circular holes. That is, we consider flow perpendicular to the plane of the images in Figure 7.4. The objective is not to represent the actual connectivity of the voids, but to capture the influence of adsorbed layers and slip in a connected collection of throat sizes. When the throat sizes are distributed randomly on the network, the gas permeability of the network is 93 nD at lab condition (i.e. without adsorbed layer; the calculation accounts only for slip in each throat, using Equations (7.9) and (7.3) (high Knudsen flow models) to relate flow in each throat to pressure gradient along that throat). The network permeability is a plausible overestimate of the measured value as the network represents only the organic portion of the shale. The organic matter accounts for 10% of the core volume, so prorating the network contribution accordingly would yield an estimate of 9 nD which is typical for the shale (Billiotte et al., 2008).

A schematic of the network model is shown in Figure 7.10. The schematic indicates that the overall interactions of the throats, connected to each other in the network, control the flow properties. In the network model, we account for both the effects of adsorbed layer and gas slippage of the pore throat to predict the dependency of the flow properties on the pressure.

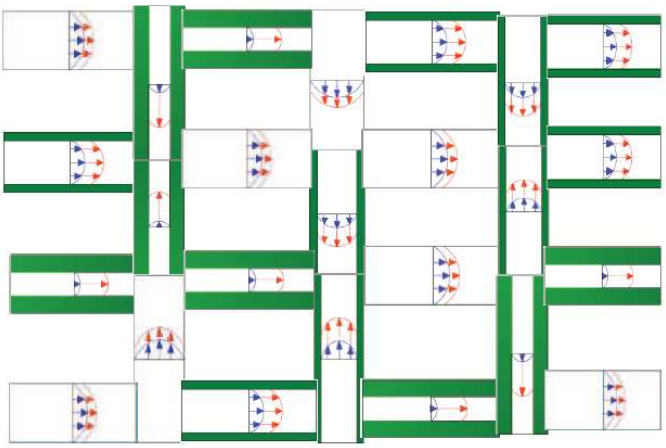

Figure 7.10: A schematic of the network model built based on mercury intrusion capillary pressure. This indicates we take into account both the effects of adsorbed layer (shown by green color) and slippage (shown by red arrows relative to blue arrows) for each pore throat.

7.5.1. Effect of laboratory conditions vs. field conditions on gas permeability

First, we evaluate the gas permeability at in-situ conditions by considering the influence of adsorbed layer on flow through each conduit in the network. To compute the gas conductance at in-situ condition, we calculate the liquid conductance with no-slip boundary condition based on the cross sectional area depending on the thickness of adsorbed layer. The gas conductance of each throat is then computed from the liquid conductance.

The ratio of network permeabilities at lab to in-situ conditions is presented in Figure 7.11. The results show that the measurements made at the lab condition would overestimate the permeability by a factor of 4 at P = 28 MPa, i.e. at the start of production. This factor is almost equal to the ratio of lab to in-situ permeabilities for a single tube of 6 nm (cf. Figure 7.8), which has the largest fraction of pore throat sizes as deduced from mercury intrusion data shown in Figure 7.2. This means that the throats whose characteristic sizes constitute the largest population dominate the flow behavior.

The overestimation would be even larger if the prediction were based on lab measurements at ambient pressure and temperature. This is because of enhancement in slippage occurring at low pressures. The ratio reaches unity at a slightly larger pressure than 5 MPa because the field temperature (360 K) is greater than the lab temperature (300 K) and because the gas for the lab measurement is N_2 and not CH_4. The difference in temperatures makes *Kn* slightly larger at the lab condition, but for a given pressure, temperature, and throat size, the properties of N_2 yield smaller *Kn* than for CH_4. Thus, smaller slippage occurs for N_2 than CH_4 because of smaller *Kn*, resulting in a smaller permeability. Thus, the gas permeability of the network model exposed to CH_4 at a slightly larger pressure than 5 MPa at field condition equals the N_2 permeability at the lab condition.

The ratio of lab to in-situ permeabilities decreases as the pressure decreases. This is because of the opposing effects of adsorbed layer and slippage at different pressures. To provide a quick tool for estimating the in-situ permeability from the lab measurement, we fit a curve to the results in Figure 7.11. The nonlinear regression model indicates the coefficient of regression is 0.99. Therefore, the in-situ gas permeability can be estimated from lab measurement using the following equation:

$$\frac{k_{g,lab}}{k_{g,in-situ}} = 0.001P^2 + 0.0898P + 0.783 \tag{7.12}$$

where $k_{g,in\text{-}situ}$ is the gas permeability at in-situ condition, $k_{g,lab}$ the gas permeability at lab condition (300 K, 5 MPa), and *P* gas pressure in MPa.

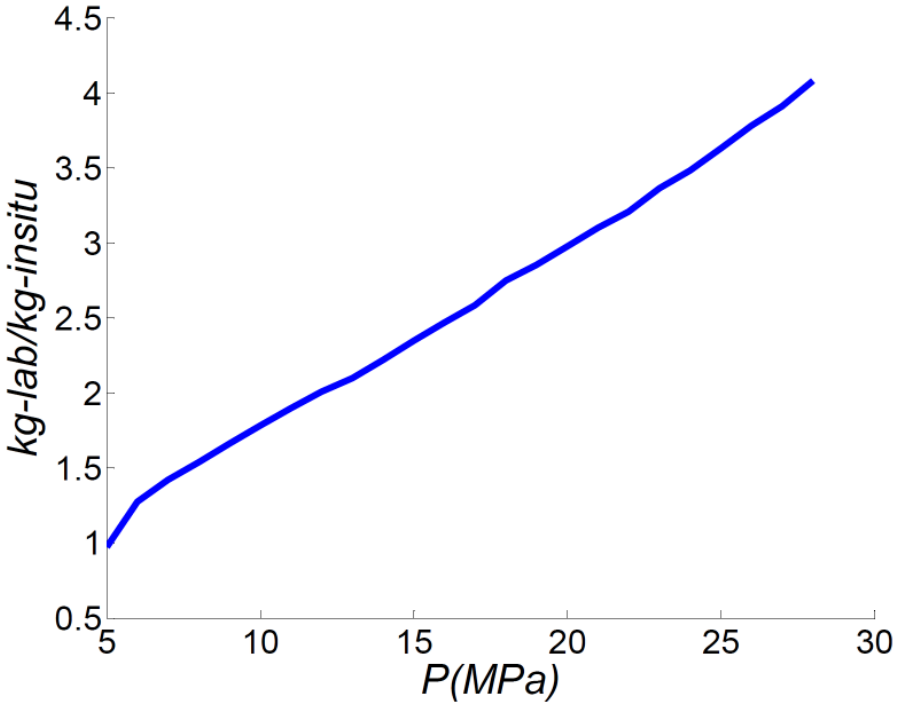

Figure 7.11: The ratio of gas permeability with slippage and without adsorbed layer (lab condition: T = 300 K, P = 5 MPa) to gas permeability with adsorbed layer and slippage (field condition: T = 360 K, P from x-axis) obtained from network of cylindrical throats having size distribution from Figure 7.2.

We should be aware of the differences between the Klinkenberg's correction and what we proposed here in Figure 7.11. In the Klinkenberg, the correction only accounts for the slip flow regime. However, we adopt both slip and transition models as they are appropriate flow regimes arise in nanoscale throats. Further, we have taken into account the effect of the adsorbed layer of gas on the gas permeability which was not included in the Klinkenberg's correction.

7.5.2. Effect of field conditions during production on gas permeability

Finally, we investigate the effect of declining field pressure on the gas permeability using the network model. In this regard, we calculate the ratio of the field permeability at low pressures ($k_{g2,in\text{-}situ}$) to its value at the start of production ($k_{g1,in\text{-}situ}$).

The initial field pressure is presumed to be 28 MPa. We take into account the effect of adsorbed layer depending on the pressure. In addition, we account for the effect of pressure on slippage. The ratio of the gas permeabilities are presented in Figure 7.12. The network modeling suggests that the shale permeability at the start of production is significantly smaller than during late production. The adsorbed layer is the reason for this effect. Furthermore, the dependency of the permeability on the pressure is nonlinear. Hence, the gas permeability of shale is highly dependent on the pressure unlike the conventional reservoir. This has major implications in reservoir simulations and ultimate recovery estimation models.

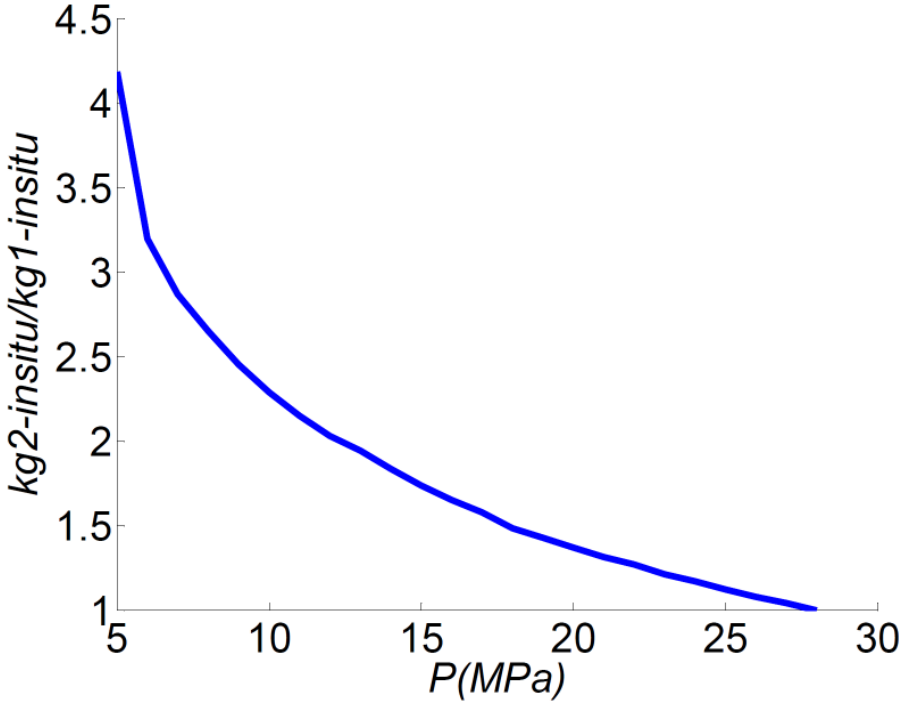

Figure 7.12: The ratio of gas permeability at pressures P_2 below initial reservoir pressure, k_{g,P_2}, to gas permeability at initial pressure (P = 28MPa), k_{g,P_1}, increases as production continues and pressure declines accordingly. The ratio is calculated from network of cylindrical throats having size distribution shown in Figure 7.2.

The significant permeability increase over the production life provides an explanation for the "long tail" behavior which is usually observed in shale gas reservoirs (Baihly et al., 2010). The long-tail production refers to the field data in which the production rate drops significantly at early times and lasts at low rate for a long period. An alternative explanation for the long tail behavior familiar from conventional reservoirs is that the reservoir is heterogeneous. Layered formations can give sustained lower rates late in the life of a well (Walsh and Lake, 2003). Determining whether such heterogeneity exists in shale gas reservoirs is beyond the scope of this work.

7.6. Validation against laboratory data

Figures 7.11 and 7.12 summarize the main implications of the theory. Figure 7.11 estimates gas permeability at the in-situ condition from the laboratory measurement and Figure 7.12 predicts the enhancement of the gas permeability during production. Two sets of experiments are required to validate these implications. The first set needs comparison of the measurements with N_2 at laboratory condition and CH_4 at reservoir condition. For the second set, we have to analyze the dependency of rock resistance against gas flow on the pore pressure when the moving fluid is methane. The test with methane should be run at the reservoir temperature and pressures to represent the in-situ conditions. Our model predicts that the effect of the adsorbed layer becomes more important as the organic content of shale increases. The organic-rich region has more tendencies to adsorb methane to its pore wall and this has to be considered when choosing the core samples.

Data across the range of conditions of Figures 7.11-12 for rocks with different organic content are not currently available. However, measurements of CH_4 transport reported on a particular shale at pressures below 7 MPa (Letham, 2011) let us partially test the effect of slippage. The experimental data were measured with methane for a

sample whose permeability at 5 MPa and 300 K is 390 nD. The effective stress was kept constant in the laboratory measurements (Letham, 2011), that is, the confining stress was lowered to yield the same effective stress at a lower pore pressure. The porosity of the laboratory sample was reported to be 13%. The porosity of our original sample is 10%, which is slightly different from the laboratory sample. To compensate for these differences, we increase the pore throat sizes of our original network model, whose permeability is 9 nD at 5MPa and 300 K, by a factor of 6.58 ($\sqrt{\frac{390}{9}} = 6.58$). We also increase the width of the network by a factor of 43.3 ($=6.58^2$) to keep the porosity of the network model unaffected by the change in the pore size distribution. Using the modified model, we compute gas permeabilities for a range of small pressures (between 1 and 6 MPa) and 300 K. Since the effective stress was kept constant during laboratory measurements, we do not change the modified pore throat size distribution with pore pressure. (In the field effective stress increases with reservoir depletion, and the effect on pore throat size distribution, which is not included in the model presented here, would diminish the slippage effect in Figure 7.13). Figure 7.13 plots these gas permeabilities normalized by the nominal liquid permeability at laboratory condition. Similar to every calculation done for the laboratory condition through this study, the gas flow here is with slippage and without adsorbed layer and the liquid flow is without slippage and without adsorbed layer. However, unlike the laboratory condition we defined in which pressure is 5 MPa, we change the pressure to investigate its influence on gas permeability, which is because of slippage. The liquid permeability for the laboratory data is 390 nD estimated by extrapolating the measured gas permeability to large pressure. Figure 7.13 shows that the model slightly underestimates the normalized gas permeability, the maximum difference with laboratory measurement being only 6%. This indicates that the slippage

model provides a good estimate for the effect of pressure on gas permeability at moderate pressures.

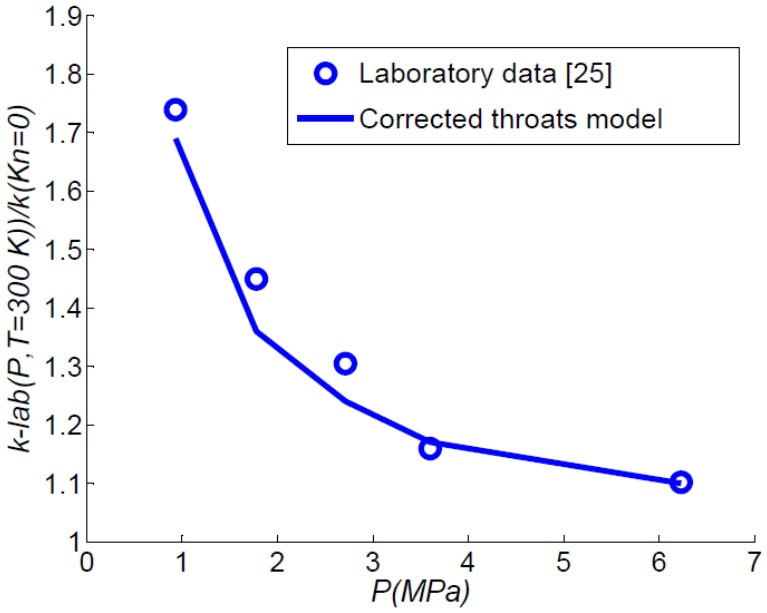

Figure 7.13: The ratio of gas permeability without adsorbed layer and with slippage (*k-lab*(*P*, *T*=300 K)) to the liquid permeability without adsorbed layer and without slippage (*k*(*Kn*=0)) is obtained from a network of conduits and compared with the laboratory measurements (Letham, 2011). The effective stress is constant and hence, the pore pressure change does not affect pore throat size distribution. Gas permeability increases with lowering pressure because of slippage unlike the liquid permeability which is constant. The flowing gas is methane.

7.7. Conclusions

Pore throats of shale are mostly narrower than 10 nm and are inside organic material on which CH_4 adsorbs. As a result, the gas permeability of these rocks is significantly affected by adsorbed gas and by slip of flowing gas on the pore walls (or on layers of molecules adsorbed on the walls). The adsorbed layer does not play an

important role in conventional rocks as the pore throats are much wider, nor is the gas volume desorbed from the organic material significant in conventional reservoirs. To better understand gas flow behavior through shale, we evaluated these effects in individual conduits of cylindrical cross-section and in simple networks of such conduits. The effect of adsorbed layer was treated as purely geometric: the cross-section open to flow was reduced by the thickness of the adsorbed layer, which was assumed to vary linearly with pressure. The effect of slip was accounted for by applying the model appropriate to the flow regime, according to Knudsen number (*Kn*). The latter depends on pressure, temperature, and conduit diameter. For the slip flow regime, the first-order slip model was judged more suitable than the dusty-gas model for the shale gas application.

At large pressures such as typical initial shale gas reservoir pressures, the effect of the adsorbed layer dominates the effect of slip on gas phase permeability. Slip dominates at smaller pressures typical of those after longer periods of production. Consequently, the reservoir matrix permeability is predicted to increase significantly over the life of a well, by a factor of 4.5, as production continues and pressure declines. The models predict that the typical conditions for laboratory measurements of permeability cause those values to overestimate field permeability by as much as a factor of 4. The model results are captured in simple analytical expressions that allow convenient estimation of these effects.

For complete validation of the proposed model, laboratory measurements at elevated pressures, in the order of 28 MPa, and reservoir temperature made with CH_4 are needed. Experimental data at such conditions, for which the adsorbed layer is expected to have the dominant effect, are not available. Comparing model predictions with the laboratory data at lower pressures (< 7MPa) and constant effective stress permits evaluating the importance of slippage. When normalized by the nominal absolute

permeability of the network (i.e. the value when both slip and adsorbed layers are negligible), the predicted trend agrees well with the measurements. The maximum difference between the predicted normalized gas permeability and measured value is 6%. This means that our adapted network model provides a reasonable basis for understanding the effect of gas pressure on matrix permeability of shale gas reservoir.

Chapter 8: Concluding remarks and future works recommendations

8.1. Concluding remarks

8.1.1. Tight gas sandstone

The objective of this study in tight gas sandstone was to develop a new pore structure model to capture the two-phase displacements, notably mercury invasion/withdrawal (as obtained in conventional mercury intrusion capillary pressure measurement in evacuated samples, followed by mercury withdrawal), and gas drainage of brine (as obtained in conventional porous plate experiments of initially brine-saturated samples).

We have analyzed the laboratory measurements of mercury intrusion (drainage), withdrawal (imbibition), porous plate on a set of 15 samples of tight gas sandstones from the Western US. For this purpose, we have developed a multiscale model to analyze macroporosity (intergranular void space) and microporosity (intragranular void space) and their interactions. The multiscale model embraces conventional network model and tree-like pore structure to mimic the intergranular and intragranular void spaces, respectively. The tree-like pore structure is proposed in this study for the first time.

The porous plate data of the drainage experiment prove to exhibit a strong signature of the amount of intergranular voids in a sample. Applying the multiscale model to such data enables a classification of the void space of rocks into macro-dominant (large macroporosity fraction), intermediate (combination of macro and microporosity), and micro-dominant (large microporosity fraction). Each class has different imbibition behavior and hence different expected gas recoveries. Similarly, the mercury withdrawal test shows different results for each pore type identified by the porous plate test, and hence, it independently confirms the existence of different

connectivities of void spaces. Using mercury withdrawal data along with our pore structure classification allows estimating the characteristic residual saturation for each structure. For a set of 35 samples of tight gas sandstones from the Western US and 9 from other places (Cluff and Webb, 2009), the ultimate recovery is estimated to be between 14% to 83% of the initial hydrocarbon saturation depending on the ratio of microporosity to total porosity and initial gas saturation. The recovery increases as the fraction of tree-like microporosity increases and also improves with an increase in initial hydrocarbon saturation. The classification also predicts different electrical resistivity responses for the classified pore structures that are consistent with the measured results. For the set of 15 samples from Western US, the averages (arithmetic mean) of the cementation exponents of the macro-dominant, intermediate, and micro-dominant are 1.8, 1.79, and 1.48, respectively. For these samples, the averages (arithmetic mean) of the saturation exponents of the macro-dominant, intermediate, and micro-dominant are 1.58, 1.50, and 1.32, respectively.

We have used field data (repeat PLT logs on a single well in a tight gas sandstone) to test our multiscale model. For this, we classified the pore structure using laboratory measurements like permeability and mercury withdrawal. We observe that the production rate per unit thickness of the macro-dominant interval is the largest initially but it becomes the smallest at a later time during the production because it has the fastest reduction rate in the production. The largest initial production rate is because of the largest permeability typical of macro-dominant rock, the fastest reduction in the production rate (largest decline ratio) is a consequence of inferior recovery (largest residual saturation) from macro-dominant rock. This means that the available field data are consistent with the model prediction, and this method of classifying tight gas sandstones by pore type should be tested as larger sets of data become available.

We extrapolated the production rates of the layers of the tight gas reservoir obtained from PLT using the tank model and integrated over time to compare the cumulative production of each layer. The projected cumulative production per unit thickness indicates that the hydrocarbon recovery of the micro-dominant interval is the largest, and this agrees with our hypothesis of having better producibility with in increase in the microporosity fraction. Knowing that micro-dominant pore space typically has smallest permeability of the three pore types and therefore that micro-dominant intervals tend to have the lowest initial production (IP) rates within a well, we conclude that initial production (IP) alone is not an appropriate tool for estimating EUR. This highlights the importance of having a better understanding from pore structure of unconventional rocks which could be true for shale gas reservoirs as well.

8.1.2. Shale gas

The main goal of this dissertation with regard to the properties of gas shale was to analyze the pore connectivity. We also sought to evaluate the effects of the adsorbed layer of gas and of gas slippage on the single-phase gas permeability.

To analyze the pore connectivity, we studied the mercury intrusion capillary pressure (MICP) data of the shale and proposed two pore structure models, i.e. tree-like model and nooks and crannies (NC). The proposed models adopt different pore throat geometries and connectivities. The void space of the tree-like structure takes circular tubes to model the pore throats that are connected in an acyclic pattern. In the tree-like model, there are multiplying branches with ever smaller throats. On the other hand, the NC model assumes that the void space comprises microcrack-like (large-aspect-ratio) throats that are connected through the rock similar to the bundle-of-tubes model.

We used both connectivity models to predict the single-phase gas permeability without slippage and without adsorbed layer of gas from the MICP data. The NC model predicts that the permeability is 106 nD whereas for the tree-like pore model it is between 15-27 nD. These are both in the acceptable range of permeability (< 100 nD, Sakhaee-Pour and Bryant, 2012).

The NC model requires extremely large-aspect-ratio throats to capture the MICP data. The throat length is approximately 30 micron for a 22-nm wide microcrack-like throat if we assume that the throat size is mono-size. However, it is very unlikely that such a large-aspect ratio throat remains open at in-situ condition in the presence of a confining stress. Thus, we judged that the NC model is not representative of the shale void space and the pore connectivity of the shale is more similar to the tree-like structure.

To better understand the effects of adsorbed layer of gas and of gas slippage on the shale permeability, we first evaluated these effects in individual conduits of cylindrical cross-section and in simple networks of such conduits. The effect of adsorbed layer was treated as purely geometric: the cross-section open to flow was reduced by the thickness of the adsorbed layer, which was assumed to vary linearly with pressure. The effect of slip was accounted for by applying the model appropriate to the flow regime, according to Knudsen number (*Kn*). The latter depends on pressure, temperature, and conduit diameter. For the slip flow regime, the first-order slip model was judged more suitable than the dusty-gas model for the shale gas application.

At large pressures such as typical initial shale gas reservoir pressures, the effect of the adsorbed layer dominates the effect of slip on gas phase permeability. Slip dominates at smaller pressures typical of those after longer periods of production. Adsorbed layer reduces the conductance of the shale pore throat by a factor of (1.1–7.2) while its slippage enhances the conductance by a factor of (1.2–2.9). Implementing both effects,

our adapted network model predicts that the matrix permeability increases significantly over the life of a well, by a factor of 4.5 for a Barnett shale sample, as production continues and pressure declines. The adapted network model is built based on the pore size distribution obtained from MICP data of the Barnett shale sample. The model also predicts that the typical conditions for laboratory measurements of permeability cause those values to overestimate field permeability by as much as a factor of 4. The model results are captured in simple analytical expressions that allow convenient estimation of these effects.

For complete validation of the proposed model, laboratory measurements at elevated pressures, in the order of 28 MPa, and reservoir temperature made with CH_4 are needed. Experimental data at such conditions, for which the adsorbed layer is expected to have the dominant effect, are not available. Comparing model predictions with laboratory data reported in literature at lower pressures (< 7MPa) and constant effective stress permits evaluating the importance of slippage. When normalized by the nominal absolute permeability of the network (i.e. the value when both slip and adsorbed layers are negligible), the predicted trend agrees well with the measurements. The maximum difference between the predicted normalized gas permeability and measured value is 6%. This means that our adapted network model provides a reasonable basis for understanding the effect of gas pressure on matrix permeability of shale gas reservoir.

8.2. Future work recommendations

8.2.1. Tight gas sandstone

The gas production data of a Western US reservoir were available from production logging tool (PLT) logs at two different times. To further test the notion of pore structure classification and its implication on the ultimate recovery, we propose that

the operators consider acquiring more production data at later times of productions. This allows further assessments of the performance of the tight gas reservoir.

We assigned the pore structure of the producing interval in this dissertation from the core measurements. In practice, these measurements are not always available. Thus, the next step is to assign the pore structure of the producing interval from other logging tools like resistivity logs. The measurements are obtained more often in practice.

8.2.2. Shale gas

We learned a lot regarding the pore structure of the tight gas sandstone by analyzing the porous plate results. However, such experiments using samples of gas shale are not available in the literature. Thus, we propose that researchers obtain those data for further investigations of the shale pore structure.

We proposed the adapted network modeling approach to predict the effects of adsorbed layer of gas and gas slippage at the pore walls on the single-phase gas permeability. Those effects are highly dependent on the gas pressure. However, the gas permeability measurements at elevated pore pressures (~ 4000 psi) are not currently available. Hence, the next step would be to acquire the permeability measurements at those elevated pore pressures and compare the results with what the adapted network modeling approach predicts.

We analyzed the gas flow behavior assuming that the flow is single-phase. However, in reality, shale reservoirs produce a significant volume of water. Therefore, the subsequent step is to study the two-phase flow properties of shale gas reservoirs. This entails both theoretical and experimental studies.

We interpreted the topology of the shale void space from MICP measurements. The capillary pressure increases up to 60000 psi in these measurements to invade the pore throats that are smaller than 10 nm, which is a typical range for the shale (Sakhaee-Pour and Bryant, 2012). This large capillary pressure could alter the pore structure and hence, the interpreted topology might not be representative of an intact rock. Hence, we recommend that the researchers analyze other pore size distribution measurements such as adsorption/desorption and contrast the results with MICP data.

We observed many microcrack-like pore throats in the SEM images of the shale. These throats are more probably closed at in-situ condition in the presence of a confining stress. Hence, it would be valuable to measure and analyze the mercury intrusion and withdrawal capillary pressures of confined shale samples. This analysis will help us to know pore throats with which characteristic sizes are open under the confined boundary condition and hence, we will interpret the existing SEM images more intelligibly. The SEM images are obtained without confining stress and they likely show some throats that are probably closed at in-situ condition. The study of the confined shale samples will also allow us to gain a better understanding of the connected network of the pores at the in-situ condition.

Appendix A: Non-continuum flow models for slip flow regime

A.1. First order slip model

The velocity profile in the slip flow regime for a cylindrical conduit is obtained by adding a correction term to the solution of the Navier-Stokes equation after applying Newtonian fluid assumption with no-slip boundary condition (Roy et al., 2003):

$$u_s = u_{no-slip} + u_{correction} \tag{A.1}$$

where u_s is the velocity profile in the slip flow regime, $u_{no\text{-}slip}$ the no-slip velocity of the Newtonian fluid, and $u_{correction}$ the correction term to implement the effect of slippage. The correction term is constant independent of location. The slip velocity profile can also be expressed in a non-dimensional form as:

$$U_s = U_{no-slip} + U_{correction} \tag{A.2}$$

where the non-dimensional no-slip velocity is defined as follows:

$$U_{no-slip} = 1 - (\frac{r}{R})^2 = 1 - x^2 \tag{A.3}$$

where R is the radius of tube, r distance from the center tube, and x the normalized radial distance from the center of tube which is equal to unity at the wall. To include the effect of molecule-wall collisions, the first order slip boundary condition is imposed as (Karniadakis et al., 2003):

$$U_s\big|_w = \frac{2-\sigma_v}{\sigma_v} \frac{\partial U_s}{\partial n}\bigg|_w Kn \tag{A.4}$$

where n is outward (unit) vector which is normal to the tube wall and σ_v the tangential momentum accommodation coefficient. The tangential momentum accommodation is calculated by measuring the gas flow rate at the slip flow regime and is close to 0.9 (Karniadakis et al., 2003).

The first order slip boundary condition is applied to derive the non-dimensional velocity profile (see Equation (A.2)) (Karniadakis et al., 2003):

$$\left.\frac{\partial U_s}{\partial n}\right|_w = \left.\left(\frac{\partial U_{no-slip}}{\partial n} + \frac{\partial U_{correction}}{\partial n}\right)\right|_w = \left.\frac{\partial U_{no-slip}}{\partial n}\right|_w = -(-2x)\big|_{x=1} = 2 \tag{A.5}$$

The minus sign is because of the direction of the normal vector. The correction term is constant and thus its gradient vanishes. Therefore, Equation (A.4) simplifies to:

$$\frac{2-\sigma_v}{\sigma_v}\left.\frac{\partial U_s}{\partial n}\right|_w Kn = 2\left(\frac{2-\sigma_v}{\sigma_v}\right)Kn \tag{A.6}$$

Thus, we can express the non-dimensional velocity profile based on Equations (A.2) and (A.3) as written in below (Karniadakis et al., 2003):

$$U_s = 1 - x^2 + 2\left(\frac{2-\sigma_v}{\sigma_v}\right)Kn \tag{A.7}$$

To cast this profile in terms of permeability, we obtain the flow rate as:

$$Q = \int u_s(r)2\pi r dr = \alpha\int_0^1 \left(1 - x^2 + 2\left(\frac{2-\sigma_v}{\sigma_v}\right)Kn\right)x dx$$

$$\overline{Q} = \frac{Q}{\alpha}\int_0^1 \left(1 - x^2 + 2\left(\frac{2-\sigma_v}{\sigma_v}\right)Kn\right)x dx = \frac{1}{4} + \left(\frac{2-\sigma_v}{\sigma_v}\right)Kn \tag{A.8}$$

where Q is the flow rate, σ_v a characteristic flow rate, and $\overline{Q}$ the non-dimensional flow rate. The first term in the RHS represents the no-slip flow rate and the second term is the enhancement because of slippage. Therefore, the effect of slip on permeability can be readily measured by dividing $\overline{Q}(Kn)$ by $\overline{Q}(Kn{=}0)$:

$$\frac{k_g}{k_l} = \frac{\frac{1}{4} + \left(\frac{2-\sigma_v}{\sigma_v}\right)Kn}{\frac{1}{4}} = 1 + 4\left(\frac{2-\sigma_v}{\sigma_v}\right)Kn \tag{A.9}$$

Here, k_g is the permeability of the conduit to gas phase, and k_l is the permeability of the same conduit when the no-slip boundary condition applies. The latter condition usually holds when a liquid fills the conduit, hence the choice of subscript "*l*". After implementing σ_v = 0.9, we obtain the enhancement of apparent permeability, called [illegible] in chapter 7 text (cf. Equation (7.3)), to be equal to 5.

A.2. Dusty gas model (DGM) in terms of Knudsen number

The apparent permeability of the conduit based on dusty gas model (DGM) is calculated as:

$$\frac{k_g}{k_l} = (1 + \frac{D_{Kn}\mu}{k_l p}) = 1 + \frac{b}{p} \tag{A.10}$$

The second term on the RHS can be simplified after substituting the Knudsen diffusivity coefficient in terms of pertinent parameter using Eq. (A.11). We also use the Hagen-Poiseuille model for permeability term as follows:

$$\frac{b}{p} = \frac{D_{Kn}\mu}{k_l p} = \frac{\frac{d}{3}\sqrt{\frac{8RT}{\pi m}} \times \mu}{\frac{d^2}{32} \times p} = \frac{32}{3}\frac{1}{d}\frac{\sqrt{\frac{8RT}{\pi m}} \times \mu}{p} = \frac{64}{3}\frac{1}{d}\frac{\sqrt{\frac{2RT}{\pi m}} \times \mu}{p} \tag{A.11}$$

Here, we implement the ideal gas assumption ($P = \rho\frac{R}{m}T = \rho\bar{R}T$) to express the pressure in terms of density which yields the results in terms of *Kn*:

$$\frac{b}{p} = \frac{64}{3}\frac{1}{d}\frac{\sqrt{\frac{2RT}{\pi m}} \times \mu}{\rho\frac{R}{m}T} = \frac{64}{3}\frac{\mu}{\rho d}\sqrt{\frac{2m}{\pi RT}} = \frac{128}{3\pi}\frac{\mu}{\rho d}\sqrt{\frac{\pi}{2\bar{R}T}} = 13.58Kn \tag{A.12}$$

Bibliography

Adesida , A.G., Akkutlu, I.Y., Resasco , D.E., and Rai, C.S., ”Characterization of Barnett Shale Kerogen Pore Size Distribution using DFT Analysis and Grand Canonical Monte Carlo Simulations”, SPE Paper 147397, presented at SPE Annual Technical Conference and Exhibition, Denver, Colorado, USA, Oct. 30-Nov. 2, 2011.

Al-Sayari, S.S., “The Influence of Wettability and Carbon Dioxide Injection on Hydrocarbon Recovery”, PhD dissertation, Imperial College, London, UK, (2009).

Ambrose, R.J., Hartman, R.C., Diaz-Campos, M., Akkutlu, Y., and Sondergeld, C.H.,” New Pore-scale Considerations for Shale Gas in Place Calculations”, SPE Paper 131772, presented at Unconventional Gas Conference, Pittsburgh, Pennsylvania, USA, Feb. 23-25, (2010).

Bazin, B., Bekri , S., Vizika, O., Herzhaft, B., and Aubry, E., “Fracturing in Tight Gas Reservoirs: Application of Special-Core-Analysis Methods To Investigate Formation-Damage Mechanisms”, SPE Journal, 15, 969-76, (2010).

Bahrami, H., Rezaee, M.R., Nazhat, D., Ostojic, J., Clennell, B., and Jamili, A., “Effect of Water Blocking Damage on Flow Efficiency and Productivity in Tight Gas Reservoirs”, SPE Paper 142283, presented at SPE Production and Operations Symposium, Mar. 27-29, Oklahoma City, Oklahoma, USA, 2011.

Baihly, J., Altman, R., Malpani, R., and Luo, F., “Shale Gas Production Decline Trend Comparison over Time and Basins” SPE Paper 135555, presented at ATCE, Florence, Italy, Sep. 19-22, 2010.

Beckner, B.L., Hutfilz, J.M., Ray, M.B., Tomich, J.F., “EM: New Reservoir Simulation System”, SPE Paper 68116, presented at SPE Middle East Oil Show, Bahrain, Mar.17-20, 2001.

Behseresht, J., Bryant, S.L., and Sepehrnoori, K., “Infinite-Acting Physically Representative Networks for Capillarity-Controlled Displacements”, SPE Journal, 14(4), 568-78, (2009).

Bennett, C.O., and Myers, J.E., ”Momentum, Heat, and Mass Transfer”, New York: McGraw-Hill, (1962).

Berkowitz, B., and Balberg, B., “Percolation Theory and Its Application to Groundwater Hydrology,” Water Resources Research, 29, 775-94, (1993).

Billiotte, J., Yang, D., and Su, K., “Experimental Study on Gas Permeability of Mudstones”, Physics and Chemistry of the Earth, Parts A/B/C, 33, 231-6, (2008).

Blatt, H. and Tracy, R.J., “Petrology: Igneous, Sedimentary and Metamorphic”, New York: W.H. Freeman and Company, (1996).

Brace, W.F., and Martin, R.J., “A Test of the Law of Effective Stress for Crystalline Rocks of Low Porosity”, International Journal Rock Mechanics Mining Science, 5, 415-46, (1968).

Brooks, R.H., and Corey, A.T., "Properties of Porous Media Affecting Fluid Flow", Journal Irrigation Drainage Division, 6, 61-88, (1966).

Bryant, S.L., Mellor, D., and Cade, C., “Physically Representative Network Models of Transport in Porous Media”, American Institute of Chemical Engineering Journal, 39(3), 387-96, (1993).

Byrnes, A.P., and Castle, J.W., “Comparison of Core Petrophysical Properties Between Low-Permeability Sandstone Reservoirs: Eastern U.S. Medina Group and Western U.S. Mesaverde Group and Frontier Formation “ SPE Paper 60304, presented at SPE Rocky Mountain Regional/Low-Permeability Reservoirs Symposium and Exhibition, Denver, Colorado, USA, Mar. 12-15, 2000.

Byrnes, A.P., “Permeability, Capillary Pressure, and Relative Permeability Properties in Low-permeability Reservoirs and the Influence of Thin, High-permeability Beds on Production: in M.G. Bishop, S.P. Cumella, J.W. Robinson, and M.R. Silverman (eds.), Gas in Low Permeability Reservoirs of the Rocky Mountain Region”, Rocky Mountain Association of Geologists Guidebook CD, 69-108, 2005.

Cargill, G.S.,”Radial Distribution Functions and Microgeometry of Dense Random Packings of Hard Spheres”, AIP Conference Proceedings, 107 (1), 20-36, (1984).

Cipolla , C.L. , Lolon, E.P., Erdle, J.C., and Rubin, B.,”Reservoir Modeling in Shale-Gas Reservoirs”, SPE Reservoir Evaluation and Engineering, 13, 638-53, (2010).

Comisky, J.T., Newsham, K.E., Rushing, J.A., and Blasingame, T.A., “A Comparative Study of Capillary-Pressure-Based Empirical Models for Estimating Absolute Permeability in Tight Gas Sands”, SPE Paper 110050, presented at SPE Annual Technical Conference and Exhibition, Anaheim, California, USA, Nov. 11-14, 2007.

Cluff, R.M., and Webb, J.C., "Analysis of Critical Permeability, Capillary Pressure and Electrical Properties for Mesaverde Tight Gas Sandstones from Western U.S. Basins", DOE Award No.: DE-FC26-05NT42660, (2009).

Curtis, M.E., Ambrose, R.J., Sondergeld, C.H., Rai, C.S., "Structural Characterization of Gas Shales on the Micro- and Nano-Scales", SPE Paper 137693, presented at Canadian Unconventional Resources and International Petroleum Conference, Calgary, Alberta, Canada, Oct. 19-21, 2010.

Derjaguin, B.V., and Churaev, N. V., "Structural component of disjoining pressure", Journal of Colloids and Interface Science, 49, 249-255, (1974).

Dewers, T.A., Heath, J., Ewy, R., and Duranti, L.," Three-dimensional Pore Networks and Transport Properties of a Shale Gas Formation Determined from Focused Ion Beam Serial Imaging", International Journal of Oil, Gas and Coal Technology, 5(2/3), 229-48, (2012).

Dvorkin, J.K., Nur, A., and Mese, A., "Real Time Monitoring of Permeability, Elastic Moduli and Strength in Sands and Shales Using Digital Rock Physics ", SPE Paper 82246, presented at SPE European Formation Damage Conference, Hague, Netherlands, May 13-14, 2003.

Eichhubl, P. "Characterization and Modeling of Pore-scale Flow Pathways in Tight Gas Sandstone, Piceance Basin, Colorado", invited talk presented at The Geology of Unconventional Gas Plays, The Geological Society, London, UK, Oct. 6, 2010.

Fathi, E., and Akkutlu, Y.," Lattice Boltzmann Method for Simulation of Shale Gas Transport in Kerogen", SPE Paper 146821, presented at SPE Annual Technical Conference and Exhibition, Denver, Colorado, USA, Oct. 30-Nov.2, 2011.

Fatt, I., "The Network Model of Porous Media, I. Capillary Pressure Characteristics", AIME Petroleum Transactions, 207, 144-81, (1956).

Finney, J., "Random Packings and the Structure of Simple Liquids. I. The Geometry of Random Close Packing", Proceedings of the Royal Society of London. Series A. Mathematical, Physical and Engineering Sciences, 319, 479-493, (1970).

Gladkikh, M., and Bryant, S., "Prediction of Imbibition in Unconsolidated Granular Materials", Journal of Colloid and Interface Science, 288(2), 526-39, (2005).

Graham, T., "On the Motion of Gases. Reprinted in Chemical and Physical researchers", Edinburgh: Edinburgh University, UK, (1876).

Hayes, J.B., 1991, “Porosity Evolution of Sandstones Related to Vitrinite Reflectance“, Organic Geochemistry, 17, 117-29, (1991).

Heath, J.E., Dewers, T.A., McPherson, B., Petrusak, R., and Chidsey, T.C., “Pore Networks in Continental and Marine Mudstones: Characteristics and Controls on Sealing Behavior”, Geosphere, 7, 429-54, (2011).

Holditch, S.A., “Tight Gas Sands”, Journal of Petroleum Technology, 58, 86-93, (2006).

Jones, F.O., and Owens, W.W., “A Laboratory Study of Low-permeability Gas Sands”, Journal of Petroleum Technology, 32, 1631-40, (1980).

Jones, S.C., “A Technique for Faster Pulse-Decay Permeability Measurements in Tight Rocks”, SPE Formation Evaluation”, 12, 19-26, (1997).

Kamath, J., “Evaluation of Accuracy of Estimating Air Permeability From Mercury-Injection Data”, SPE Formation Evaluation, 7, 304-10, (1992).

Karniadakis, G., Beskok, A., and Aluru, N. “Microflows and Nanoflows: Fundamentals and Simulation”, New York: Springer, (2005).

Klinkenberg, L.J., “The Permeability of Porous Media to Liquids and Gases”, SPE Paper 41-200, presented at Drilling and Production Practice, (1941).

Knudsen, M. “The Laws of Molecular and Viscous Flow of Gases Through Tubes”, Ann. Physik, 28, 75-177, (1909).

Lake, Larry W. “Enhanced Oil Recovery”, Englewood Cliffs, N.J.: Prentice Hall, (2010).

Larson, R. G., and Morrow, N. R., “Effects of Sample Size on Capillary pressure in porous media”, Powder Technology. 30, 123-138, (1981).

Law, B.E., and Dickenson, W.W., “Conceptual Model for Origin of Abnormally Pressured Gas Accumulations in Low Permeability Reservoirs”, AAPG Bulletin, 69, 1295-1304, (1985).

Leahy-Dios, A., Das, M., Agarwal, A., and Kaminsky, R.D., “Modeling of Transport Phenomena and Multicomponent Sorption for Shale Gas and Coalbed Methane in an Unstructured Grid Simulator”, SPE Paper 147352, presented at SPE Annual Technical Conference and Exhibition, Oct. 30- Nov. 2, Denver, Colorado, USA, 2011.

Lee, D.S., Elsworth, D., Yasuhara, H., Weaver, J. and, Rickman, R., "Experiment and Modeling to Evaluate the Effects of Proppant-pack Diagenesis on Fracture Treatments", Journal of Petroleum Science and Engineering, 74, 67-76, (2010).

Letham, E.A., "Matrix Permeability Measurements of Gas Shales: Gas Slippage and Adsorption as Sources of Systematic Errors", BS Thesis, The University of British Columbia, Vancouver, Canada, (2011).

Liu, H., Lin, Z., and Seaton, N. A., "Analysis of Sorption Hysteresis in Mesoporous Solids Using a Pore Model Network Model", Journal of Colloid and Interface Science, 156 (2), 285-293, (1993).

Loucks, R.G., Reed, R.M., Ruppel, S.C., Jarvie, D.M.," Morphology, Genesis, and Distribution of Nanometer-scale Pores in Siliceous Mudstones of the Mississippian Barnett Shale", Journal of Sedimentary Research, 79, 848–861, (2009).

Luffel, D.L., Hopkins, C.W., Holditch, S.A., Schettler P.D., and Luffel, L., "Matrix Permeability Measurement of Gas Productive Shales", SPE Paper 26633, presented at SPE Annual Technical Conference and Exhibition, Houston, Texas, USA, Oct. 3-6, 1993.

Luffel, D.L., Howard, W.E., and Hunt, E.R., "Travis Peak Core Permeability and Porosity Relationships at Reservoir Stress", Society of Petroleum Engineers Formation Evaluation, 6(3), 310-19, (1991).

Mallon, A. and Swarbrick, R.E., "How Should Permeability Be Measured in Fine-grained Lithologies? Evidence From the Chalk", Geofluids, 8, 34-45, (2008).

Mason, E.A., and Malinauskas, A.P. "Gas Transport in Porous Media: The Dusty-Gas Model", Amsterdam; New York: Elsevier, (1983).

Mason, G., and Mellor, D.W.," Simulation of Drainage and Imbibition in a Ransom Packing of Equal Spheres", Journal of Colloid and Interface Science, 176, 214-225, (1995).

Masters, J.A., "Deep Basin Gas Trap, Western Canada", AAPG Bulletin, 63, 152-81, (1979).

Masters, J.A., "Lower Cretaceous Oil and Gas in Western Canada, in J. A. Masters, ed., Elmworth-Case Study of a Deep Basin Gas Field", AAPG Memoir, 38, 1-34, (1984).

Mendenhall, W., Reinmuth, J.E., and Beaver, R.," Statistics for Management and Economics". Boston; Massachusetts: PWS-Kent Publishing Company, (1989).

Michel, G.G., Sigal, R.F., Civan, F., and Devegowda, D.,"Parametric Investigation of Shale Gas Production Considering Nano-Scale Pore Size Distribution, Formation Factor, and Non-Darcy Flow Mechanisms", SPE Paper 147438, presented at SPE Annual Technical Conference and Exhibition, Denver, Colorado, USA, Oct. 30-Nov.2, 2011.

Mousavi, M.A., and Bryant, S.L., "Geometric Models of Porosity Reduction Mechanisms in Tight Gas Sands" SPE Paper 107963, presented at SPE Rocky Mountain Oil and Gas Technology Symposium, Denver, Colorado, USA, Apr. 16-18, 2007.

Mousavi, M. and Bryant, S.L., "Predicting the Effect of Diagenetic Alteration on Two-phase Flow Properties in Tight Gas Sands,", presented at American Association of Petroleum Geologists Southwest Section 2008 Convention, Abilene, Texas, USA, Feb. 24-27, 2008.

Mousavi, M.A., and Bryant, S.L., "Connectivity of Pore Space: the Primary Control on Two-phase Flow Properties of Tight Gas Sands", presented at AAPG Annual Convention and Exhibition, Denver, Colorado, USA, Jun. 7-10, 2009.

Mousavi, M.A., "Pore-scale Characterization and Modeling of Two-phase Flow in Tight Gas Sandstones", PhD Dissertation, The University of Texas at Austin, Austin, Texas, USA, (2010).

Nelson, P.H., "Pore Throat Sizes in Sandstones, Tight Sandstones, and Shales", AAPG Bulletin, 93, 329-40, (2009).

Olson, J.E., Laubach, S.E., and Eichhubl, P., "Estimating Natural Fracture Producibility in Tight Gas Sandstones: Coupling Diagenesis with Geomechanical Modeling", The Leading Edge, 29 (12), 1494-99, (2010).

Oren, P.E., Stig, B. and Arntzen, O.J., "Extending Predictive Capabilities to Network Models", SPE Journal, 3, 324-36, (1998).

Oren, P.E., and Stig, B., "Process Based Reconstruction of Sandstones and Prediction of Transport Properties", Transport in Porous Media, 46, 311-43, (2002).

Ostensen, R.W., "Microcrack Permeability in Tight Gas Sandstone", SPE Journal, 23, 919-27, (1983).

Passey, Q.R., Bohacs, K.M., Esch, W.L., Klimentidis, R., and Sinha, S., "From Oil-Prone Source Rock to Gas-Producing Shale Reservoir - Geologic and Petrophysical Characterization of Unconventional Shale Gas Reservoirs", SPE Paper 131350, presented at International Oil and Gas Conference, Beijing, China, Jun. 8-10, 2010.

Polczer, S., "Shale to Supply Half of North America's Gas", Calgary, Herald, Canada, Apr. 9, 2009.

Purcell, W.R., "Capillary Pressure - Their Measurements Using Mercury and the Calculation of Permeability Therefrom", AIME Petroleum Transactions, 186, 39-48, (1949).

Reinecke, S.A., and Sleep, B.E. "Knudsen Diffusion, Gas Permeability, and Water Content in an Unconsolidated Porous Medium", Water Resources Research 38, 1-16, (2002).

Rodriguez, E, "Grain-Scale Mechanisms of Particle Retention in Saturated and Unsaturated Granular Materials", PhD Dissertation, The University of Texas at Austin, Austin, Texas, USA, (2011).

Roy, S., Raju, R., Chuang, H.F., and Cruden, B.A., and Meyyappan, M., "Modeling Gas Flow Through Micro-channels and Nano-pores", Journal of Applied Physics, 93, 4870-9, (2003).

Sakhaee-Pour, A., and Bryant, S.L., "Gas Permeability of Shale", SPE Reservoir Evaluation & Engineering, (In press).

Shabro, V., Torres-Verdin, C., and Javadpour, F., "Numerical Simulation of Shale-Gas Production: From Pore-Scale Modeling of Slip-Flow, Knudsen Diffusion, and Langmuir Desorption to Reservoir Modeling of Compressible Fluid", SPE Paper 144355, presented at North American Unconventional Gas Conference and Exhibition, The Woodlands, Texas, USA, Jun. 14-16, 2011.

Shanley, K.W., Cluff, R.M., and Robinson, J.W., "Factors Controlling Prolific Gas Production From Low-Permeability Sandstones Reservoirs: Implications for Resource Assessment, Prospect Development, and Risk Analysis", AAPG Bulletin, 88, 1083-121, (2004).

Sondergeld, C.H., Newsham, K.E., Comisky, J.T., Rice, M.C., and Rai, C.S., "Petrophysical Considerations in Evaluating and Producing Shale Gas Resources", SPE Paper 131768, presented at SPE Unconventional Gas Conference, Pittsburgh, Pennsylvania, USA, Feb. 23-25, 2010.

Spencer, C.W., “Geologic Aspects of Tight Gas Reservoirs in the Rocky Mountain Region”, Journal of Petroleum Technology, 37, 1308-14, (1985).

Spencer, C.W., “Review of Characteristics of Low-permeability Gas Reservoirs in Western United States”, AAPG Bulletin, 73, 613-29, (1989).

Strickland, R., Purvis, D., and Blasingame, T., “Practical Aspects of Reserves Determinations for Shale Gas”, SPE Paper 144357, presented at North American Unconventional Gas Conference and Exhibition, Jun. The Woodlands, Texas, USA, Jun. 14-16, 2011.

Surdam, R.C., “A New Paradigm for Gas Exploration in Anomalously Pressured "Tight-Gas Sands" in the Rocky Mountain Laramide Basins, in R.C. Surdam, ed., Seals, Traps, and the Petroleum System”, AAPG Memoir, 67, 283-98, (1997).

Suri, P., Azeemuddin, M., Zaman, M., Kukreti, A.R., Roegiers, J.C., “Stress-dependent Permeability Measurement Using the Oscillating Pulse Technique”, Journal of Petroleum Science and Engineering, 17, 247-64, (1997).

Swanson, B.F.,”A Simple Correlation Between Permeability and Mercury Capillary Pressure”, Journal of Petroleum Technology, 33(12), 2498-504, (1981).

Thane, C., “Geometry and Topology of Model Sediments and Their Influence in Sediment Properties”, MS Thesis, The University of Texas at Austin, Austin, Texas, USA, (2006).

Thomeer, J. H., “Air Permeability as a function of Three Pore-Network Parameters”, Journal of Petroleum Technology, 35(4), 809-14, (1983).

Urbina, I., “Insiders Sound an Alarm Amid a Natural Gas Rush”. The New York Times, Jun. 26, (2011).

Walsh, M., and Lake, L.W., “A Generalized Approach to Primary Hydrocarbon Recovery (Handbook of Petroleum Exploration and Production)”, Amsterdam; Boston: Elsevier, 2003.

Wang, F.P., and Reed, R.M., “Pore Networks and Fluid Flow in Gas Shales” SPE Paper 124253, presented at Annual Technical Conference and Exhibition, New Orleans, Louisiana, USA, Oct. 4-7, 2009.

Wells, J.D., Amaefule, J.O.," Capillary Pressure and Permeability Relationships in Tight Gas Sands", SPE paper 13879, presented at SPE/DOE Low Permeability Gas Reservoirs Symposium, Denver, Colorado, USA, Mar. 19-22, 1985.

Xiao, Y., Bosch, R.V.D., Liu, F., Steffen, K., "Performance Evaluation in Data Rich Fayetteville Shale Gas Plays - Integrating Physics-based Reservoir Simulations with Data Driven Approaches for Uncertainty Reduction", SPE Paper 14940, presented at International Petroleum Technology Conference, , Bangkok, Thailand, Feb. 7-9, 2012.

Yang, Y., Aplin, A.C., "Permeability and Petrophysical Properties of 30 Natural Mudstones", Journal of Geophysical Research, 112, B03206, 1-14, (2007).

Zhou,Y., Zhang, R., Staroselsky, I., Chen, H., Kim, W.T., and Jhon, M.S., "Simulation of Micro- and Nano-scale Flows Via the Lattice Boltzmann Method", PHYSICA A, 362, 68-77, (2006).